Plasmonic enhancement of single-molecule fluorescence under one- and two-photon excitation

Lu, X.

Plasmonic Enhancement of Single-Molecule Fluorescence under One- and Two-Photon Excitation

Proefschrift

ter verkrijging van
de graad van doctor aan de Universiteit Leiden,
op gezag van rector magnificus prof. dr. ir. H. Bijl,
volgens besluit van het college voor promoties
te verdedigen op woensdag 08 december 2021
klokke 11.15 uur

door

Xuxing Lu

geboren te Fujian, China
in 1983

Promotor:
Prof. dr. M. A. G. J. Orrit

Copromotor:
Dr. M. J. A. de Dood

Promotiecommissie:

Prof. dr. Q. Wang	Suzhou Institute of Nano-Tech and Nano-Bionics
Dr. P. Zijlstra	Eindhoven University of Technology
Dr. W. Albrecht	AMOLF
Prof. dr. J. Aarts	
Prof. dr.ir. S. J. T. Van Noort	

Front & Back: The color stripes are the analogs of the single-molecule spectra from infrared dye under one-photon (red) and two-photon (blue) excitation. The graphics was modified from the art by Jorch (kde store).

Casimir PhD Series, Delft-Leiden 2021-44

ISBN 978-90-8593-506-3

An electronic version of this dissertation is available at
http://openaccess.leidenuniv.nl/.

The present work is financially supported by the Netherlands Organization for Scientific Research (NWO). The author acknowledges a Ph.D. grant from the China Scholarship Council.

Contents

1

Introduction

1

Collecting photons by eyes is probably one of the most efficient ways for us to perceive the environment. For centuries, great efforts have been made to extend our visual range by manipulating the propagation of light, e.g. through a telescope or microscope, we can see further or smaller into the world. Visualizing optically at micron or submicron length scales helps to reveal many secrets hidden to our naked eyes, especially in the biological systems. Recent technical advances in optics have pushed the detection capability down to the single-molecule level, giving a new access to the unique properties of individual molecules that usually cannot be distinguished in ensemble experiments[1, 2]. Single-molecule techniques have soon grown into an important field of optics, and spawned a revolution in biophysics/chemistry and other fields of nanoscience[3–10].

The challenge of detecting a single molecule optically comes from the mismatch between the molecular sizes and the wavelength of light, which results in very weak interactions between individual molecules and light[11, 12]. Pioneered by Orrit and Bernard in 1990[13], fluorescence, with the photons emitted at a longer wavelength than the excitation light (Stokes-shifted)[14], has been recognized as one of the most convenient means of probing single molecules, as the background can be suppressed efficiently by spectral filtering[15–18]. The fluorescence-based single-molecule technique, however, relies on the contrast provided by the emission of the target molecules against the background scattering and the photons from the environmental molecules. Therefore, this technique can only be applied to strong emitters (e.g. with quantum yields $> 10\%$), which limits its applications since the majority of molecules only emit weakly. Additionally, low molecular concentration ($\mathrm{pM} \sim \mathrm{nM}$) is required to get single-molecule sensitivity in conventional microscopy due to the diffraction limit of excitation beams[19].

Plasmonics nanostructures, well known for their subwavelength light confinements, offer a versatile solution to improve the detection sensitivity of single weak emitters by enhancing their fluorescence. The enhanced fluorescence from the molecules of low quantum yield ($10^{-1} \sim 10^{-3}$) inside the nanoscale near-field region, can easily overcome the total emission background from all the non-enhanced molecules in the micron-scale focusing volume, even for concentrations as high as μM[20]. Despite many successes of plasmon enhanced fluorescence experiments, detecting ultra-weak photon emission at single-molecule level is still a challenge. Example comes from the molecules with extremely low quantum yields (e.g. $< 10^{-3}$)[21], or with very low excitation efficiency, such as the fluorescence under two-photon excitation[22, 23].

This thesis aims to improve the detection from ultra-weak single emitter by enhancing their emission properties with plasmonic nanostructures. We exploit the wet-chemically synthesized single crystalline gold nanorods (GNRs) as our basic frameworks in the whole studies, simply because of their unique optical properties, such as the intense electromagnetic fields enhancement near the tips, and the narrow, tunable resonance with light. We first explore the lower limit of fluorescence quantum yield for single-molecule detection by enhancing the fluorescence with a single gold nanorod. Later, we develop a method to synthesize end-to-end gold nanorod dimers on glass substrates with the aid of molecular linkers, and then apply these strong plasmon coupling systems to enhance the single-molecule fluorescence under two-photon excitation.

1.1. Surface plasmon resonance of gold nanoparticles

Propagating and localized surface plasmons

"Surface plasmons" (SPs) refers to the collective oscillations of conduction electrons that exists at the metal-dielectric interfaces. While still a hot topic of research, the observations and applications of SPs has a long history and can be dated back to Roman empire. The famous example is the Lycurgus cup, which shows different color depending on the location of the light source. A theoretical description of SPs however came only after Gustav Mie gave the first full solution to the scattering of light by a spherical metallic particle in 1908[24], and was explained as the coherent oscillation of electrons at metal surfaces by Rufus Ritchie in 1957[25].

Surface plasmons can be categorized into two main subclasses: the propagating SP polaritons (SPPs) waves that travel along the metal-dielectric interface at a wavelength shorter than the free light in the dielectric material[25–29], and the localized SPs (LSPs) modes that are excited in the metal structures with sizes comparable to or smaller than the exciting light, such as metal nanoparticles[30–32]. Although both the SPPs and LSPs can remarkably enhance the electromagnetic fields near the surfaces, the LSPs are more favored for singe-molecule sensing, primarily because the LSPs are more convenient to excite (no requirement on the momentum of the exciting light), and the near fields of LSPs are more localized into a small volume, instead of distributed widely around the interfaces as the propagating modes. Additionally, they also benefit from the cheap but reliable synthesis of metallic nanoparticles, with their shapes and sizes being adjustable to tune their plasmon resonances[33].

Localized surface plasmons of gold nanoparticles

Among different types of plasmoics nanoparticles, wet-chemcally systhesized gold nanoparticles have attracted most attention, mainly because of their chemical stability and the excellent performance in the visible and NIR spectral ranges. As a straightforward example, a single gold nano-sphere shows a strong plasmon resonance in the visible range around $520 \sim 580\ \mathrm{nm}$, when its size is smaller than $100\ \mathrm{nm}$ (see figure 1.1a)[34]. The strong scattering and absorption of light in this color range by the gold nanoparticles can explain the secret of the orientation-dependent color change of the Lycurgus cup, which contains tiny gold nanoparticles dispersing in the glass. The gold nanoparticle also exhibits nanofocusing ability of electromagnetic fields. As is depicted in figures 1.1c. and 1.1e., the electric field is localized at the surface of the gold nanosphere at resonance, and the intensity reduces rapidly in a few nanometers away from the surface, depending on the size of the particles.

The limitation of spherical gold nanoparticles for single-molecule sensing arises from their small field enhancements. As is shown in Figure 1c., the maximum field enhancement given by a gold nanosphere only reaches the magnitude of 10^1, which is usually too low for enhancing weak signals from single molecules. Additionally, the tunable spectral range, corresponding to enhancement by the narrow dipole plasmonic mode, covers only small range of visible light (e.g. $520 \sim 580\ \mathrm{nm}$ for particle size $\leq 100\ \mathrm{nm}$), which further limits their applications to a few favourable emitters. Extending to longer wavelength can

1

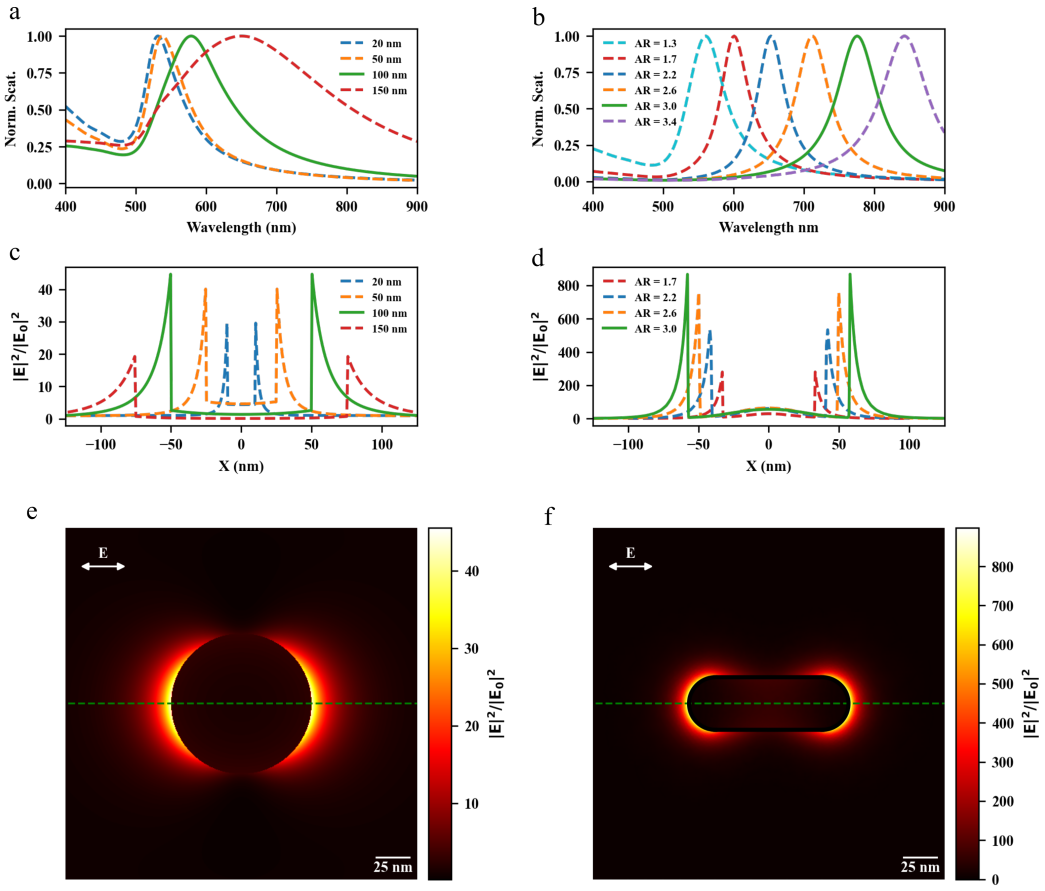

Figure 1.1: Surface plasmons of single gold nanospheres and gold nanorods in water. (a, b) Simulated scattering spectra of the gold nanospheres (a) and nanorods (b) excited by a linear polarized plane wave. In the simulations, Mie theory was performed for the spherical particles of varied sizes (here, 20, 50, 100, and 150 nm), and the boundary element method was used for the nanorods with a fixed diameter of 38 nm but with different aspect ratios. (c, d) The corresponding electric field intensity distributions along the main axis (green dashed in e and f) of the gold nanoparticles (c) and nanorods (d) at resonance. (e, f) The electric field intensity profile around the resonant gold nanosphere (e) and gold nanorod (f), corresponding to the size of 100 nm for the nanosphere, and 38 nm $\times$ 114nm for the nanorod.

be done by choosing a larger nanoparticle , yet, increasing the size (e.g. $> 150\ \mathrm{nm}$) results in a smaller near-field enhancement (red dashed in figure 1.1.c.) and larger luminescence background from the particles as the result of the broad plasmon resonance (red dashed in figure 1.1a.).

Localized surface plasmons of gold nanorods

Compared to gold nanospheres, the elongated gold nanorods (GNRs) exhibit better optical performance in nanofocusing[35]. As an anisotropic structure, GNRs support two primary plasmonic modes, the transverse mode and the longitudinal mode, corresponding to electron oscillations perpendicular or parallel to the longitudinal axis, respectively[36]. While the transverse modes display constant resonance at around $514\ \mathrm{nm}$, the longitudinal modes are more sensitive to the particle shapes, and can be well tuned from visible to near infrared region by adjusting their aspect ratio. As the resonances are further away from the interband transition band of gold, the damping effect due to Ohmic loss becomes weaker, resulting in narrower resonance bands as is shown in figure 1.1b.. The intense plasmon gives rise to very large near-field enhancement near the tips (see figures 1.1d., and 1.1e.), a feature that have been widely used to enhance weak signals, such as Raman scattering or fluorescence from single molecules. The longitudinal plasmon modes of GNRs are also very sensitive to the surrounding environment[37, 38]. As an example, by monitoring the plasmon shifts of GNRs, one might even be able to sense the tiny refractive index changes caused by the approach of a small object, such as a single protein molecule[39].

The applications of GNRs are also inspired by their chemical stability and by the flexibility of tuning their sizes and shapes. The sizes and aspect ratios of GNRs can be readily controlled during the synthesis process[40, 41], or can be adjusted by overgrowth or oxidation of the GNRs[42]. As a result, the plasmon resonances of GNRs can be tuned to cover a broader range of molecular absorbance bands, hence extends their applications to more species of molecules. GNRs are also suitable for biological applications because of their biocompatibility[43]. They can be conveniently functionalized with different molecules, including drug- or bio-molecules, though the high affinity of gold towards thiols[44, 45]. Moreover, the molecules can be specifically functionalized to the tips or to side of GNRs, as a result of the site-dependent reactivity of GNRs. The site-specifically functionalization of GNRs offers more controllable ways to study the interaction of molecules with the longitudinal plasmon modes. For example, the tip-specific functionalization of GNRs can improve the detection sensitivity of single molecules as the molecules can specifically be located inside the nearfield hotspots to get maximum signals enhancements[46, 47].

Plamonic coupling of end-to-end gold nanorod dimers

The plasmon resonance of a plasmonic nanostructure can be significantly modified by coupling with other nanostructures. Inspired by molecular orbital theory, the plasmon resonances resulting from plasmonic coupling can be regarded as the hybridization of the basic plasmon resonances of each component[48–50]. The hybridized plasmon resonances can be classified according to the relative oscillating behaviors of all the basic plasmon modes, or simply categorized into dark modes and bright modes according to their response to the

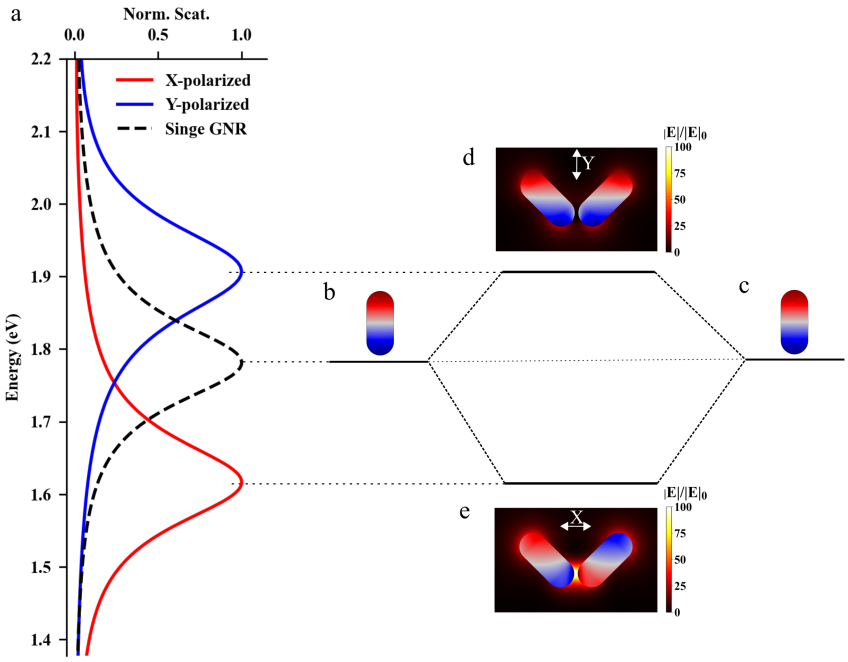

Figure 1.2: Plasmonic hybridization of a v-shaped gold nanorod dimer in the medium water ($n = 1.33$). (a) The black dashed line represents the scattering spectrum of the single GNR with the size of $40\ \mathrm{nm} \times 94\ \mathrm{nm}$, while the blue and red solid lines give the scattering spectra for the v-shaped GNRs dimer excited by light with the polarization perpendicular (S-polarized) and parallel (P-polarized) to the symmetry axis, respectively. The structure of the dimer was set as $\pi/2$ and the interparticle gap was set as $5\ \mathrm{nm}$. (b, c) The surface charge profile of the single GNR at the plasmonic resonance, (d, e) give the surface charges and the near-field profiles of the two hybridized plasmonic modes oscillating symmetrically and anti-symmetrically, respectively. In the simulations, the scattering spectra were calculated by using the boundary element method (Scuff-Em), while the near-fields and the surface charges were simulated with COMSOL Multiphysics.

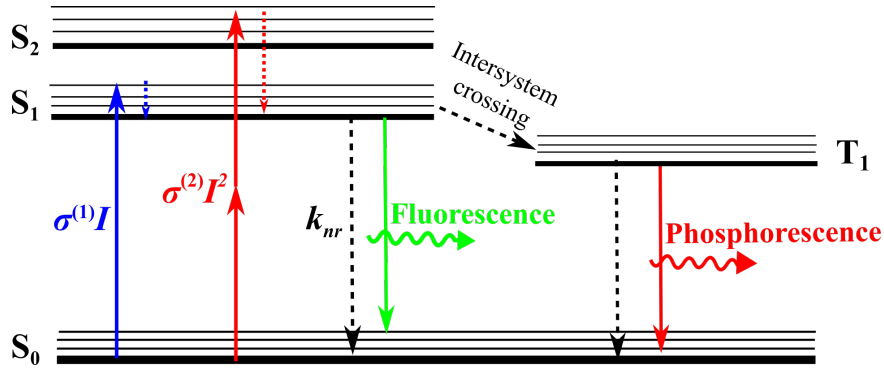

Figure 1.3: Jablonski diagram illustrating the light emission process under one-photon or two-photon excitation. $\sigma^{(1)}$ and $\sigma^{(2)}$ represent the one- and two-photon absorption cross-sections, respectively, I is the intensity of excitation photon flux, and k_{nr} is the non-radiative rate.

excitation light. The dark plasmon modes are usually hard to excite with plane light waves, while the bright modes show strong reaction to the incident light, resulting in large interaction cross sections and strong near field enhancements in some of the interparticle gaps[51].

The plasmonic coupling of nanostructures is determined by the materials, shapes, sizes, and the arrangements of all the coupling components. As a simple example depicted in figure 3., the plasmon resonance of a symmetric v-shaped GNRs dimer nanostructure splits into a symmetric (bonding) low-energy mode, and a anti-symmetric (anti-bonding) high-energy mode. The bonding or anti-bonding modes of the GNRs dimer can be excited by normal incident plane light with polarization perpendicular or parallel to the symmetry axis, respectively. Similar to the electron distribution of a covalent bonding molecule, the electromagnetic field profiles of the v-shaped GNRs dimer are also dependent on the symmetry of the plasmon oscillations. For the bonding mode, the near-field is strongly confined in the small gaps of the dimer, while for the anti-bonding mode, the field is localized with smaller enhancement around the far ends of the GNRs . The plasmon resonances of these two modes are also dependent on the angle between the long axes of the two GNRs. As the long axes of two GNRs are aligned along each other, only the bonding mode can be excited, and the anti-bonding mode at the shorter wavelength is hidden in the spectra, corresponding respectively to the bright and dark modes mentioned above[52, 53].

1.2. Fluorescence and fluorescence enhancement

One-photon-excited fluorescence

Materials can emit photons as they are excited to high energy levels. If the excitation is due to the absorption of photons, the emission is called photoluminescence. Fluorescence refers to the photoluminescence while the photon is emitted subsequently (in the timescale of sub-nanosecond or nanosecond) after the absorption of one photon[14]. For normal molecules at room temperature, the emission photons usually have longer wavelength compared to the excitation, a phenomenon called Stokes shift. The energy loss of the emitted photon is due

to the nonradiative relaxation of the excited molecule from the higher vibrational sub-levels to the lowest level of the excited electron state, as is depicted in figure 1.3. After a time of sub-nanosecond to ~ 10 ns, the molecule is then dissipated to the ground state by emitting a photon, or though other nonradiative pathways. Alternatively, the molecule may also be transferred to the lowest excited triplet state (T_1), a dark state where the molecule can stay for a time scale of microseconds before nonradiatively relaxing to the ground state. The random switching between the bright state (S_1) and the dark state (T_1) results in a phenomenon known as fluorescence blinking, where the molecule enters nonfluorescent state repeatedly under continuous excitation. Here we should mention that, at low temperature, the molecule at the triplet state (T_1) can also emit photon, a process called phosphorescence.

The excitation rate of one-photon excitation (OPE) $k_{\mathrm{exc}}^{(1)}$ below saturation is proportional to the photon flux intensity of the excitation I_{exc} as: $k_{\mathrm{exc}}^{(1)} = \sigma^{(1)} I_{\mathrm{exc}}$, where $\sigma^{(1)}$ is the one-photon absorption cross section of the molecule. Considering the long lifetime of the triplet state, the contribution of the intersystem crossing rate (k_{iSC}) to the total relaxing rate is often negligible, therefore the quantum yield of a fluorophore can be simply expressed as

$$\eta = k_{\mathrm{r}}/(k_{\mathrm{r}} + k_{\mathrm{nr}}) \tag{1.1}$$

here, k_{r} is the radiative rate, which is determined by the local density of photon states, and k_{nr} is the nonradiative rate. For a great majority of strongly absorbing molecules, the nonradiative rate dominates the deactivation process of the excited state to the ground state ($k_{\mathrm{nr}} \gg k_{\mathrm{r}}$), hence inhibits the spontaneous emissions of the molecules, resulting in very weak emitters that are very difficult to detect.

Two-photon-excited fluorescence

Instead of being excited by only one photon, the fluorophores can also be excited by multiple photons of lower energy. The simplest variant of multi-photon excitation is two-photon excitation, where the molecule is excited by absorbing two photons of identical frequencies simultaneously. Two-photon excitation (TPE) is a nonlinear optical process where the excitation rate $k_{\mathrm{exc}}^{(2)}$ is proportional to the square of the incident light intensity $k_{\mathrm{exc}}^{(2)} = \sigma^{(2)} I_{\mathrm{exc}}^2$[54], where $\sigma^{(2)}$ is the two-photon absorption cross section. TPE extends the absorption band into longer wavelength, usually in the infrared range, by exciting with two photons of the same wavelength. The excitation wavelength of TPE, however, is not necessary the double of OPE, as the molecules under TPE may be excited to different excited electron state due to the different selection rule for TPE. The emission spectra, however, is identical to one-photon-excited fluorescence, as the molecule only emits from the lowest level of the excited state S_1, according to the Kasha's rule. As a result, the lifetime and the quantum yield of the molecules under two-photon-excitation will be similar as those of one-photon-excited fluorescence.

TPE spectroscopy has attracted significant research interests because of its advantages over its OPE counterpart: 1), TPE facilities tissue penetration and background suppression as the result of the longer excitation wavelength, which may fall into the "biological transparency window"[55, 56]; 2), TPE allows inherent optical sectioning without the need of rejecting the out-of-focus emission, as the excitation under TPE is limited to a small volume, due to squared dependence of TPE on the incident light[57–59]; 3), for the same reason,

TPE also avoids out-of-focus photobleaching, which allows multiple scanning with reduced photodamage to the samples[60, 61].

The major obstruction for the application of TPE comes from the extremely low TPE efficiency which requires very high excitation intensity. Since first predicted by Goppert Mayer in 1931[54], TPE was only experimentally verified until the invention of lasers in 1960s, which could provide enough coherent photons for TPE[62, 63]. Yet illumination by light with very high power may also cause unacceptable photodamge to the samples. Ultra-short-pulsed laser, being able to generate ultra-high pulse intensities while still keeping the average output power relatively low, have stimulated the rapid growth of TPE's applications since its invention in 1990s[57]. Investigation of TPE at single-molecule level, however, is still a challenge. The TPA cross section for normal dyes is very low due to their small sizes ($1 \sim 3$ nm), typically in the range of $10^0 \sim 10^2$ GM (Goppert-Mayer), while $1\ \mathrm{GM} = 10^{-50}\mathrm{cm}^4\mathrm{s}\ \mathrm{molecule}^{-1}\ \mathrm{photon}^{-1}$[64–66].

Plasmonic enhancement of single-molecule fluorescence

The essential difficulty of detecting a single weak emitter is how to extract the weak signals from the background. In normal microscopy, limited by the diffraction of light, "selective" excitation of a particular molecule while keeping the surrounding molecules unexcited is very difficult, especially when the molecular concentration is high. By utilizing nano plasmonic lenses, one can create "superemitters" with enhanced fluorescence intensities overwhelm the brightness of the surrounding molecules. The enhancement of the fluorescence arises from the enhancement of the exciting electric field and from the enhancement of the radiative rate by coupling the emitters with the plasmonic nanoparticles. First of all, the excitation rate k_{exc} can be highly enhanced in the vicinity of the nanoparticle as a result of the strong electromagnetic field confinement. The enhancement factor ξ_{exc} shows different intensity dependence for OPE and for TPE on the excitation power: for OPE, ξ_{exc} is proportional to the enhancement of the near-field intensity, while for TPE, it scales with the square of the enhancement of the excitation light intensity. Secondly, the spontaneous emission k_{r} of the fluorophore can also be enhanced by the particle via the Purcell effect, which is related to the local density of photon states. Associated to the dissipative losses of the metals, however, coupling with the plasmon modes may also introduce additional non-radiative decay channels, which may quench the fluorescence of the molecules. The balance between the enhancement and the quenching strongly depends on the relative position and orientation of the emitter with respect to the nanoparticles, which may change the spectral shapes of the emissions and the lifetimes. The enhancement factor can be tuned by adjusting the sizes, shapes and the configurations of the nanoparticles.

Considering the simple two-level scheme, the overall enhancement under weak excitation can be expressed as[21, 67]

$$\xi_{\mathrm{total}} = \frac{\xi_{\mathrm{exc}}\xi_{\mathrm{rad}}}{1 + \eta_0(\xi_{\mathrm{rad}} + K_{\mathrm{nr}}/k_{\mathrm{r}}^0 - 1)}, \tag{1.2}$$

here, ξ_{exc} represents the excitation enhancement, $\xi_{\mathrm{rad}} = k_{\mathrm{r}}/k_{\mathrm{r}}^0$ is the radiative enhancement factor, which accounts for the increased local density of states in the vicinity of the antenna . k_r and k_r^0 are the radiative decay rates with and without the nanoantenna, respectively,

η_0 is the intrinsic quantum yield of the emitter, and K_{nr} is the additional non-radiative absorption rate due to dissipative losses of the nanoantenna. The lifetime of the fluorescence is shortened as[22]

$$\tau/\tau_0 = \eta_0^{-1}(\xi_{\mathrm{rad}} + K_{\mathrm{nr}}/k_{\mathrm{r}}^0 + 1/\eta_0 - 1)^{-1} \tag{1.3}$$

1.3. Outline of the thesis

This thesis examines the single-molecule detection of very weak optical signals enhanced by gold-nanorod-based plasmonic nanostructures. We first used single gold nanorods to enhance the conventional one-photon-excited fluorescence from single molecules with extremely low quantum yield ($\eta \sim 10^{-4}$). Later, we explored single-molecule detection of the fluorescence under two-photon-excitation enhanced by end-to-end gold nanorod dimer. Further experiments confirmed that such gold nanorod dimers may also be used to enhance the anti-Stokes Raman scattering, once the strong plasmon coupling between each rod not only strongly enhance the nearfield but also heat up the medium around the molecules inside the gap. The contents of the thesis is organized as follows:

In **Chapter 2**, we give general evaluation of single-molecule fluorescence with the enhancement by gold-nanorod-related plasmonic nanostructures. We performed full-wave simulations based on the boundary element method to estimate the fluorescence enhancement factor under OPE or TPE, by single gold nanorods, or by end-to-end gold nanorod dimers. The modification of the emission spectra and of the fluorescence lifetime by the plasmon modes are also investigated theoretically.

Chapter 3 demonstrates the single-molecule detection of a very weak emitter with a quantum yield of about 10^{-4} and a comparatively large Stokes shift of $3000\ \mathrm{cm}^{-1}$, by enhancing the fluorescence with single gold nanorods. We optimize the fluorescence rates by optimizing the excitation wavelength and the plasmon resonance. We further theoretically estimated that the quantum yield detection limit of a single molecule could be as low as 10^{-6}, provided the dwell time of the molecules in the plasmonic hot spot is long enough.

In **Chapter 4**, we develop a method to synthesize end-to-end gold nanorod dimers with the aid of molecular linkers. We controlled the end-to-end assembly in the presence of CTAB surfactant, which forms a bilayer that coats more compact over the side of the rods, to favor the attachment of the linker molecules at the tips. The interparticle gaps were kept open by choosing biomolecule pairs of streptavidin and biotin disulfide as the linkers, which ensures a separation of around $5\ \mathrm{nm}$ between the two nanorods.

In **Chapter 5**, we exploit the end-to-end gold nanorod dimer to enhance the two-photon-excited fluorescence of a single organic molecule. The strong plasmon coupling between the rods induces a very intense local field in the gap, with the maximum enhancement factor up 10^2, resulting in a TPE enhancement of $10^7 \sim 10^8$. With such high enhancement factor, we successfully detected two-photon-excited fluorescence at single-molecule level. Correlated scanning electron microscope images (SEM) were taken later to examine the configurations of the gold nanorod dimer structures.

References

[1] W. E. Moerner and Michel Orrit. Illuminating Single Molecules in Condensed Matter. *Science*, 283(5408):1670–1676, March 1999.

[2] David R. Walt. Optical Methods for Single Molecule Detection and Analysis. *Analytical Chemistry*, 85(3):1258–1263, February 2013.

[3] Shimon Weiss. Fluorescence Spectroscopy of Single Biomolecules. *Science*, 283(5408):1676–1683, March 1999.

[4] Elizabeth Rhoades, Eugene Gussakovsky, and Gilad Haran. Watching proteins fold one molecule at a time. *Proceedings of the National Academy of Sciences*, 100(6):3197–3202, March 2003.

[5] Harold Craighead. Future lab-on-a-chip technologies for interrogating individual molecules. *Nature*, 442(7101):387–393, July 2006.

[6] F. Ritort. Single-molecule experiments in biological physics: Methods and applications. *Journal of Physics: Condensed Matter*, 18(32):R531–R583, July 2006.

[7] Fredrik Persson, Irmeli Barkefors, and Johan Elf. Single molecule methods with applications in living cells. *Current Opinion in Biotechnology*, 24(4):737–744, August 2013.

[8] Michel Orrit, Taekjip Ha, and Vahid Sandoghdar. Single-molecule optical spectroscopy. *Chemical Society Reviews*, 43(4):973–976, January 2014.

[9] Sebastian van de Linde and Markus Sauer. How to switch a fluorophore: From undesired blinking to controlled photoswitching. *Chemical Society Reviews*, 43(4):1076–1087, January 2014.

[10] Zdeněk Farka, Matthias J. Mickert, Matěj Pastucha, Zuzana Mikušová, Petr Skládal, and Hans H. Gorris. Advances in Optical Single-Molecule Detection: En Route to Supersensitive Bioaffinity Assays. *Angewandte Chemie International Edition*, 59(27):10746–10773, 2020.

[11] W. E. Moerner and L. Kador. Optical detection and spectroscopy of single molecules in a solid. *Physical Review Letters*, 62(21):2535–2538, May 1989.

[12] W. E. (William E.) Moerner. Nobel Lecture: Single-molecule spectroscopy, imaging, and photocontrol: Foundations for super-resolution microscopy. *Reviews of Modern Physics*, 87(4):1183–1212, October 2015.

[13] M. Orrit and J. Bernard. Single pentacene molecules detected by fluorescence excitation in a p-terphenyl crystal. *Physical Review Letters*, 65(21):2716–2719, November 1990.

[14] Joseph R Lakowicz. *Principles of fluorescence spectroscopy*. Springer science & business media, 2013.

[15] Taekjip Ha, Alice Y. Ting, Joy Liang, W. Brett Caldwell, Ashok A. Deniz, Daniel S. Chemla, Peter G. Schultz, and Shimon Weiss. Single-molecule fluorescence spectroscopy of enzyme conformational dynamics and cleavage mechanism. *Proceedings of the National Academy of Sciences*, 96(3):893–898, February 1999.

[16] Shimon Weiss. Measuring conformational dynamics of biomolecules by single molecule fluorescence spectroscopy. *Nature Structural Biology*, 7(9):724–729, September 2000.

[17] W. E. Moerner and David P. Fromm. Methods of single-molecule fluorescence spectroscopy and microscopy. *Review of Scientific Instruments*, 74(8):3597–3619, August 2003.

[18] Manuel F Juette, Daniel S Terry, Michael R Wasserman, Zhou Zhou, Roger B Altman, Qinsi Zheng, and Scott C Blanchard. The bright future of single-molecule fluorescence imaging. *Current Opinion in Chemical Biology*, 20:103–111, June 2014.

[19] Lukas Novotny and Bert Hecht. *Principles of nano-optics*. Cambridge university press, 2012.

[20] Deep Punj, Mathieu Mivelle, Satish Babu Moparthi, Thomas S. van Zanten, Hervé Rigneault, Niek F. van Hulst, María F. García-Parajó, and Jérôme Wenger. A plasmonic 'antenna-in-box' platform for enhanced single-molecule analysis at micromolar concentrations. *Nature Nanotechnology*, 8(7):512–516, July 2013.

[21] Xuxing Lu, Gang Ye, Deep Punj, Ryan C. Chiechi, and Michel Orrit. Quantum Yield Limits for the Detection of Single-Molecule Fluorescence Enhancement by a Gold Nanorod. *ACS Photonics*, 7(9):2498–2505, September 2020.

[22] Weichun Zhang, Martín Caldarola, Xuxing Lu, and Michel Orrit. Plasmonic Enhancement of Two-Photon-Excited Luminescence of Single Quantum Dots by Individual Gold Nanorods. *ACS Photonics*, 5(7):2960–2968, July 2018.

[23] Oluwafemi S. Ojambati, Rohit Chikkaraddy, William M. Deacon, Junyang Huang, Demelza Wright, and Jeremy J. Baumberg. Efficient Generation of Two-Photon Excited Phosphorescence from Molecules in Plasmonic Nanocavities. *Nano Letters*, 20(6):4653–4658, June 2020.

[24] Gustav Mie. Beiträge zur Optik trüber Medien, speziell kolloidaler Metallösungen. *Annalen der Physik*, 330(3):377–445, 1908.

[25] R. H. Ritchie. Plasma Losses by Fast Electrons in Thin Films. *Physical Review*, 106(5):874–881, June 1957.

[26] Heinz Raether. Surface plasmons on smooth surfaces. In *Surface plasmons on smooth and rough surfaces and on gratings*, pages 4–39. Springer, 1988.

[27] Michael G Cottam and David R Tilley. *Introduction to surface and superlattice excitations*. CRC Press, 2019.

[28] Vladimir Moiseevich Agranovich. *Surface polaritons*. Elsevier, 2012.

[29] Jan Renger, Romain Quidant, Niek van Hulst, Stefano Palomba, and Lukas Novotny. Free-Space Excitation of Propagating Surface Plasmon Polaritons by Nonlinear Four-Wave Mixing. *Physical Review Letters*, 103(26):266802, December 2009.

[30] K. Lance Kelly, Eduardo Coronado, Lin Lin Zhao, and George C. Schatz. The Optical Properties of Metal Nanoparticles: The Influence of Size, Shape, and Dielectric Environment. *The Journal of Physical Chemistry B*, 107(3):668–677, January 2003.

[31] Matthew Rycenga, Claire M. Cobley, Jie Zeng, Weiyang Li, Christine H. Moran, Qiang Zhang, Dong Qin, and Younan Xia. Controlling the Synthesis and Assembly of Silver Nanostructures for Plasmonic Applications. *Chemical Reviews*, 111(6):3669–3712, June 2011.

[32] Uwe Kreibig and Michael Vollmer. *Optical properties of metal clusters*, volume 25. Springer Science & Business Media, 2013.

[33] Valerio Voliani. *Gold Nanoparticles*. De Gruyter, April 2020.

[34] Stephan Link and Mostafa A. El-Sayed. Size and Temperature Dependence of the Plasmon Absorption of Colloidal Gold Nanoparticles. *The Journal of Physical Chemistry B*, 103(21):4212–4217, May 1999.

[35] Huanjun Chen, Lei Shao, Qian Li, and Jianfang Wang. Gold nanorods and their plasmonic properties. *Chemical Society Reviews*, 42(7):2679–2724, 2013.

[36] Jorge Zuloaga, Emil Prodan, and Peter Nordlander. Quantum Plasmonics: Optical Properties and Tunability of Metallic Nanorods. *ACS Nano*, 4(9):5269–5276, September 2010.

[37] Jan Becker, Andreas Trügler, Arpad Jakab, Ulrich Hohenester, and Carsten Sönnichsen. The Optimal Aspect Ratio of Gold Nanorods for Plasmonic Bio-sensing. *Plasmonics*, 5(2):161–167, June 2010.

[38] Martin Dieter Baaske, Peter Sebastian Neu, and Michel Orrit. Label-Free Plasmonic Detection of Untethered Nanometer-Sized Brownian Particles. *ACS Nano*, 14(10):14212–14218, October 2020.

[39] Peter Zijlstra, Pedro M. R. Paulo, and Michel Orrit. Optical detection of single non-absorbing molecules using the surface plasmon resonance of a gold nanorod. *Nature Nanotechnology*, 7(6):379–382, June 2012.

[40] N. R. Jana, L. Gearheart, and C. J. Murphy. Seed-Mediated Growth Approach for Shape-Controlled Synthesis of Spheroidal and Rod-like Gold Nanoparticles Using a Surfactant Template. *Advanced Materials*, 13(18):1389–1393, 2001.

[41] J. Pérez-Juste, L. M. Liz-Marzán, S. Carnie, D. Y. C. Chan, and P. Mulvaney. Electric-Field-Directed Growth of Gold Nanorods in Aqueous Surfactant Solutions. *Advanced Functional Materials*, 14(6):571–579, 2004.

[42] Weihai Ni, Xiaoshan Kou, Zhi Yang, and Jianfang Wang. Tailoring Longitudinal Surface Plasmon Wavelengths, Scattering and Absorption Cross Sections of Gold Nanorods. *ACS Nano*, 2(4):677–686, April 2008.

[43] Hongwei Liao and Jason H. Hafner. Gold Nanorod Bioconjugates. *Chemistry of Materials*, 17(18):4636–4641, September 2005.

[44] Dakrong Pissuwan, Stella M. Valenzuela, and Michael B. Cortie. Prospects for Gold Nanorod Particles in Diagnostic and Therapeutic Applications. *Biotechnology and Genetic Engineering Reviews*, 25(1):93–112, January 2008.

[45] Xiaoge Hu and Xiaohu Gao. Multilayer coating of gold nanorods for combined stability and biocompatibility. *Physical Chemistry Chemical Physics*, 13(21):10028–10035, 2011.

[46] Peter Zijlstra, Pedro M. R. Paulo, Kuai Yu, Qing-Hua Xu, and Michel Orrit. Chemical Interface Damping in Single Gold Nanorods and Its Near Elimination by Tip-Specific Functionalization. *Angewandte Chemie*, 124(33):8477–8480, 2012.

[47] Pedro M. R. Paulo, Peter Zijlstra, Michel Orrit, Emilio Garcia-Fernandez, Tamara C. S. Pace, Ana S. Viana, and Sílvia M. B. Costa. Tip-Specific Functionalization of Gold Nanorods for Plasmonic Biosensing: Effect of Linker Chain Length. *Langmuir*, 33(26):6503–6510, July 2017.

[48] E. Prodan, C. Radloff, N. J. Halas, and P. Nordlander. A Hybridization Model for the Plasmon Response of Complex Nanostructures. *Science*, 302(5644):419–422, October 2003.

[49] T. J. Davis, D. E. Gómez, and K. C. Vernon. Simple Model for the Hybridization of Surface Plasmon Resonances in Metallic Nanoparticles. *Nano Letters*, 10(7):2618–2625, July 2010.

[50] Boris Luk'yanchuk, Nikolay I. Zheludev, Stefan A. Maier, Naomi J. Halas, Peter Nordlander, Harald Giessen, and Chong Tow Chong. The Fano resonance in plasmonic nanostructures and metamaterials. *Nature Materials*, 9(9):707–715, September 2010.

[51] Liane S. Slaughter, Yanpeng Wu, Britain A. Willingham, Peter Nordlander, and Stephan Link. Effects of Symmetry Breaking and Conductive Contact on the Plasmon Coupling in Gold Nanorod Dimers. *ACS Nano*, 4(8):4657–4666, August 2010.

[52] Jatish Kumar, Xingzhan Wei, Steven Barrow, Alison M. Funston, K. George Thomas, and Paul Mulvaney. Surface plasmon coupling in end-to-end linked gold nanorod dimers and trimers. *Physical Chemistry Chemical Physics*, 15(12):4258–4264, February 2013.

[53] Xuxing Lu, Jian Wu, Qiannan Zhu, Junwei Zhao, Qiangbin Wang, Li Zhan, and Weihai Ni. Circular dichroism from single plasmonic nanostructures with extrinsic chirality. *Nanoscale*, 6(23):14244–14253, 2014.

[54] Maria Göppert-Mayer. über Elementarakte mit zwei Quantensprüngen. *Annalen der Physik*, 401(3):273–294, 1931.

[55] Patrick Theer, Mazahir T. Hasan, and Winfried Denk. Two-photon imaging to a depth of 1000 Mm in living brains by use of a Ti:Al_2O_3 regenerative amplifier. *Optics Letters*, 28(12):1022–1024, June 2003.

[56] Fritjof Helmchen and Winfried Denk. Deep tissue two-photon microscopy. *Nature Methods*, 2(12):932–940, December 2005.

[57] W. Denk, J. H. Strickler, and W. W. Webb. Two-photon laser scanning fluorescence microscopy. *Science*, 248(4951):73–76, April 1990.

[58] C. J. R SHEPPARD and M. GU. Image formation in two-photon fluorescence microscopy. *Image formation in two-photon fluorescence microscopy*, 86(3):104–106, 1990.

[59] Min Gu and C. J. R. Sheppard. Comparison of three-dimensional imaging properties between two-photon and single-photon fluorescence microscopy. *Journal of Microscopy*, 177(2):128–137, 1995.

[60] William A. Mohler, Jeffrey S. Simske, Ellen M. Williams-Masson, Jeffrey D. Hardin, and John G. White. Dynamics and ultrastructure of developmental cell fusions in the Caenorhabditis elegans hypodermis. *Current Biology*, 8(19):1087–1091, September 1998.

[61] Jayne M. Squirrell, David L. Wokosin, John G. White, and Barry D. Bavister. Long-term two-photon fluorescence imaging of mammalian embryos without compromising viability. *Nature Biotechnology*, 17(8):763–767, August 1999.

[62] P. A. Franken, A. E. Hill, C. W. Peters, and G. Weinreich. Generation of Optical Harmonics. *Physical Review Letters*, 7(4):118–119, August 1961.

[63] W. Kaiser and C. G. B. Garrett. Two-Photon Excitation in Ca${\mathrm{F}}_{2}$: ${\mathrm{Eu}}^{2+}$. *Physical Review Letters*, 7(6):229–231, September 1961.

[64] Marius A. Albota, Chris Xu, and Watt W. Webb. Two-photon fluorescence excitation cross sections of biomolecular probes from 690 to 960 nm. *Applied Optics*, 37(31):7352–7356, November 1998.

[65] Amit Nag and Debabrata Goswami. Solvent effect on two-photon absorption and fluorescence of rhodamine dyes. *Journal of Photochemistry and Photobiology A: Chemistry*, 206(2):188–197, August 2009.

[66] Chris Xu and Watt W. Webb. Measurement of two-photon excitation cross sections of molecular fluorophores with data from 690 to 1050 nm. *JOSA B*, 13(3):481–491, March 1996.

[67] Saumyakanti Khatua, Pedro M. R. Paulo, Haifeng Yuan, Ankur Gupta, Peter Zijlstra, and Michel Orrit. Resonant Plasmonic Enhancement of Single-Molecule Fluorescence by Individual Gold Nanorods. *ACS Nano*, 8(5):4440–4449, May 2014.

2

Theoretical investigations of the single-molecule fluorescence enhancements by a single gold nanorod and by an end-to-end gold nanorod dimer

Single gold nanorod supports the longitudinal plasmon modes that may enhance not only the near-fields but also the local density of photon states near the tips. As a consequence, single gold nanorods can be used to enhance the fluorescence of weak emitters, by enhancing both the excitation and radiative rates. Gold nanorod dimer, arranged in an end-to-end configuration, may strengthen both effects inside the gap owing to the strong plasmon coupling. This provides stronger fluorescence enhancement. We compare the fluorescence enhancement by a single gold nanorod to that of a gold nanorod dimer with interparticle gap of $5\,\mathrm{nm}$*. We consider fluorescent dyes with different absorption and emission bands. Our simulations reveal that, at weak excitation, an enhancement factor of* $\sim 10^4$ *can be achieved by the dimer for one-photon excited fluorescence, while for two-photon-excited fluorescence, the enhancement factor by the dimer can be as high as* $\sim 10^8$*. The influence of plasmon modes on the fluorescence lifetime and on the spectral shaping is also investigated for all the dyes. At high excitation intensity, the enhancement factor for both one- or two-photon-excited fluorescence will be saturated to a limited value of the radiative enhancement by the plasmonic structures.*

2.1. Introduction

The most valuable feature of noble metal nanoparticles comes from the collective oscillation of surface charges, also known as the localized surface plasmon resonance (SPR)[1, 2]. Controlling the SPR of nanoparticles provides an effective way of manipulating the light-matter interaction on the nanoscale[3–6]. As a straightforward approach, coupling to plasmonic nanoparticles can strongly influence the fluorescence processes of fluorophores[7–19]. First of all, the excitation efficiencies of the fluorophores can be largely enhanced due to the strong light-field confinement near the plasmonic nanoparticles. Secondly, the SPR of the nanoparticles may also increase the local density of photon states (LDOS) around the surfaces, which, in turn, enhances the radiative rate of the excited fluorophore according to the Purcell effect[20, 21]. The emission rates of the emitters, however, may be quenched via the additional non-radiative channels induced by the Ohmic absorption of the metal[8, 22, 23]. Consequently, the interplay of these effects may result in an overall enhancement of the fluorescence rates, and can modify the fluorescence lifetimes[23–25] and the spectral shapes of emissions[26–29], which can be controlled by tuning the shapes and sizes of the metal nanoparticles, as well as the relative position and orientation of the emitter with respect to the nanoparticles[11].

The impacts of plasmon resonance on the emission properties of a single fluorophore can be theoretically investigated by solving the classical Maxwell's equations, involving a radiative dipole coupled to the plasmonic structure[10, 13, 17–19]. In this chapter, we evaluate theoretically the performance of gold nanorod based SPR on the fluorescence enhancement of very weak emitters, which are harder to detect at single-molecule level, either because of the very small quantum yields, or because of the very low excitation efficiencies in certain cases, for example two-photon excitation[30]. In the following sections, we will examine the fluorescence enhancement by a single GNR and compare it with the enhancement by a GNR dimer structure, where the GNRs couple strongly with each other. Moreover, we will also investigate the influences of the LSPRs of these plasmonic nanostructures on the fluorescence lifetime and on the shape of the emission spectra. At last, we will investigate the saturation of the fluorescence of a molecule at high excitation, with or without the enhancement by the plasmonic structures.

2.2. Theoretical framework

Two-level scheme of fluorescence enhancement by an antenna

In this thesis, we follow the two-level scheme of Khatua et al[13]. to study the single-molecule fluorescence enhancement by a plasmonic nanoantenna. In this model, the fast internal vibration relaxation is ignored, and the transition rates of the molecule between the ground (g) and exited (e) state are represented by the excitation and the two relaxation rates, as depicted in figure 1. In the absence of the nano-antenna, the time evolution of the probabilities of the molecule at the excited state (p_{e}^{0}) and at the ground state (p_{g}^{0}) can be

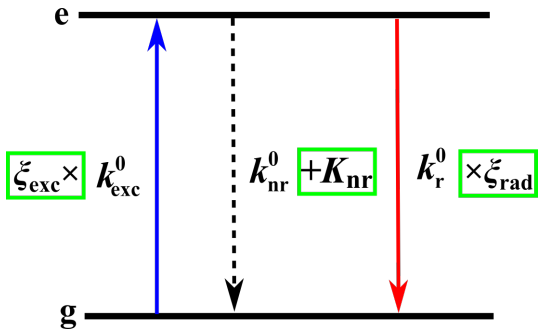

Figure 2.1: Schematic of the transition rates of a molecule in a two-level system, with or without a nanoantenna. Reprinted from Ref[13].

expressed as

$$\begin{aligned} \frac{\mathrm{d}p^0_\mathrm{e}}{\mathrm{d}t} &= k^0_\mathrm{exc} \cdot p^0_\mathrm{g} - (k^0_\mathrm{nr} + k^0_\mathrm{r}) p^0_\mathrm{e} \\ p^0_\mathrm{g} &= 1 - p^0_\mathrm{e}, \end{aligned} \tag{2.1}$$

which, at the steady state condition of $\frac{\mathrm{d}p^0_\mathrm{e}}{\mathrm{d}t} = 0$, gives the equilibrium population of the excited state,

$$p^0_\mathrm{e} = \frac{k^0_\mathrm{exc}}{k^0_\mathrm{exc} + k^0_\mathrm{nr} + k^0_\mathrm{r}}. \tag{2.2}$$

The photon emission rate from the molecule is given by

$$I^0_\mathrm{f} = \frac{k^0_\mathrm{exc} \cdot k^0_\mathrm{r}}{k^0_\mathrm{exc} + k^0_\mathrm{nr} + k^0_\mathrm{r}} = k^0_\mathrm{exc} \cdot \frac{1}{k^0_\mathrm{exc}/k^0_\mathrm{r} + 1/\eta_0}. \tag{2.3}$$

Here, k^0_r and k^0_nr are the radiative and non-radiative rates of the molecule, k^0_exc is the excitation rate, and η_0 represents the quantum yield of the molecule. At low excitation power, where $k^0_\mathrm{exc}/k^0_\mathrm{r} \ll 1/\eta_0$, the emission rate is proportional to the excitation rate: $I^0_\mathrm{f} = k^0_\mathrm{exc} \cdot \eta_0$.

By replacing the transition rates in equation (2.3) with the rates modified by the antenna, we get the enhanced emission rate in the presence of the antenna

$$I_\mathrm{f} = \xi_\mathrm{exc} \cdot k^0_\mathrm{exc} \cdot \frac{\xi_\mathrm{rad}}{\xi_\mathrm{exc} \cdot k^0_\mathrm{exc}/k^0_\mathrm{r} + (\xi_\mathrm{rad} + K_\mathrm{nr}/k^0_\mathrm{r} - 1) + 1/\eta_0}, \tag{2.4}$$

and the overall fluorescence enhancement by the antenna

$$\xi_\mathrm{total} = \xi_\mathrm{exc} \cdot \xi_\mathrm{rad} \cdot \frac{k^0_\mathrm{exc}/k^0_\mathrm{r} + 1/\eta_0}{\xi_\mathrm{exc} \cdot k^0_\mathrm{exc}/k^0_\mathrm{r} + (\xi_\mathrm{rad} + K_\mathrm{nr}/k^0_\mathrm{r} - 1) + 1/\eta_0}. \tag{2.5}$$

Here ξ_exc and ξ_rad are the enhancement factors of the excitation and radiative decay rates, respectively. K_nr is the additional non-radiative absorption rate due to the dissipative losses

of the antenna. Under weak excitation the overall enhancement can be simplified as

$$\xi_{\mathrm{total}} = \xi_{\mathrm{exc}} \cdot \xi_{\mathrm{rad}} \cdot \frac{1/\eta_0}{(\xi_{\mathrm{rad}} + K_{\mathrm{nr}}/k_{\mathrm{r}}^0 - 1) + 1/\eta_0}. \tag{2.6}$$

As a result of the modification of the decay rates by the antenna, the fluorescence of the molecule can be deduced as

$$\frac{\tau}{\tau_0} = \frac{k_{\mathrm{r}}^0 + k_{\mathrm{nr}}^0}{\xi_{\mathrm{rad}} k_{\mathrm{r}}^0 + k_{\mathrm{nr}}^0 + K_{\mathrm{nr}}} = \frac{1/\eta_0}{(\xi_{\mathrm{rad}} + K_{\mathrm{nr}}/k_{\mathrm{nr}}^0 - 1) + 1/\eta_0}. \tag{2.7}$$

Here, for simplicity, we omit the intersystem transitions of the excited molecule to other energy states, which may cause fluorescence blinking, or phosphorescence of the molecules.

Numerical simulations of fluorescence enhancements

The fluorescence enhancement of a single molecule by the plasmonic antenna can be treated classically, provided the molecule is not too close to the metal (sub-nanometer away from the metal surfaces). We consider the molecule as a radiative dipole $\mathbf{p}_0$ oscillating with frequency of ω. As the theoretical absorption rate of the molecule is related to the intensity of the local field at its position, the excitation enhancement factor by the nanoantenna can be expressed as

$$\xi_{\mathrm{exc}}^{(n)} = \frac{|\mathbf{p}_0 \cdot \mathbf{E}(\omega_{\mathrm{exc}})|^{2n}}{|\mathbf{p}_0 \cdot \mathbf{E}_0(\omega_{\mathrm{exc}})|^{2n}}, \tag{2.8}$$

where $\mathbf{E}(\omega_{\mathrm{exc}})$ and $\mathbf{E}_0(\omega_{\mathrm{exc}})$ are the electric fields at the position of the dipole with and without the nanoantenna, ω_{exc} is the frequency of the illuminating light source, and the number $n = 1\ or\ 2$ indicates the excitation with one or two photons, since two-photon absorption depends on the square of the excitation light intensity[31, 32].

To evaluate the enhancement factor by the nanoantenna numerically, we applied a classical electrodynamics approach based on boundary element method (SCUFF-EM) to simulate the excitation and emission enhancements[33, 34].

To get the excitation enhancement, we assumed the antenna is excited by a plane wave and for the calculation of decay rates, we modeled the excited emitter as a radiating dipole, whose time-averaged radiated power in a medium without nanoantenna is[4]

$$P_{r0}(\omega) = \frac{|\mathbf{p}_0|^2}{4\pi\varepsilon_0} \frac{n\omega^4}{3c^3}, \tag{2.9}$$

where n is the refractive index of the medium, c is the speed of light and ε_0 is the vacuum permittivity. The enhancement factor of the radiative rate (ξ_{rad}) and the non-radiative dissipation rate (K_{nr}) by the nanoantenna were derived from

$$\xi_{\mathrm{rad}} = k_{\mathrm{r}}/k_{\mathrm{r}}^0 = P_{\mathrm{rad}}/P_{\mathrm{r0}}, \tag{2.10}$$

and

$$K_{\mathrm{nr}}/k_{\mathrm{r}}^0 = P_{\mathrm{abs}}/P_{\mathrm{r0}}. \tag{2.11}$$

In the simulations, the power absorbed by the antenna P_{abs} was calculated by integrating the Poynting vector over the surface, and the radiated power P_{rad} was obtained from[4]

$$P_{\mathrm{rad}}(\omega) + P_{\mathrm{abs}}(\omega) = \frac{\omega^3}{2c^2\varepsilon_0}|\mathbf{p}_0|^2[\mathbf{n} \cdot \mathrm{Im}[\mathbf{G}(\mathbf{r}, \mathbf{r}; \omega)] \cdot \mathbf{n}], \tag{2.12}$$

where $\mathbf{G}(\mathbf{r}, \mathbf{r}; \omega)$ is the Green tensor at the emitter's position $\mathbf{r}$ and $\mathbf{n}$ represents the direction of the dipole moment.

From Eqs. (S3.12) and (S3.15), we can clearly see that the radiative rate enhancement ($\xi^{\omega}_{\mathrm{rad}}$) and the non-radiative relaxation rate $K^{\omega}_{\mathrm{nr}}(\omega)$ both depend on the frequency of the emitted photons (ω). To get the emission enhancement for all the photons, we calculate the average radiative rate enhancement and non-radiative relaxation rate:

$$<\xi_{\mathrm{rad}}>= \int \xi_{\mathrm{rad}}(\omega)F_{\mathrm{dye}}(\omega)d\omega, \tag{2.13}$$

$$<K_{\mathrm{nr}}>= \int K_{\mathrm{nr}}(\omega)F_{\mathrm{dye}}(\omega)d\omega, \tag{2.14}$$

here, $F_{\mathrm{dye}}(\omega)$ is the normalized emission spectra of the molecule.

2.3. Results and discussion

The most valuable feature of gold nanorod (GNR) dimers compared to single GNR, comes from their outstanding capacity of enhancing ultra-weak signals[35–38]. As an example, we first compare the fluorescence enhancement by an end-to-end GNR dimer with the enhancement by a single GNR.

We start from the strongest coupled dimer configuration, where two identical GNRs are arranged in end-to-end manner with the long axes along each other, shown in figure 2.3a. All GNRs were modeled as a cylinder with two hemispheres at the ends, and their diameters were fixed at a constant value of $40\ \mathrm{nm}$. For the single GNR, the length was set as $115\ \mathrm{nm}$, which gives a longitudinal plasmon resonance of $765\ \mathrm{nm}$. While for the GNR dimer, we adjust the length and the interparticle gap to tune the resonance of the longitudinal-coupled mode to the same plasmon wavelength as the single GNR. In order to have enough space for the molecule to access the near-field hotspot, the GNRs were separated by a gap of $5\ \mathrm{nm}$, and their lengths were adjusted to $90\ \mathrm{nm}$, which ensures the longitudinal plasmon resonance at the wavelength of $765\ \mathrm{nm}$. In the simulations, the dielectric constant for gold was taken from Johnson and Christy, and the refractive index of the ambient medium was taken as 1.33 for water.

For simplicity, the fluorescent molecule was modeled as a point dipole with orientation to be parallel to the polarization of the excitation light, which was aligned with the long axis to get the best excitation. For the single GNR, we placed the molecule at varied positions along the long axis with a certain distance (labeled as 'd' in figure 2.2a) from the tip of the GNR. For the GNR dimer, the position of the molecule is represented by the distance d from the tip of the first GNR (as shown in figure 2.3a) between the two GNRs along the long axes. For both cases, the minimum distance of the molecule away from the gold surface was assumed to be $0.75\ \mathrm{nm}$.

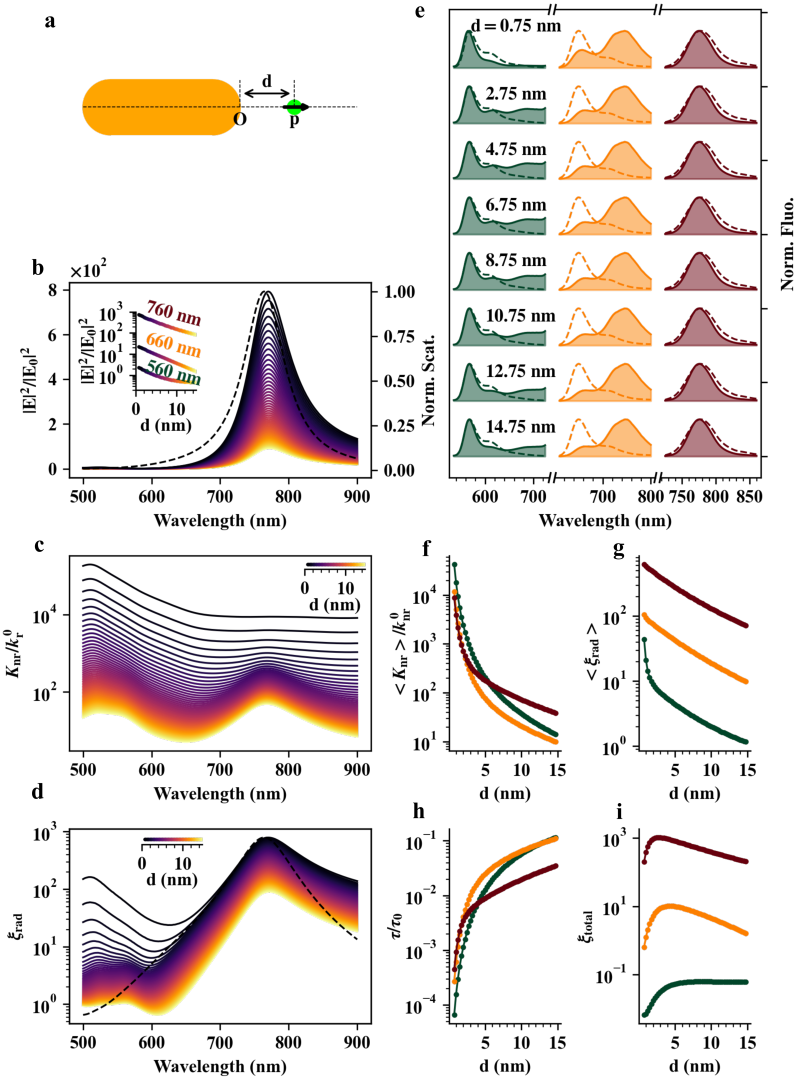

Figure 2.2: Calculated fluorescence enhancement by a single GNR. (a) Scheme of the simulation. (b) Near-field intensity enhancements as a function of the excitation wavelength at different distances. The distance is represented by the color of the line, which corresponds to the d-ordinate of the dots of the same color in the inset. Black dashed line is the normalized scattering spectrum of the GNR. Inset shows the near-field intensity enhancements as a function of d excited at the wavelengths of 760 nm, 660 nm and 560 nm. (c, d) Additional non-radiative rates (c) and radiative enhancements (d) as a function of wavelength at different distances. Dashed line in (d) is the normalized scattering of GNR. (e) Spectral shaping of the spontaneous emissions from three dyes with different emission bands near a single GNR with different separations (labeled by the values of d). Left to right: the original (dashed line) and modified (shaded) emission spectra of Alexa Fluor 555 (dark green), Alexa Fluor 633 (orange) and Alexa Fluor 750 (brown). (f-i) Distance dependence of the averaged additional non-radiative rate (f), radiative enhancement (g), lifetime shortening (h) and overall enhancement (i) for the molecules of Alexa Fluor 555 (dark green), Alexa Fluor 633 (orange) and Alexa Fluor 750 (brown).

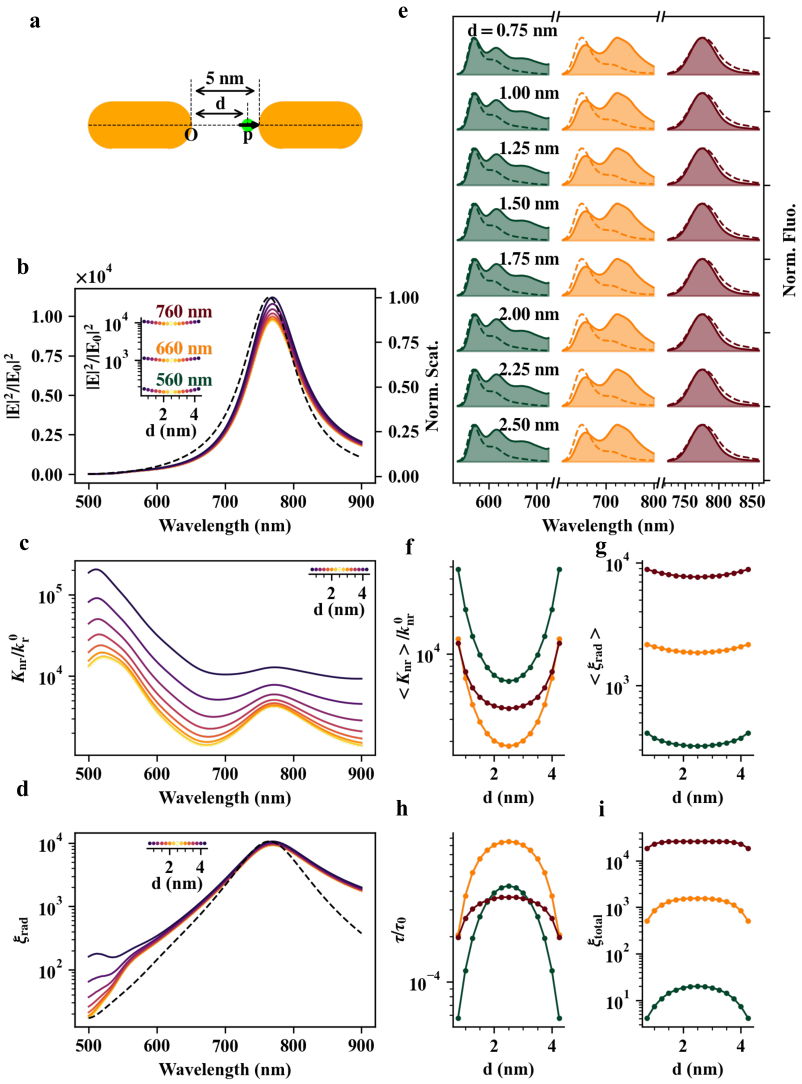

Figure 2.3: Calculated fluorescence enhancement by a GNR dimer. (a) Scheme of the simulation. (b) Near-field intensity enhancements as a function of the excitation wavelength at different positions represented by d, which corresponds to the d-ordinate of the dot in the inset with respect to the line-color. Black dashed line is the normalized scattering spectrum of the GNR dimer. Inset shows the near-field intensity enhancements as a function of d excited at the wavelengths of 760 nm, 660 nm and 560 nm. (c, d) Additional non-radiative rates (c) and radiative enhancements (d) as a function of wavelength at different positions. Dashed line in (d) is the normalized scattering of GNR dimer. (e) Spectral shaping of the spontaneous emissions from three dyes with different emission bands at different positions inside the gap of the GNR dimer (labeled by the values of d). Left to right: the modified (shaded) and original (dashed line) emission spectra of Alexa Fluor 555 (dark green), Alexa Fluor 633 (orange) and Alexa Fluor 750 (brown). (f-i) Position dependence of the averaged additional non-radiative rate (f), radiative enhancement (g), lifetime shortening (h) and overall enhancement (i) for the molecules of Alexa Fluor 555 (dark green), Alexa Fluor 633 (orange) and Alexa Fluor 750 (brown).

Enhancement of near-field intensity : Single GNR vs GNR dimer

Under weak excitation, the fluorescence enhancement can be treated as the product of the excitation enhancement and the emission enhancement. We first discuss the excitation enhancement upon one-photon absorption, which can be represented as the near-field intensity enhancement in the parallel-excited condition. Figure 2.3b shows the intensity enhancement of the near-field by the GNR dimer as a function of the excitation wavelength and of the molecular position (inset). For comparison, we also calculate the near-field intensity enhancement by a single GNR for different molecule-tip separations in figure 2.2b. From the plots, we can see that the intensity enhancement spectra of both structures are slightly red-shifted compared to the scattering spectra (from $765\ \mathrm{nm}$ to $770\ \mathrm{nm}$), and their shapes show clear asymmetric profiles, with the red wings decreasing slower than the blue wings as the excitation was detuned away from the resonant excitation. Such differences can be explained as the results of plasmonic damping and the dephasing between the near-field and the far-field responses of the structures.

Apparently, the near-field enhancement by a single GNR depends strongly on the position of the molecule with respect to the gold surface. As the molecule moves away from the tip of the GNR, the near-field enhancement decreases rapidly. Therefore, the effective excitation enhancement by a single GNR is only localized to a small volume near the tip. The GNR dimer provides a more uniform near-field hotspot with larger enhancement factor between the gap, which is distributed symmetrically along the long axis. From figure 2.2b, we can see the enhancement of near-field intensity by a single GNR in resonance drops monotonically from 7.9×10^2 to 3.6×10^2 as the GNR-molecule distance increases from $0.75\ \mathrm{nm}$ to $5\ \mathrm{nm}$. For the GNR dimer, however, the enhancement of the near-field intensity shows little change inside the gap. As shown in figure 2.3b, the enhancement factor decreases slightly from 1.0×10^4 to 0.9×10^4 as the molecule moves away from one tip at the distance of $0.75\ \mathrm{nm}$ toward the center of the dimer.

Additionally, GNR dimer performs better for the near-field enhancement excited at the wavelength out of the plasmon resonance. As an example, we compared the enhancement of the near-field intensity by the single GNR and by the GNR dimer at different excitation wavelengths as shown in the insets of figures 2.2a and 2.3a, respectively. We can see that the near-field intensity enhancement by the single GNR, for $d = 0.75\ \mathrm{nm}$, decreased from 730 to 23 and 2.3 as the excitation wavelength was detuned from $760\ \mathrm{nm}$ to $660\ \mathrm{nm}$ and $560\ \mathrm{nm}$, respectively. On the other hand, for the dimer the relative enhancement factor at these wavelengths drops from 1.1×10^4 to 1.1×10^3 and 1.7×10^2, respectively.

Non-radiative and radiative rates enhancement : Single GNR vs GNR dimer

Next, we examine the emission enhancement of the fluorescent molecule by the single GNR and by the GNR dimer. Unlike the excitation enhancement, where the near-field enhancement is due to the plasmon modes excited by a plane wave, the emission enhancement concerns the plasmon oscillation induced by a point-like dipole source, which may introduce different coupling channels to the plasmon modes. For instance, as the result of symmetry breaking, it may be easier for the dipole to excite the higher order modes or 'dark' modes of the plasmon structures compared to plane waves. As it was mentioned before, the influence of plasmon resonance on the emission properties of the dipole can be described by the enhancement of the radiative rates (ξ_{rad}) and the additional non-radiative rates ($K_{\mathrm{nr}}/k_{\mathrm{r}}^0$).

As shown in figures 2.2c and 2.3c, for both the single GNR and the GNR dimer, two major additional non-radiative absorption bands exist for the excited molecule. The first absorption band is due to the excitation of the longitudinal plasmon mode with the peak at wavelength of $770\ \mathrm{nm}$. The other one is at the high energy range with the peak at $510\ \mathrm{nm}$ which can be viewed as the result of the excitation of high-order modes. The excitation of the high-order modes and their coupling with far-field or other plasmonic modes, strongly depend on the excitation wavelength, the curvature of the gold surface and the distance of the dipole source from the surface. When the molecule is placed very close to the tip of the GNR (or close to the tip of one GNR in the case of the dimer), the additional dissipation channels are dominated by the high-order absorption modes. As the molecule moves away from the tip, the high-order absorption decreases more rapidly than the absorption due to the SPR, leaving two distinguishable peaks at wavelengths of $510\ \mathrm{nm}$ and $770\ \mathrm{nm}$ for both single GNR and GNR dimer.

To investigate the radiative rate enhancement, we need to consider not only the excitation of the plasmon modes by a dipole source, but also the coupling of these modes with the far fields. Different from the coupling with the point-like dipole source near by, low order plasmon modes with longer resonant wavelengths couple more efficiently with the far fields. This statement can be confirmed by the dominant peaks of the radiative enhancements at the wavelength of $770\ \mathrm{nm}$, as is shown in figures 2.2d and 2.3d, which correspond to the longitudinal plasmon resonances of singe GNR and GNR dimer, respectively. At this wavelength, due to the strong plasmon coupling between the GNRs, the radiative rate of the molecule inside the gap of the dimer can be enhanced by a factor of about 10^4, which is more than one order higher than the enhancement by a single GNR for the molecule separated by similar distance from the tip. From the spectra, we also see a small peak at $510\ \mathrm{nm}$ for both cases as the molecule is placed very close to the GNR's tip. This peak vanishes very quickly as we increase distance of the molecule from the GNR's tip. Additionally, for the radiative rate enhancement by the GNR dimer, we see more features in range between the two main modes compared to single GNR, which can be viewed intuitively as due to the excitation of other hybrid modes of the GNR dimer (except the longitudinal SPR) by the molecule.

Specifically, we notice that the high-order modes excited at the short wavelength of $510\ \mathrm{nm}$ are strongly localized modes. As a consequence, the excitation of this high-order modes is not influenced by the length of the GNR. From figure 2.4a, we can see that the additional non-radiative absorption at the wavelength of $510\ \mathrm{nm}$ by single GNR is not dependent on the length of the GNR. As the molecule moves away from the GNR's tip, the high-order absorption peaks by the single GNR decrease about two orders faster compared to the absorption at the SPRs of each GNR shown in figure 2.4b, indicating that the interaction length scale of the high order modes is about two-order smaller than the dipole-like longitudinal plasmon modes. From figure 2.4a, we also see that, for the GNR dimer, as the molecule inside the gap is placed very close to one of the two GNRs (e.g. $d \leq 1.5\ \mathrm{nm}$), the existence of the other GNR does not influence the values of additional non-radiative rates, which confirms the interaction length scales of these high order modes are absolutely short. Similar behaviour can be seen for the radiative rate enhancements for the single GNR and GNR dimer at the wavelength of $510\ \mathrm{nm}$, shown in figure 2.4c, where we don't see significant difference in the enhancement factors for all the structures, while the molecule is closer to GNR's tip. As a comparison, for radiative rate at SPR's wavelength, the enhancement

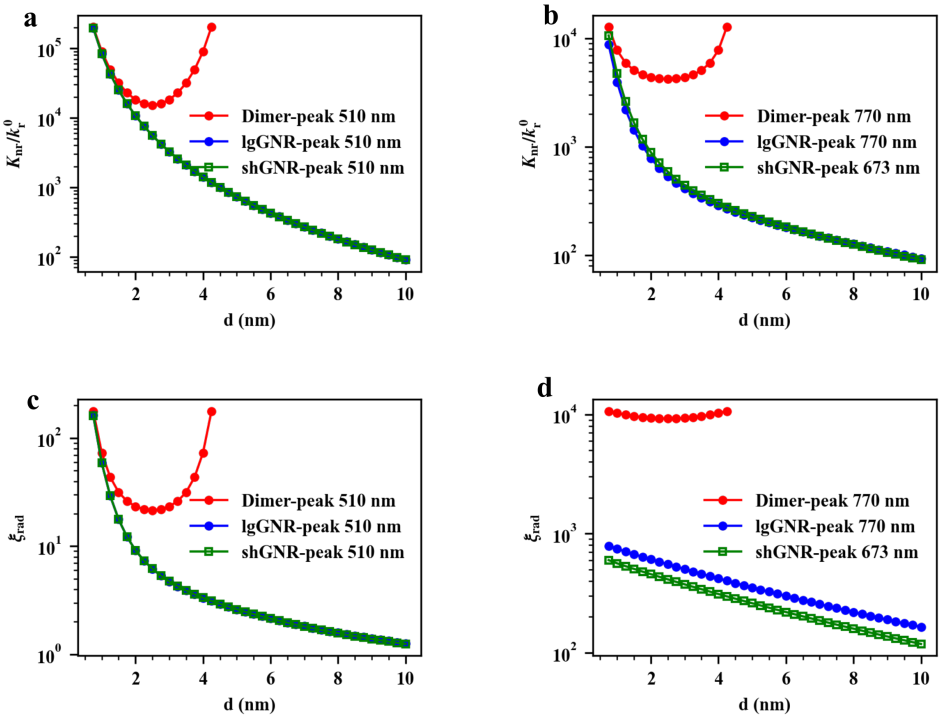

Figure 2.4: Comparisons of the additional non-radiative rates (a, b) and the radiative enhancements (c, d) at the wavelengths of 510 nm (a, c) and 770 nm (b, d), with the enhancements by a GNR dimer and by two single GNR of different lengths. The shorter single GNR (shGNR) with SPR of 670 nm has similar length as the individual GNR of the dimer, and the longer GNR (lgGNR) and the GNR dimer have same resonant wavelength of 765 nm.

factor by the GNR dimer can be more than one-order higher than the enhancement by a single GNR, as is shown in figure 2.4d.

Fluorescence enhancement of the dyes with different emission bands : Single GNR vs GNR dimer

So far, we have provided a detailed description of the influence of plasmon resonance on the excitation and radiation of a dipole emitter by exploiting a single GNR and a longitudinally arranged GNR dimer. To investigate the overall fluorescence enhancement of a dye molecule, we need to involve the influences of the intrinsic non-radiative decay of the molecule, and of the spectral overlaps of the molecular absorption and emission with the SPR. For a dye with specific absorption and emission bands, the well known strategy to get best fluorescence enhancement is to tune the plasmon resonance by adjusting its size to ensure best spectral overlaps between the SPR and the absorption and emission bands of the molecule.

Herein, we will compare the fluorescence enhancements by the aforementioned single GNR and GNR dimer for three dyes with very different absorption and emission bands: the Alexa Fluor 555, Alexa Fluor 633 and Alexa Fluor 750. They have similar quantum yield of 10% and different maximum absorption peaks at the wavelengths of $555\ \mathrm{nm}$, $633\ \mathrm{nm}$ and $750\ \mathrm{nm}$, respectively. Instead of tuning the plasmon resonances to get best fluorescence enhancements, we will use the same structures to investigate the enhancement of these three dyes under the excitation wavelengths of $560\ \mathrm{nm}$, 660 and $760\ \mathrm{nm}$, respectively. In the case of one-photon excitation, we lose both excitation and emission enhancement for the two dyes Alexa Fluor 555 and Alexa Fluor 633, which are off-resonance with the plasmonic structures. Yet the discussions about the spectral shaping and lifetime shortening by the GNR structures will be very valuable for the study of fluorescence enhancement under two-photon excitation, as the two-photon absorption bands for common dyes are normally in the infrared region and their excitation rates can be significantly enhanced by our structures, especially by the GNR dimers.

Spectral shaping of the spontaneous emission

One notable feature of the plasmon-emitter system is that the line-shape of the emission spectrum of the molecule can be modified, since different spectral components of the emission will be selectively enhanced according to the plasmonic modes. Here, we illustrate the modification of the emission spectra of the three dyes with very different emission bands by the single GNR and by the GNR dimer.

First, we have a look at the dye Alexa Fluor 750, which has the emission peak (brown dashed lines in figures 2.2e and 2.3e) overlapped with the LSPR. Due to maximum enhancement at the peaks, we see similar sharpened profiles for the enhanced emissions (brown shaded area) for both single GNR and GNR dimer, as shown in figures 2.2e and 2.3e respectively. Secondly, for Alexa Fluor 633 dye with the emission maximum at $639\ \mathrm{nm}$ (orange dashed lines in figures 2.2e and 2.3e), we see significant red-shift for the emission peaks, enhanced by the single GNR and by GNR dimer, which can be regard as the enhancement of the emission tail by the longitudinal SPR modes of the nanostructures. Yet, due to other enhancement channels according to the hybridized plasmon modes of the GNR dimer, we

see the maximum peak for GNR dimer is located at $724\ \mathrm{nm}$, which is shorter than the peak of $746\ \mathrm{nm}$ for the single GNR. For the similar reason, we see the other peak with slightly smaller value at the wavelength of $658\ \mathrm{nm}$ for GNR dimer. Finally, for Alexa Fluor 555 with the emission peak at $568\ \mathrm{nm}$, we see from figure 2.2e that, at short distance ($d = 0.75\ \mathrm{nm}$) from single GNR, the emission enhancement at the longer wavelength is suppressed by the emission enhancement corresponding to the high-order modes excited at the shorter wavelength. As the molecule moves away from the tip, the enhancement due to high-order modes decrease very fast, and we see emission tail is lifted by the enhancement caused by the LSPR at longer wavelength. For GNR dimer, we see the longer wavelength enhancement for the emission rise up, which can be attributed to the hybridized modes of GNR dimer.

One-photon excited fluorescence enhancement

Since the plasmonic enhancement of the decay rates of the molecules are highly dependent on the exact positions of the spectra, we will approximate the radiative rate enhancement (ξ_{rad}) and the additional non-radiative rate (K_{nr}) for each dye by taking the average of the enhancement factors over the emission spectra of the dyes.

Expectantly, for single GNR, as the dye molecule gets very close to GNR's tip, the decay rate is dominated by the additional non-radiative rate. Shown in figure 2.2f, we see large non-radiative rates ($\sim 10^4$) for the three dyes for small separation ($d \sim 1\ \mathrm{nm}$). The rates drop rapidly as the separation of the dye from the GNR increases. Specifically, at short distance, we obverse largest $< K_{\mathrm{nr}} >$ for Alexa Fluor 555 (green dotted line), which has the strongest emission overlap with short-wavelength absorption band of the GNR, while at larger distance (e.g. $d > 6\ \mathrm{nm}$), Alexa 750 (brown dotted line), having reddest emission band, exhibits the largest non-radiative rate, due to its strongest spectral overlap with the longitudinal SPR. The radiative rate enhancements ($< \xi_{\mathrm{rad}} >$) for the dyes, however, are mainly correlated with the spectral overlaps between their emission bands and the LSPR. As shown in figure 2.2g, at short distance ($d \sim 1\ \mathrm{nm}$), we see the enhancement factors of 6×10^2, 1×10^2 and 4×10^1 for the radiative rates of Alexa Fluor 750, 633 and 555, respectively. For the dimer, as shown in figure 2.3f, the magnitude of non-radiative rates for the dyes are similar to the case of the single GNR ($\sim 10^4$). And, for the radiative decay rates, we see about one order higher enhancement factors for each dye inside the gap of the dimer (figure 2.3g), compared to the enhancement factors by the single GNR when the dyes are very close to the GNR.

The stronger near-field enhancement by the GNR dimer, together with the stronger radiative enhancement, leads to a larger overall enhancement of the fluorescence of the dye inside the gap of the dimer. As shown in figure 2.3i, for Alexa Fluor 750 dye with emission resonant with the longitudinal SPR, we see a maximum overall fluorescence enhancement factor of about 2.6×10^4 inside the gap of the GNR dimer. For the other two dyes, Alexa Fluor 633 and 555, both having absorption bands and emission bands out of resonance with longitudinal SPR, we get enhancement factors of 1.5×10^3 and 20, excited at the off-resonance wavelengths of $660\ \mathrm{nm}$ and $560\ \mathrm{nm}$, respectively. As a comparison, for single GNR, the over enhancement factor for the three dyes are 10^3, 10^0 and 10^{-2}, respectively, as is depicted in figure 2.2i.

Fluorescence lifetime reduction

A direct consequence of the overall enhancements of the radiative decay rate and non-radiative decay rate of a molecule is the reduction of its fluorescence lifetime. Lifetime shortening is crucial for the single-molecule study of an emitter with very long fluorescence lifetime. Here we find that fluorescence lifetime can be strongly reduced in the vicinity of GNR's tip. As depicted in figures 2.2h and 2.3h, for single GNR and GNR dimer, respectively, we see about four-order reduction for the lifetimes of all the three dyes, as the molecule gets close to the GNR's tip ($\mathrm{d} \sim 1\mathrm{nm}$). For single GNR, the lifetime reduction of the molecule is mainly due to the additional non-radiative decay rates, hence the strong lifetime reduction is only restricted to a very tiny region near the GNR's tip. As can be seen in figure 2.2h, the lifetime reduction factors for the dyes increase rapidly to the magnitude of about 10^{-2} as the molecules move away from the tip by a small distance (at the position: $d \sim 3\ \mathrm{nm}$). For GNR dimer, however, the strong lifetime reduction factor at different position inside the gap do not change significantly. As depicted in figure 2.3h, the reduction factor remains in the range of $10^{-4} \sim 10^{-3}$ for all the dyes in the center of the gap.

Two-photon-excited fluorescence enhancement

Another potential application of gold-nanorod based plasmonic structures is to enhance two-photon-excited fluorescence of a molecule. Unlike the one-photon excited fluorescence, two-photon-excited fluorescence is a nonlinear optical process where the excitation of the molecule is due to the absorption of two identical photons, hence the excitation rate is proportional to the square of the incident light intensity: $k_{\mathrm{exc}}^{(2)} = \sigma^{(2)} I_{\mathrm{exc}}^2$. As a consequence, we would expect higher excitation enhancement for two-photon-excited fluorescence than one-photon counterpart in the near-field hotspots, since the enhancement factor is dependent on the square of the near-field intensity. Additionally, two-photon excitation extends the absorption band into longer wavelength, usually in the infrared range, which can be well overlapped with SPR band of GNR to achieve the maximum enhancement for two-photon-excited fluorescence.

Here, we compare the two-photon-excited fluorescence enhancement by the aforementioned single GNR and GNR dimer. We focus on the two dyes, Alexa Fluor 633 and Alexa Fluor 555, since both have two-photon absorption in the infrared range. In the simulation, the excitation wavelength was set as $770\ \mathrm{nm}$ to ensure best excitation enhancement. The emission spectra and the quantum yields of the dyes under two-photon excitation are considered the same as one-photon excited fluorescence.

Figure 2.5 gives the overall fluorescence enhancements for two dyes under two-photon excitation, by the single GNR and by the GNR dimer. From the plot, we see a maximum enhancement factor of about 10^5 for Alexa 633 molecule (orange circles) by a single GNR, while by GNR dimer, the enhancement factor can be as strong as 10^8 (orange dots). The improvement of the overall enhancement by GNR dimer comes from the strong plasmonic coupling between the two GNRs. This causes stronger enhancement for both the excitation rate and radiative rate of the dye, compared to the single GNR. For Alexa Fluor 555, which has shorter wavelength emission band, we see smaller enhancements by GNR dimer ($\sim 10^7$, green dots) and by single GNR ($\sim 10^4$, green circles), which can be attributed to the stronger quenching effects due to additional non-radiative absorption by the gold.

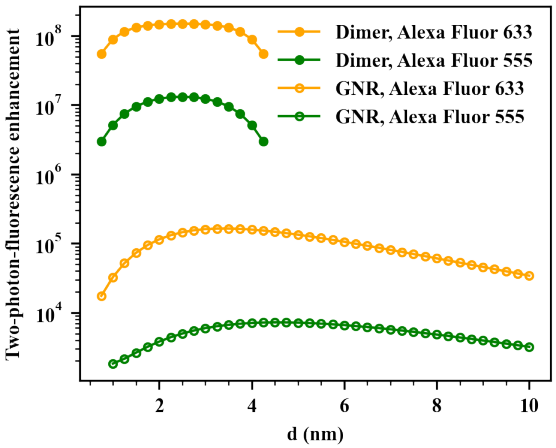

Figure 2.5: Two-photon-excited fluorescence enhancement by a single GNR and by a GNR dimer for two dyes, Alexa Fluor 633 and Alexa Fluor 555.

Saturation of one/two-photon-excited fluorescence enhanced by single GNR or by GNR dimer

In previous discussions, we considered the fluorescence enhancement under very weak excitation, where the processes of excitation and emission can be treated independently. In this case, the emission rate is proportional to the excitation rate of the molecule. As the excitation continue to increase, we will see saturation behavior for the emission rate[4, 30, 39, 40]. For free dye, as the molecule is excited by very high power ($k_{\mathrm{exc}} \to \infty$), from Eq (2.3), we see a limited rate $I^0_{\mathrm{f},\infty} \to k^0_{\mathrm{r}}$ for the emission rate of the free dye, which means the emission rate is limited by the intrinsic radiating rate of the dye (k^0_{r}). Enhanced by the plasmonic structure, the saturated emission rate of the dye is $I_{\mathrm{f},\infty} \to <\xi_{\mathrm{rad}}> \cdot k^0_{\mathrm{r}}$. Therefore, the saturated overall fluorescence enhancement is $<\xi_{\mathrm{rad}}>$, which represents the averaged radiative enhancement of dye by the plasmon structures.

Following the strategy of the book (Principle of Nano-optics) by Novotny and Hecht [4]), the saturation behavior of the molecule can be characterized by the parameter I_{s}. For a free dye, $I_{\mathrm{s}} = k^0_{\mathrm{r}}/\eta_0 = \tau_0^{-1} = k^0_{\mathrm{D}}$, where k^0_{D} and τ_0 are the intrinsic decay rate and intrinsic lifetime of the dye, respectively. For the dye enhanced by a plasmonic structure,

$$I_{\mathrm{s}} = \frac{<\xi_{\mathrm{rad}} + K_{\mathrm{nr}}/k^0_{\mathrm{r}} - 1> \cdot \eta_0 + 1}{\xi_{\mathrm{exc}}} \cdot k^0_{\mathrm{D}}, \tag{2.15}$$

where $< \cdots >$ represents the average over the emission spectrum. Here, I_{s} characterises the saturated excitation power, at which the emission rate equals to half of the saturated emission rate. Obviously, the saturated excitation rate of the molecule, with or without the plasmonic structure, is proportional to the ratio of the total decay rates over the excitation rates.

Next, we investigate the saturation of the fluorescence enhanced by a single GNR and by the GNR dimer. In this study, we represented the enhancements of the decay rates (ξ_{rad} and

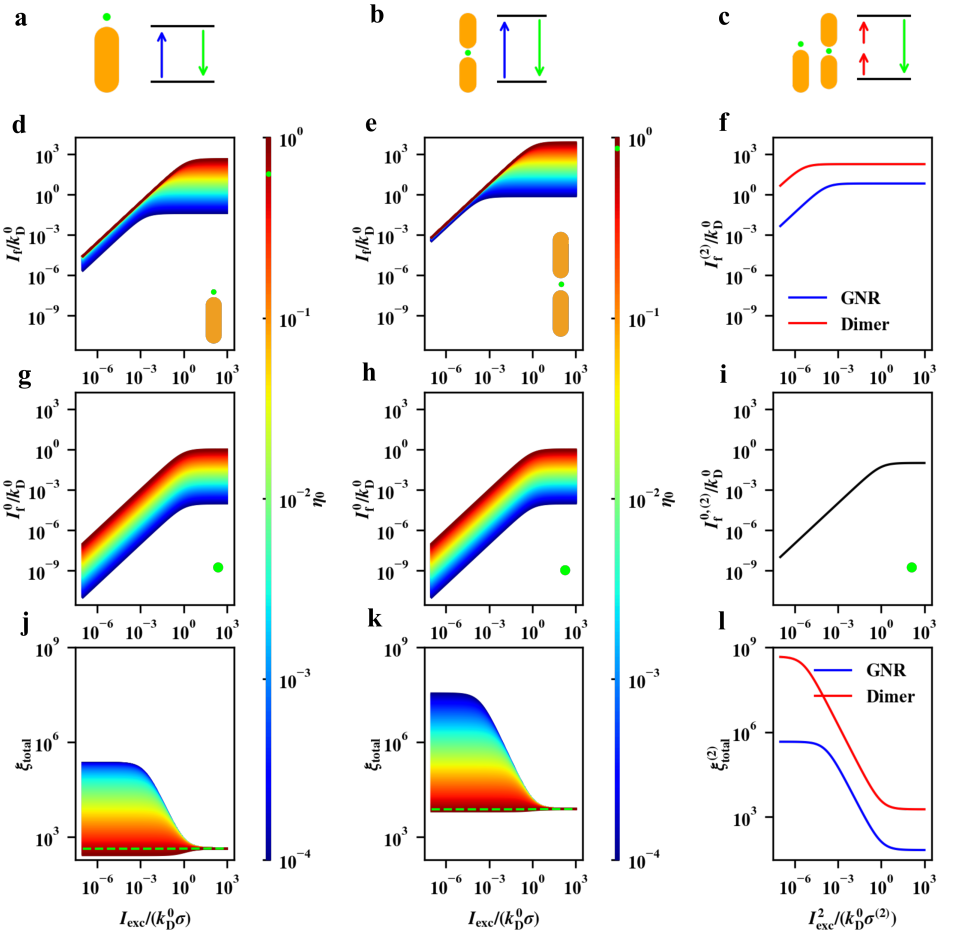

Figure 2.6: Fluorescence saturation under one-photon and two-photon excitation. (a, b, c) Schemes of the simulations for one-photon excited fluorescence enhanced by a single GNR (a) and by a GNR dimer (b), for two-photon-excited fluorescence enhanced by the single GNR and GNR dimer (c). For all cases, the distance from GNR's tip was set as 2.5 nm and the excitation wavelength was set as 765 nm. (d, e, g, h, j, k) Saturation of the one-photon excited fluorescence for single dye molecule with different quantum yields. (d, e, g, h) Excitation power dependence of the one-photon fluorescence with (d, e) or without (e ,h) the enhancement by single GNR (d) or by GNR dimer (e). (j, k) Overall fluorescence enhancement by single GNR (j) or by the GNR dimer (k). Green dashed lines in (j, k) represent the dyes that have constant enhancement factor for all excitation powers by single GNR (j) or by GNR dimer (k), with the quantum yields corresponding to the green dots in the colorbars. Here, for simplicity, we assumed the dyes with different quantum yields have similar one-photon absorption cross section of σ, and their emission spectra were all represented by the emission of Alexa Fluor 750 in the simulations. (f, i, l) Saturation of two-photon-excited fluorescence of a single molecule of Alexa Fluor 633. (f, i) Power dependence of two-photon fluorescence rates with (f) or without (i) the enhancement by single GNR or by GNR dimer. (l) Power dependence of two-photon fluorescence enhancement by single GNR or by GNR dimer.

$K_{\mathrm{nr}}/k_{\mathrm{r}}^0$) with the averaged enhancement factors for a single molecule of Alexa Fluor 750. The molecule was placed at the position of $d = 2.5$ nm from the GNR's tip, or placed at the center of the dimer's gap, as is shown in figures 2.6a, and 2.6b. The excitation enhancement factors were considered as the enhancements of the near-field intensities excited at the wavelength of 770 nm.

We show the fluorescence rate of the molecule as a function of the excitation rate in figures 2.6d, 2.6e, 2.6g, and 2.6h, with (d and e) or without (g and h) the enhancement by single GNR and GNR dimer, respectively. As an assumption, we varied the quantum yield of the molecule from 10^{-4} to 1 to investigate the emission saturation for the dyes with different quantum yield, keeping the intrinsic decay rate ($k_{\mathrm{D}}^0 = 1/\tau_0$) of the dye and the emission spectrum as constant. As expected and shown in the plots, the fluorescence rate depends linearly on the excitation rate for small excitation intensities. At high excitation rate, the emission intensities approach the saturated rates, which could be ether $< \xi_{\mathrm{rad}} > \cdot k_{\mathrm{D}}^0 \cdot \eta_0$ or $k_{\mathrm{D}}^0 \cdot \eta_0$, depending on whether the dye is enhanced or not by the plasmonic structures. Interestingly, from figures 2.6d and 2.6e, we see that the dye with smaller quantum yield is easier to be saturated under the enhancement of the single GNR or the dimer, based on the assumption of similar intrinsic decay rate for all quantum yields.

We compare the overall fluorescence enhancements by the single GNR and by the GNR dimer for the dyes with different quantum yields in figures 2.6j and 2.6k, respectively. For each plasmonic structure, below saturation, the fluorescence enhancement factor does not depend on the excitation power, yet it does depend on the quantum yield of the molecule. It turns out that the overall fluorescence enhancement is larger for the dye with smaller quantum yield. Specifically, the enhancement factor $\xi_{\mathrm{total}} \rightarrow \xi_{\mathrm{exc}} \cdot < \xi_{\mathrm{rad}} >$, as the quantum yield $\eta_0 \rightarrow 0$. Here, ξ_{exc} is the excitation enhancement by the plasmon mode. Above saturation, however, the overall enhancement for all quantum yields approaches to the same enhancement factor of $< \xi_{\mathrm{rad}} >$. By having a closer look at Eq (2.5), we find that for the dye with the quantum yield of

$$\eta_0 = \frac{\xi_{\mathrm{exc}} - 1}{< \xi_{\mathrm{rad}} + K_{\mathrm{nr}}/k_{\mathrm{r}}^0 - 1 >}, \tag{2.16}$$

we see a constant enhancement factor of ξ_{rad} for all excitation powers, which can be confirmed by the straight lines (green dashed) in figure 2.6j and 2.6k.

Finally, it is also of interest to investigate the saturation of two-photon-excited fluorescence, with the enhancement by the single and dimer GNR. As an example, we considered the Alexa Fluor 633 dye excited at the wavelength of 770 nm. Similar to one-photon case, the molecule was placed at the position of $d = 2.5$ nm from the GNR's tip, or placed at the center of the dimer's gap, as shown in figure 2.6c. Due to the stronger excitation enhancement, the fluorescence enhanced by the GNR dimer is saturated at smaller excitation intensity, compared to the single GNR (figure 2.6f). The expected fluorescence rates, excited at high power, are also limited to the saturated emission rates of $< \xi_{\mathrm{rad}} > \cdot k_{\mathrm{D}}^0 \cdot \eta_0$ for both structures. At weak excitation, we see much stronger fluorescence enhancement under two-photon excitation compared to one-photon excitation, which is about 10^8 by the GNR dimer, and 10^5 by the single GNR, as shown in figure 2.6l. The saturated fluorescence enhancement, however, is the same factor of $< \xi_{\mathrm{rad}} >$ for both two-photon excitation and one-photon excitation, which is the averaged enhancement factor of the radiative rate of the dye by the plasmonic structure.

2.4. Conclusions

In conclusion, we theoretically investigated the fluorescence enhancement by a single GNR and by an end-to-end GNR dimer. Compared to single GNR, the GNR dimer with end-to-end configuration provides stronger enhancements for both near-field intensity and radiative rate of a dipole. At low excitation power, the stronger near-field enhancement, together with the stronger radiative enhancement, will introduce much higher overall fluorescence enhancement of a single molecule, especially for the two-photon-excited fluorescence, since two-photon excitation depends quadratically on the excitation intensity. For a GNR dimer with interparticle gap of $5\ \mathrm{nm}$, we got enhancement factor of 10^4 for the dye with well spectral overlapping with the SPR under one photon excitation, which is more than 10 times higher than the enhancement by the single GNR. For two-photon-excited fluorescence, the enhancement can reach up to the factor of 10^8 by GNR dimer, while for single GNR, the maximum enhancement factor is about 10^5. Accompanied with the fluorescence enhancement, we also saw significant spectral shaping and lifetime shortening for the fluorescence of the molecule. Finally, we examined the fluorescence saturation under the enhancement of single GNR and GNR dimer. Theoretical analysis showed that, at very high excitation power, the enhanced fluorescence rate from a single molecule will be saturated to a limited value, which is determined by the intrinsic radiative rate of the molecule, enhanced by the factor of the radiative enhancement by the plasmonic structure.

References

[1] Heinz Raether. Surface plasmons. *Springer Tracts in Modern Physics*, 111:1, 1988.

[2] Uwe Kreibig and Michael Vollmer. *Optical properties of metal clusters*, volume 25. Springer Science & Business Media, 2013.

[3] Craig F Bohren and Donald R Huffman. *Absorption and scattering of light by small particles*. John Wiley & Sons, 2008.

[4] Lukas Novotny and Bert Hecht. *Principles of nano-optics*. Cambridge university press, 2012.

[5] Jon A. Schuller, Edward S. Barnard, Wenshan Cai, Young Chul Jun, Justin S. White, and Mark L. Brongersma. Plasmonics for extreme light concentration and manipulation. *Nature Materials*, 9(3):193–204, March 2010.

[6] Surbhi Lal, Stephan Link, and Naomi J. Halas. Nano-optics from sensing to waveguiding. *Nature Photonics*, 1(11):641–648, November 2007.

[7] Palash Bharadwaj, Pascal Anger, and Lukas Novotny. Nanoplasmonic enhancement of single-molecule fluorescence. *Nanotechnology*, 18(4):044017, December 2006.

[8] Pascal Anger, Palash Bharadwaj, and Lukas Novotny. Enhancement and Quenching of Single-Molecule Fluorescence. *Physical Review Letters*, 96(11):113002, March 2006.

[9] Anika Kinkhabwala, Zongfu Yu, Shanhui Fan, Yuri Avlasevich, Klaus Müllen, and W. E. Moerner. Large single-molecule fluorescence enhancements produced by a bowtie nanoantenna. *Nature Photonics*, 3(11):654–657, November 2009.

[10] S. Sun, L. Wu, P. Bai, and C. E. Png. Fluorescence enhancement in visible light: Dielectric or noble metal? *Physical Chemistry Chemical Physics*, 18(28):19324–19335, July 2016.

[11] Guowei Lu, Tianyue Zhang, Wenqiang Li, Lei Hou, Jie Liu, and Qihuang Gong. Single-Molecule Spontaneous Emission in the Vicinity of an Individual Gold Nanorod. *The Journal of Physical Chemistry C*, 115(32):15822–15828, August 2011.

[12] Haifeng Yuan, Saumyakanti Khatua, Peter Zijlstra, Mustafa Yorulmaz, and Michel Orrit. Thousand-fold Enhancement of Single-Molecule Fluorescence Near a Single Gold Nanorod. *Angewandte Chemie*, 125(4):1255–1259, 2013.

[13] Saumyakanti Khatua, Pedro M. R. Paulo, Haifeng Yuan, Ankur Gupta, Peter Zijlstra, and Michel Orrit. Resonant Plasmonic Enhancement of Single-Molecule Fluorescence by Individual Gold Nanorods. *ACS Nano*, 8(5):4440–4449, May 2014.

[14] Anastasiya Puchkova, Carolin Vietz, Enrico Pibiri, Bettina Wünsch, María Sanz Paz, Guillermo P. Acuna, and Philip Tinnefeld. DNA Origami Nanoantennas with over 5000-fold Fluorescence Enhancement and Single-Molecule Detection at 25 μM. *Nano Letters*, 15(12):8354–8359, December 2015.

[15] Deep Punj, Raju Regmi, Alexis Devilez, Robin Plauchu, Satish Babu Moparthi, Brian Stout, Nicolas Bonod, Hervé Rigneault, and Jérôme Wenger. Self-Assembled Nanoparticle Dimer Antennas for Plasmonic-Enhanced Single-Molecule Fluorescence Detection at Micromolar Concentrations. *ACS Photonics*, 2(8):1099–1107, August 2015.

[16] Biswajit Pradhan, Saumyakanti Khatua, Ankur Gupta, Thijs Aartsma, Gerard Canters, and Michel Orrit. Gold-Nanorod-Enhanced Fluorescence Correlation Spectroscopy of Fluorophores with High Quantum Yield in Lipid Bilayers. *The Journal of Physical Chemistry C*, 120(45):25996–26003, November 2016.

[17] Weichun Zhang, Martín Caldarola, Xuxing Lu, Biswajit Pradhan, and Michel Orrit. Single-molecule fluorescence enhancement of a near-infrared dye by gold nanorods using DNA transient binding. *Physical Chemistry Chemical Physics*, 20(31):20468–20475, 2018.

[18] Pedro M. R. Paulo, David Botequim, Agnieszka Jóskowiak, Sofia Martins, Duarte M. F. Prazeres, Peter Zijlstra, and Sílvia M. B. Costa. Enhanced Fluorescence of a Dye on DNA-Assembled Gold Nanodimers Discriminated by Lifetime Correlation Spectroscopy. *The Journal of Physical Chemistry C*, 122(20):10971–10980, May 2018.

[19] Xuxing Lu, Gang Ye, Deep Punj, Ryan C. Chiechi, and Michel Orrit. Quantum Yield Limits for the Detection of Single-Molecule Fluorescence Enhancement by a Gold Nanorod. *ACS Photonics*, 7(9):2498–2505, September 2020.

[20] E. M. Purcell, H. C. Torrey, and R. V. Pound. Resonance Absorption by Nuclear Magnetic Moments in a Solid. *Physical Review*, 69(1-2):37–38, January 1946.

[21] Daniel Kleppner. Inhibited Spontaneous Emission. *Physical Review Letters*, 47(4):233–236, July 1981.

[22] W. L. Barnes. Fluorescence near interfaces: The role of photonic mode density. *Journal of Modern Optics*, 45(4):661–699, April 1998.

[23] Joseph R Lakowicz. *Principles of fluorescence spectroscopy*. Springer science & business media, 2013.

[24] Alexander Huck, Shailesh Kumar, Abdul Shakoor, and Ulrik L. Andersen. Controlled Coupling of a Single Nitrogen-Vacancy Center to a Silver Nanowire. *Physical Review Letters*, 106(9):096801, February 2011.

[25] Ling Xin, Mo Lu, Steffen Both, Markus Pfeiffer, Maximilian J. Urban, Chao Zhou, Hao Yan, Thomas Weiss, Na Liu, and Klas Lindfors. Watching a Single Fluorophore Molecule Walk into a Plasmonic Hotspot. *ACS Photonics*, 6(4):985–993, April 2019.

[26] M. Ringler, A. Schwemer, M. Wunderlich, A. Nichtl, K. Kürzinger, T. A. Klar, and J. Feldmann. Shaping Emission Spectra of Fluorescent Molecules with Single Plasmonic Nanoresonators. *Physical Review Letters*, 100(20):203002, May 2008.

[27] G. Vecchi, V. Giannini, and J. Gómez Rivas. Shaping the Fluorescent Emission by Lattice Resonances in Plasmonic Crystals of Nanoantennas. *Physical Review Letters*, 102(14):146807, April 2009.

[28] Marcus Schmelzeisen, Yi Zhao, Markus Klapper, Klaus Müllen, and Maximilian Kreiter. Fluorescence Enhancement from Individual Plasmonic Gap Resonances. *ACS Nano*, 4(6):3309–3317, June 2010.

[29] Oluwafemi S. Ojambati, Rohit Chikkaraddy, William M. Deacon, Junyang Huang, Demelza Wright, and Jeremy J. Baumberg. Efficient Generation of Two-Photon Excited Phosphorescence from Molecules in Plasmonic Nanocavities. *Nano Letters*, 20(6):4653–4658, June 2020.

[30] Martin Kauert, Patrick C. Stoller, Martin Frenz, and Jaro Rička. Absolute measurement of molecular two-photon absorption cross-sections using a fluorescence saturation technique. *Optics Express*, 14(18):8434–8447, September 2006.

[31] Mark W. Dowley, Kenneth B. Eisenthal, and Warner L. Peticolas. Two-Photon Laser Excitation of Polycyclic Aromatic Molecules. *The Journal of Chemical Physics*, 47(5):1609–1619, September 1967.

[32] Mariacristina Rumi and Joseph W. Perry. Two-photon absorption: An overview of measurements and principles. *Advances in Optics and Photonics*, 2(4):451–518, December 2010.

[33] M. T. Homer Reid and S. G. Johnson. Efficient Computation of Power, Force, and Torque in BEM Scattering Calculations. *ArXiv e-prints*, July 2013.

[34] `http://github.com/homerreid/scuff-EM`.

[35] Taishi Zhang, Nengyue Gao, Shuang Li, Matthew J. Lang, and Qing-Hua Xu. Single-Particle Spectroscopic Study on Fluorescence Enhancement by Plasmon Coupled Gold Nanorod Dimers Assembled on DNA Origami. *The Journal of Physical Chemistry Letters*, 6(11):2043–2049, June 2015.

[36] András Szenes, Balázs Bánhelyi, Tibor Csendes, Gábor Szabó, and Mária Csete. Enhancing Diamond Fluorescence via Optimized Nanorod Dimer Configurations. *Plasmonics*, 13(6):1977–1985, December 2018.

[37] Manshu Peng, Feifei Sun, Na Na, and Jin Ouyang. Target-Triggered Assembly of Nanogap Antennas to Enhance the Fluorescence of Single Molecules and Their Application in MicroRNA Detection. *Small*, 16(19):2000460, 2020.

[38] Zhi Zhao, Xiahui Chen, Jiawei Zuo, Ali Basiri, Shinhyuk Choi, Yu Yao, Yan Liu, and Chao Wang. Deterministic assembly of single emitters in sub-5 nanometer optical cavity formed by gold nanorod dimers on three-dimensional DNA origami. *Nano Research*, August 2021.

[39] John W. Daily. Saturation effects in laser induced fluorescence spectroscopy. *Applied Optics*, 16(3):568–571, March 1977.

[40] Keith Berland and Guoqing Shen. Excitation saturation in two-photon fluorescence correlation spectroscopy. *Applied Optics*, 42(27):5566–5576, September 2003.

3

Quantum yield limits for the detection of single-molecule fluorescence enhanced by a gold nanorod

Fluorescence-based single-molecule optical detection techniques are widely chosen over other methods owing to the ease of background screening and better signal-to-noise throughput. Nonetheless, the methodology still suffers from limitations imposed by weak emitting properties of most molecules. Plasmonic nanostructures, such as gold nanorods, can significantly enhance the fluorescence signal of a weak emitter, extending the application of these techniques to a wider range of species. In this work, we explore the lower limit of fluorescence quantum yield for single-molecule detection, using a single gold nanorod to enhance molecular fluorescence. We specifically designed an infrared dye with the extremely low quantum yield of 10^{-4} *and a comparatively large Stokes shift of* $3,000\ \mathrm{cm}^{-1}$ *to demonstrate single-molecule detection by fluorescence enhancement. This example allows us to discuss more general cases. We estimate theoretically the optimal excitation wavelength and the plasmon resonance of the rod which maximize the fluorescence signals. We then confirm experimentally the detection of single-molecule fluorescence with an enhancement factor of* 3 *orders of magnitude for the quantum yield* 10^{-4}*. Theoretical simulations indicate that single-molecule signals should be detectable for molecules with quantum yield as low as* 10^{-6}*, provided the dwell time of the molecules in the plasmonic hot spot is long enough.*

3.1. Introduction

Optical detection of single molecules lies at the core of numerous biochemical studies as it opens up the possibility of investigating individual molecular behaviour usually hidden in the ensemble measurements[1–5]. The key to successful single-molecule detection is to optimize and extract a weak signal from a high background[6–9]. Over the past decades, fluorescence-based single-molecule techniques have been widely applied due to the easy but efficient background suppression and their high sensitivity[9–14]. In this method, the photons emitted at longer wavelength than the excitation light (Stokes-shifted), can easily be discriminated from the background by spectral filtering, providing exceptional contrast and thereby enabling the detection and study of weak single-molecule signals [14, 15]. Notwithstanding the many successes of fluorescence-based single-molecule techniques, it would be important to extend them to a broader range of absorbing molecules with weak emission, especially those emitting in the near-infrared. Chen et.al.[16] have designed deep-red low quantum yield dyes (quantum yield≈0.002) with large Stokes shift that prove to be better in staining mitochondria than normal MitoTrackers. In another work, water-soluble low quantum yield rylene derivative dyes (quantum yield≈0.01) were studied for the application of membrane labelling[17]. They prove to be more photostable than other well-established dyes. While dealing with low-quantum-yield dyes, conventional spectrofluorimeters can not be effectively used to study single-molecule fluorescence mainly because impurities become dominant. The decrease in quantum efficiency for red and NIR dyes is usually attributed to the energy gap law[18]. Recently, the low quantum yield of red fluorescent proteins has been attributed to the presence of dark chromophores[19], which limit their sensing applications [20, 21]. One way to improve these weak emitters is to minimise their nonradiative decay. Another promising strategy to improve the fluorescence efficiency of single-molecule fluorescence is to enhance the radiative emission rate by coupling the fluorophores to plasmonic structures, which can enhance the local field by confining the electromagnetic energy to volumes well below the diffraction limit[2, 13, 22–26].

Compared to strong emitters, poor emitters with low quantum yields benefit from a stronger fluorescence enhancement by plasmonic structures. They are easier to detect at the single-molecule level because of reduced background from unenhanced molecules. This has led researchers in previous studies to employ quenching agents such as methyl viologen [27–29] and nickel chloride[30] to reduce the quantum yield of the emitter. The plasmonic structures in those experiments were fabricated by various top-down and bottom-up approaches. Fluorescence enhancement of emitters with quantum yield down to 1×10^{-3} has been experimentally demonstrated with nano-fabricated bow-tie antennas[31, 32]. More convenient alternative plasmonic structures are wet-chemically synthesized gold nanorods (GNRs), which have attracted significant interest for their facile synthesis and unique optical properties [25, 33–35]. The collective oscillations of the GNR's free electrons, known as localized surface plasmons, strongly confine the electromagnetic field into a sub-wavelength region near the tips, thereby enhancing the excitation rates of the molecules nearby[24]. The plasmonic resonance of GNRs can easily be tuned from the red to the near-infrared range by adjusting their aspect ratio, making them a good single-molecule detection platform for a wide range of fluorescent species[25]. In addition to the excitation enhancement, GNR can enhance radiative channels by increasing the local density of photon states. However, this

enhancement of spontaneous emission is generally accompanied by enhanced non-radiative decay channels. Going closer to the metal will generally increase the excitation and radiative enhancements, but at the same time it will also increase the non-radiative processes responsible for fluorescence quenching, leading to an optimal range for the total enhancement [36–38]. Overlapping the excitation wavelength and the plasmon resonance with the emission spectra of a particular emitter can enhance both the excitation and emission rates, thereby improving the fluorescence enhancement. By using this strategy, we have earlier reported the detection of gold-nanorod-enhanced single-molecule fluorescence from dyes with a quantum yield of 10^{-3}, with an enhancement factor of up to 1000[25]. In the present work, we explore the possibility to enhance the fluorescence of dyes with even lower quantum yield, while keeping the fluorescence observable against background, the strongest source of which is the intrinsic photoluminescence of gold, also enhanced by the plasmon resonance. When going to weaker quantum yields, it is not enough to consider the enhancement factor alone. Indeed, the quantity determining the detection limit is the signal-to-noise ratio, which depends in a complex manner on the plasmon enhancement, the molecular absorption cross section and the fluorescence quantum yield. Therefore, we undertook careful theoretical and experimental investigations of fluorescence enhancement for weak quantum yields in view of optimizing the enhanced fluorescence signal and of extending single-molecule techniques to a much broader range of emitting species.

In this study, we explore single-molecule detection of very weak emitters with quantum yields as low as 1×10^{-4}, by enhancing their fluorescence with a single gold nanorod. To optimize the signal, we need to consider the molecule's Stokes shift (about $150\ \mathrm{nm}$ or $3000\ \mathrm{cm}^{-1}$). Indeed, we have a trade-off between molecular excitation rate and the fluorescence enhancement. Using theoretical simulations, we optimize the excitation wavelength and the plasmon resonance of the rod. We then apply these parameters to detect single-molecule fluorescence experimentally with enhancement factors of three orders of magnitude. We further investigate the quantum yield dependence of the signal-to-noise ratio of the plasmon-emitter coupled system and estimate the lowest quantum yield for which single emitters can be detected in the near field of a single gold nanorod. Although we consider only single nanorods here because of their ease of synthesis, modeling, and manipulation, our results can easily be extended to more complicated nanostructures with much higher near-field enhancement, such as strongly coupled gold nanoparticle dimers or clusters.

3.2. Results and discussion

In this work, instead of selecting molecules with small Stokes shifts (i.e., separation between the maxima of absorption and emission) as done in previous studies[25], we focus on the case of low-quantum-yield dyes, which often have much larger Stokes shifts. For large Stokes shifts (i.e., for small overlaps between the absorption and emission spectra), enhancing both the excitation and the radiation processes with the same narrow-band GNR antenna is very difficult. As a consequence, detection of such single molecules becomes harder than those with small Stokes shifts. To get maximum signals, we will have to sacrifice a fraction of the enhancement factor. In a simple coupled system of a single gold nanorod and an emitter, we can optimize emission by balancing excitation and radiative enhancements, through adjustment of the excitation wavelength and of the aspect ratio of the gold nanorod.

For our study, we selected a molecule of the donor-acceptor type based on Naphthalene Diimide-terthiophene (NDI-2TEG-3T) because it is a very weak emitter. It has a measured quantum yield of about 1.3×10^{-4} and has a large Stokes shift between the emission and the absorption bands. The structure of the molecule is shown in the inset of Figure 3.2.c and the synthesis details are given in the Supporting Information. The low fluorescence efficiency of NDI-2TEG-3T is due to its typical donor-acceptor structure. The introduction of terthiophene units as donors provides an energy level which is suitable for the photoinduced electron transfer process. This extra channel for nonradiative exciton relaxation consequently quenches the fluorescence[39, 40]. When measured in toluene, the NDI-2TEG-3T molecule shows two distinct absorption bands. One of these two bands is assigned to a high-energy $\pi - \pi^*$ transition in the range of 300 to 400 nm. The second one is a low-energy broad intramolecular charge-transfer transition in the range of 500 to 700 nm with its maximum at 590 nm. It originates from the electron-rich terthiophene group to the electron-deficient NDI unit. We focus on the second band with the maximum at 590 nm as it overlaps better with typical gold nanorod resonances. The fluorescence band lies in the near-infrared range with its maximum at about 740 nm. Both bands can be overlapped with the plasmon resonance of gold nanorods, opening possibilities of very large fluorescence enhancements through the combination of excitation and emission enhancements. However, as mentioned before, we need to explore the dependence of the enhanced fluorescence signal on excitation wavelength and on plasmon resonance in order to optimize it.

We begin our discussion with the simulation of fluorescence enhancement of NDI-2TEG-3T by a single gold nanorod. For simplicity, we consider the molecule to lie on the long symmetry axis of the rod, at a variable distance from the tip (we call this distance the 'gap' as represented in the inset of Figure 3.1.b). Considering the small quantum yield and the short lifetime of NDI-2TEG-3T molecules, we apply the simplified two-level scheme model for the calculation of the fluorescence enhancement factor, which neglects the excitation saturation (see Supporting Information for more details). Moreover, we assume both the excitation wave polarization and the molecular dipole to be oriented along the same longitudinal nanorod axis. This simulation therefore applies to the configuration providing maximum enhancement. The plasmon wavelength of the nanorod was tuned by changing its length while keeping its diameter constant at 25 nm, which is the average rod diameter in our experiments. The dielectric permittivity of gold was taken from Johnson and Christy[41], and the refractive index of the medium was set to 1.496 for toluene.

Figure 3.1.b shows the dependence of the excitation and emission enhancements on the gap, with the excitation and plasmon wavelengths at 671 nm and 673 nm, respectively. The excitation enhancement increases monotonously as the gap decreases. The emission enhancement, however, presents a maximum, found here at the gap of about $d_{\mathrm{m}} = 1.5$ nm. The maximum emission enhancement reaches about 200, leading to a maximum total enhancement of five orders of magnitude. The value of d_{m} depends on the dye quantum yield. For quantum yields such as 1×10^{-2}, the optimal gap is about 4 nm (See Figure. S3.11.), whereas for very low quantum yields, the optimal gap shifts to values of 1.5 nm or less (1.5 nm for a yield of 1.3×10^{-4} in Figure 3.1b.). This is because, by reducing the gap, we can benefit from higher excitation and radiative enhancements, while quenching by the metal is still dominated by non-radiative relaxation within the molecule.

Next, we optimized the fluorescence intensity of the nanorod-molecule system, by vary-

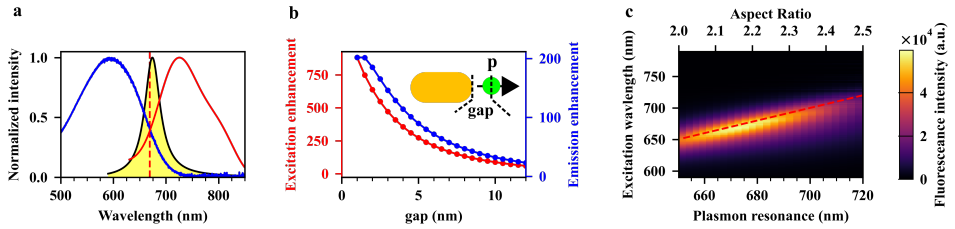

Figure 3.1: (a) Absorption (blue) and emission (red) spectra of NDI-2TEG-3T in toluene. The shaded band is the gold nanorod scattering spectrum calculated for the aspect ratio corresponding to the optimum normalized intensity (see (c)), at excitation wavelength 671 nm (vertical red dashed line). (b) Calculated excitation (red) and emission (blue) enhancements as functions of the gap, i.e., the separation of the molecule from the tip of the gold nanorod. [Inset: schematic of the simulated molecule-nanorod system.] (c) Estimated enhanced fluorescence intensity as a function of the excitation wavelength and of the plasmon resonance wavelength of the gold nanorod. The fluorescence intensity was normalized by the non-enhanced intensity of the fluorescence excited at 671 nm. The red dashed straight line corresponds to the molecule being excited at the wavelength of the plasmon resonance. All values are obtained by varying the gap and selecting the gap value providing maximum enhancement.

ing both the excitation wavelength and the aspect ratio of the gold nanorod. Figure 3.1.c gives the normalized fluorescence intensity as a function of the excitation wavelength and of the resonance wavelength of the gold nanorod. To obtain this plot, we have varied the gap value to optimize the intensity, for each excitation and plasmon wavelength. The plot is given for a fixed quantum yield of 1.3×10^{-4}, corresponding to NDI-2TEG-3T in toluene. As can be seen on Figure 3.1.c, the maximum fluorescence intensity enhanced by each rod is obtained for excitation nearly in resonance with the plasmon, i.e., ($\omega_{\mathrm{exc}} \sim \omega_{\mathrm{sp}}$), because most of the enhancement arises from the excitation. Here ω_{exc} is the frequency of the excitation light source and ω_{sp} is the frequency of the surface plasmon resonance. Next, we note an intensity maximum (sweet spot) at the plasmon wavelength of about 674 nm, which balances the enhancement of both excitation and radiative processes. The total fluorescence enhancement value at this spot is 50,000 times. Here, we can see in Figure 3.1.a that the plasmon resonance at the sweet spot (yellow shaded band) does not overlap exactly with the emission maximum of the molecule, as had been postulated in previous studies to give maximum total fluorescence enhancement (see Supporting Information.), but corresponds to the maximum overlap with both the dye absorption (blue line) and emission (red line) spectrum.

We can interpret the results of simulations in Figure 3.1.c in a very simple way. We notice that the total intensity in Eq (S3.10) is a product of the molecular absorption cross setion C_{abs}, the excitation enhancement factor, and the emission enhancement which is nearly equal to the radiative enhancement factor in the limit of very weak quantum yields. As the excitation and radiation processes are both enhanced by the same narrow plasmon resonance (Lorentzian form), we can approximate the enhanced intensity as:

$$I(\omega_{\mathrm{exc}}) \propto C_{\mathrm{abs}}(\omega_{\mathrm{exc}}) \cdot F_{\mathrm{dye}}(\omega_{\mathrm{exc}}) \cdot f(\omega_{\mathrm{exc}}), \tag{3.1}$$

which means we tune the plasmon resonance and the excitation wavelength to the maximum overlap between absorption and emission of the molecule (see extensive mathematical justification in the Supporting Information).

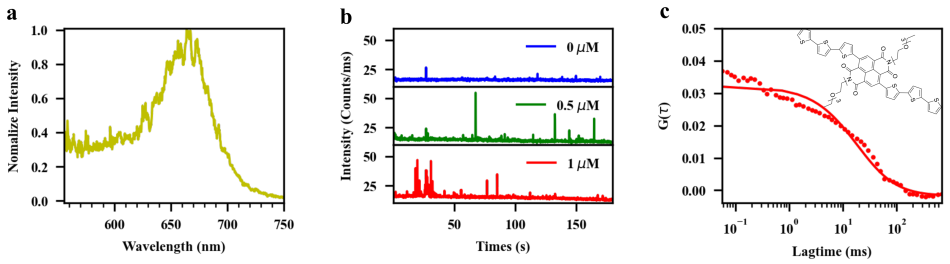

Figure 3.2: (a), Photoluminescence spectra of the gold nanorod deposited on a glass surface and immersed in toluene, which was used to enhance the fluorescence of NDI-2TEG-3T, (b), Photoluminescence time trace from the single gold nanorod immersed in a solution of NDI-2TEG-3T in toluene with different concentrations. (c), The measured (red dashed line) autocorrelation curve of the fluorescence bursts shown in (b) for molecular concentration of 1 μM, and the single exponential fitting of the curve (red solid line). Inset: chemical structure of NDI-2TEG-3T.

We performed fluorescence enhancement experiments on NDI-2TEG-3T molecules under the theoretically derived optimum conditions. Gold nanorods, with average plasmon wavelength of 614 nm, were immobilized on the surface of clean coverslips and immersed in toluene containing different concentrations of NDI-2TEG-3T. The plasmon wavelength of the gold nanorod red-shifts to about 680 nm in toluene due to its high refractive index of 1.496. The measurements were performed on a home-built confocal microscope setup. A circularly polarized continuous-wave (CW) laser with the wavelength of 671 nm was chosen as the excitation source, and was focused by an oil immersion objective with a numerical aperture (NA) of 1.4 to a diffraction-limited spot (about half-a-μm in diameter). A long-pass filter ($\geq$ 675 nm LongPass U-Grade 671/RazorEdge, Semrock) was used to separate the fluorescence signal from the background of scattered laser light. Before adding the NDI-2TEG-3T solution, we recorded photoluminescence (PL) spectra of each bright spot to make sure that the nanoparticle under study had the single Lorentzian lineshape of a single gold nanorod. Time traces were taken for each nanorod under different concentrations of the molecules while keeping the excitation power constant. In each step, the concentration of the molecules was adjusted by adding a certain amount of high concentrated NDI-2TEG-3T solution (50 μM) sequentially, followed by some 10 minutes for diffusion to homogenize the concentration. As confirmed by bulk measurements of the concentration-dependent absorbance, NDI-2TEG-3T is very well dissolved in toluene in our experimental range of molecular concentration (see Figure S3.5). The absence of spectral signatures from dimers and higher clusters confirms that the molecules are well separated from each other, and hence access the plasmonic hot spot independently of each other.

Figure 3.2 shows typical experimental measurements of single-molecule fluorescence enhanced by a single gold nanorod. We first identify single nanorods among spots in the optical image from their photoluminescence spectrum which has a Lorentzian shape and is relatively narrow. Figure 3.2.a indicates a single nanorod with its plasmon resonance at 667 nm. In the intensity time traces as shown in Figure 3.2.b, the background arises from gold nanorod photoluminescence and from the very weak non-enhanced fluorescence of all the molecules in the volume of the excitation focal spot, while the bursts are due to the en-

hanced fluorescence of the molecules within the hot spots near the tips of the rod. To verify that the bursts indeed arise from single molecules, we compared the time traces taken at different NDI-2TEG-3T concentrations. As shown in Figure 3.2.b, in pure toluene solvent, we do not see any strong bursts in the fluorescence time-trace. Bursts appear more and more frequently in the time traces as we increase the NDI-2TEG-3T concentration, while the background remains at a similar level. This observation confirms that the signal from all the non-enhanced molecules in the focal spot (about 52 molecules) is negligible compared to the photoluminescence of the rod, even though the molecular concentration is as high as $1.0\ \mu\mathrm{M}$, because the quantum yield of NDI-2TEG-3T is exceedingly weak. The bursts arise from molecules diffusing through, or being transiently stuck in the tiny hot spots near the tips of the nanorods. The probability of such bursts increases as the molecular concentration increases. By analyzing the highest bursts in the fluorescence time trace, we see the typical single-step single molecule bursts with the time duration in the order of $10\ \mathrm{ms}$ (Figure S3.9), which confirms that only a single molecule was present in the hotspot during the burst, and indicated that it was transiently immobilized. The autocorrelation curve for the fluorescence bursts corresponding to molar concentration of $1\ \mu\mathrm{M}$ is shown in Figure 3.2.c. By fitting the autocorrelation curve to a single exponential, we obtained an average correlation time of $27\ \mathrm{ms}$, which is obviously too long to be due to the free diffusion of molecules through the near field of a nanorod according to the previous works[24–26], where passivation of the glass surface completely suppressed the long-lived bursts. The correlation time results from an interplay between sticking time and bleaching time in the experimental conditions. Here, it can most likely be considered as the result of the transient sticking of dye molecules. Noting that sticking to the metal surface would lead to complete quenching of the fluorescence[42–44], we assign the long bursts to sticking onto the glass substrate. The intensities of the bursts in the time traces depend on the orientation and spatial position of the molecules with respect to the gold nanorods during their residence within the hot spot. As an approximation, we represented the maximum enhanced fluorescence as the largest intensity of the bursts in the time trace, subtracting the background[45]. Those maximum bursts are around $55\ \mathrm{counts/ms}$, whereas the background is $16\ \mathrm{counts/ms}$. To get the enhancement factor, we evaluated the fluorescence signal of one NDI-2TEG-3T molecule from a high-concentration solution ($50\ \mu\mathrm{M}$), by recording the fluorescence signal under the same experimental conditions but on an area without a nanorod. Figure S3.7 (of the Supporting Information) shows such a trace with an average count of 36 per 1 ms bin time, when the excitation power is 3.3 times larger than the power we used for single molecules measurements. We estimate the number of molecules in the focal volume (about $0.061\ \mathrm{fL}$), at the given concentration of $50\ \mu\mathrm{M}$, to be about $1,800$ at any given time. From this, we get an estimate of the average intensity of about $6 \pm 1\ \mathrm{counts/s}$ per molecule. This corresponds to an enhancement factor of about $13,000$, taking the circularly polarized excitation into account. Note that the enhanced signal being stochastic, we estimate it by the largest observed signal, which entails an error of roughly a factor 2. The obtained enhancement value is significantly lower than the best enhancement factor expected for this low quantum yield (more than $100,000$, see Fig 3.3a. hereafter). Various factors can explain the difference: i) the plasmon resonance was not perfectly tuned to the laser and dye wavelengths; ii) the orientation of the molecule was probably not optimal as chosen in the calculation; and, most importantly, iii) the position of the dye was probably on the glass slide and not along the

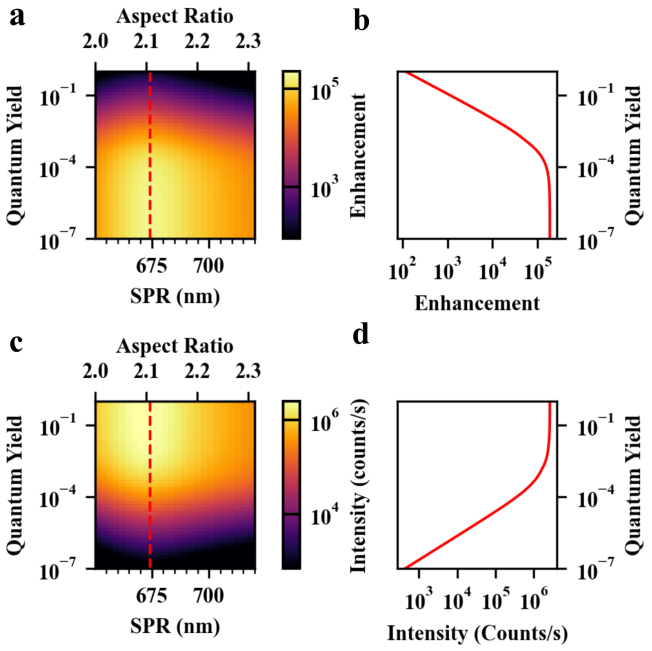

Figure 3.3: (a, c) Simulated fluorescence enhancement (a) and the estimated photon counts (c) from emitters with different quantum yields as functions of the plasmon resonance of the gold nanorod. The excitation wavelength was set as 671 nm. (b, d) Corresponding enhancement factor and emitted intensity enhanced by gold nanorod with the optimized plasmon wavelength of 673 nm (dashed red lines in a and c) as functions of the quantum yield of the molecule. In this plot, we kept the molecular absorption cross section and the excitation intensity constant, i.e., equal to the intensity used in the NDI-2TEG-3T measurements.

rod axis, which is the best position for enhancement. The latter factor can lead to significant reduction of the enhancement factor[46].

To illustrate how the enhancement factor can been tuned by the plasmon resonance of gold nanorods, we examined the fluorescence time traces recorded on gold nanorods with different plasmon wavelengths (see figure. S3.10.). From figure. S3.10. we can see that, as the SPR of the gold nanorods is detuned from the laser (blue shift from 667 nm to 638 nm), the strongest fluorescence bursts in the time traces also decreasing, with the enhancement factors decreasing from about $13,000$ to about $4,000$, respectively.

According to the aforementioned studies, we learn that by properly choosing the wavelengths of the excitation light and the plasmon resonance, we are able to detect single-molecule fluorescence enhanced by a single gold nanorod with high signal-to-background ratio, even though the molecular quantum yield is as low as 1.3×10^{-4}. To gain further insight into the possibility of fluorescence enhancement of single molecules with a simple individual gold nanorod, we performed numerical simulations of the detection limit for molecules with very low quantum yields, keeping the same molecular absorption cross section as NDI-2TEG-3T. In this study, we must consider which background sources will compete with enhanced fluorescence and prevent the detection of single events. Neglecting ex-

perimental imperfections, two sources of background as intrinsic to the sample under study: i) Fluorescence of molecules out of the hot spot. Although the concentration of molecules can exceed a micromolar, their fluorescence is negligible (less than 300 cps) because of the dye's low quantum yield. ii) Photoluminescence of the gold nanorod itself. Although intrinsic gold photoluminescence is very weak (10^{-10})[47], the photoluminescence signal is also enhanced by the plasmon resonance and cannot be separated from the enhanced fluorescence. A typical PL rate for the NRs in this study was $10\ \mathrm{kcps}$. We therefore base our discussion of the signal-to-background ratio on this value.

Figure 3.3 gives the simulated single-molecule fluorescence enhancement by a single gold nanorod as a function of molecular quantum yield. For the sake of comparison, we used the same excitation wavelength $671\ \mathrm{nm}$, the same absorption cross section, and the same fluorescence spectrum as those of NDI-2TEG-3T we used in our measurements. Therefore, the enhanced radiative and metal-induced non-radiative rates are independent of the quantum yields, and they share the same spectral dependence on the plasmon resonance. Because the spectral dependence of the plasmon-dependent emission enhancement is not changed, the spectral position of the plasmon resonance with maximum enhancement is conserved, independently of the quantum yield (see Eq. (S3.9)). As shown in Figure 3.3.a,c, the spectral position of the maximum enhancement factor and of the maximum enhanced fluorescence intensity do not change for different quantum yields. All are located at $674\ \mathrm{nm}$ (dashed red line in Figure 3.3.a,c). At the optimal plasmon wavelength of $674\ \mathrm{nm}$, the total enhancement factor increases dramatically at first, as the quantum yield of the emitter decreases (see Figure. 3.3.d), until it approaches the constant value of 2×10^5, which confirms the simple expression in Eq. (S3.9) for the emission enhancement limit. To understand this result, we approximate the product of excitation and radiative enhancements $\xi_{\mathrm{exc}} \cdot \xi_{\mathrm{rad}}$ (i.e., the total fluorescence enhancement factor expected for vanishing quantum yield) as the fourth power of the field enhancement factor: $\xi_{\mathrm{total}} \xrightarrow{\eta_0 \to 0} \xi_{\mathrm{exc}} \cdot \xi_{\mathrm{rad}} \propto |\mathbf{E}/\mathbf{E}_0|^2 \cdot |\mathbf{E}/\mathbf{E}_0|^2 \sim |\mathbf{E}/\mathbf{E}_0|^4$, the value of which is $(27)^4 \sim 5 \times 10^5$. The enhanced fluorescence intensity, however, drops with the quantum yield as can be seen by substituting Eq.(S3.9) into Eq.(S3.10). The enhanced intensity (see Figure 3.3.d) at first is approximately constant down to a quantum yield of about 10^{-3}, as the decrease in molecular quantum yield is roughly compensated by an associated increase in enhancement. However, when the molecular quantum yield becomes lower than 10^{-3}, the enhancement factor saturates, causing the intensity to drop with the molecular quantum yield. As shown in Figure 3.3.d, the estimated photon intensity from a single emitter drops from $2 \times 10^6\ \mathrm{counts/s}$ to $4 \times 10^3\ \mathrm{counts/s}$ when its quantum yield η_0 decreases from 100% to 10^{-6}. Such a signal would still be detectable above the photoluminescence background of the nanorod, even for an integration time as short as $10\ \mathrm{ms}$. From the above discussion, we find that by enhancing the fluorescence with a single gold nanorod, one can expect photon intensities of thousands of counts/s from a single molecule even though its quantum yield is as low as 10^{-6}, a single-molecule fluorescence comparable with the background from the luminescence of a single gold nanorod ($\sim 10^4\ \mathrm{counts/s}$), under typical excitation laser power in the experiments. However, sufficiently long integration times are needed (about 10 ms), which requires a high medium viscosity, or transient sticking of the molecules. In principle, this contrast allows us to detect the signal from a single molecule. By looking at the signal-to-noise ratio in Figure 3.4, we can see that $SNR \sim 10$ for molecules with the quantum yield of 10^{-6} (green dashed), and even though

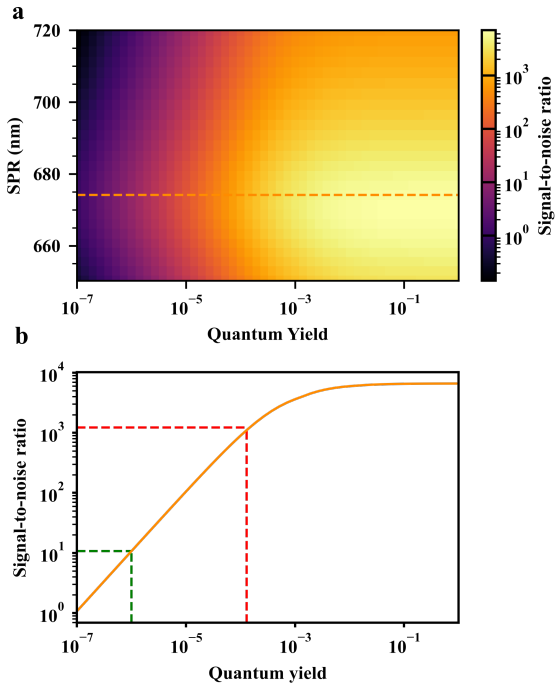

Figure 3.4: (a) Signal-to-noise ratio of the coupled nanorod-molecule system with different plamsonic resonance as functions of the molecular quantum yields. (b) Corresponding signal-to-noise ratio with the the excitation wavelength at 671 nm and the plasmon resonance of the gold nanorod optimizing for the properties of NDI-2TEG-3T (dashed orange line in (a)). We assumed a typical experimental background of nanorod photoluminescence (10^4 cps) at the plasmonic wavelengh of 673 nm, and the photoluminescence of other plasmonic wavelengths were normalized by their scattering cross sections. Integration time was set as 0.1 s. The green dashed line corresponds to molecule of quantum yield 10^{-6} and the red dashed line corresponds to the quantum yield of NDI-2TEG-3T molecule (1.3×10^{-4}).

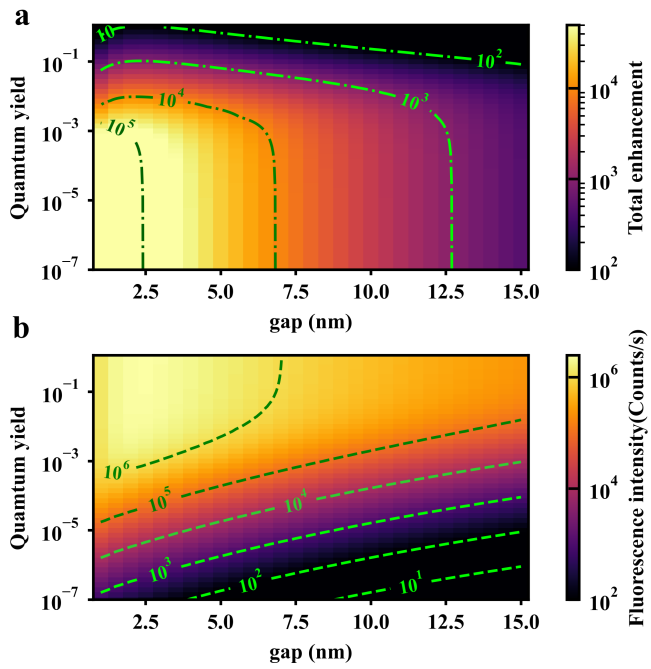

Figure 3.5: Color plots of the calculated fluorescence enhancement (a) and of the estimated photon intensity (b) as functions of the separation of the rod tip to emitter distance (gap) and of the emitter's quantum yield. The green dashed lines in each figure are contours of equal enhancements and intensities. All molecular parameters except the yield were kept constant, as above.

it is one hundred times smaller than that of the measured NDI-2TEG-3T molecules with the quantum yield of 1.3×10^{-4} (red dashed), it still provides enough contrast to distinguish single-molecule signals from background noise.

Following the above discussion, one should keep in mind that as the quantum yield decreases, the volume for the single-molecule fluorescence to be effectively enhanced will also decrease. This can be understood intuitively. As we reduce the quantum yield of the molecule, internal conversion will outcompete quenching by the metal at shorter and shorter distance, so that the molecules can get closer to the gold nanorod and reach larger fluorescence enhancement. This increase of the enhancement can mitigate, to some extent, the strong fluorescence reduction due to the decreasing quantum yield. This partial compensation is seen clearly on the green dashed lines in Figure 3.5, which scales more favorably than quantum yield for small gaps. Therefore, the molecules with smaller quantum yield can get closer to the tips of the nanorod to emit more photons. As a consequence, because diffusion time scales as the squared distance, successful detection of single molecules with very small quantum yield requires slower diffusion or longer binding events than molecule with high quantum yields. Moreover, the reduced effective near-field volume leads to a lower number of detected events, which can be compensated by increasing the concentration of the molecules. We made use of this compensation in our experiment, as we used molecu-

lar concentrations in the μM range instead of nM, as was done in the previous work with quantum yield of 10^{-2}. Additionally, we could also make sure to keep the molecules for longer times in the vicinity of the nanorod tips. This can be done either by slowing down the molecular diffusion in a more viscous solvent, or by transient binding of the molecules within the effective near-field volume, for example through DNA-transient binding[48].

In conclusion, we have provided a detailed study of single-molecule fluorescence enhancement by wet-chemically synthesized single gold nanorods, for extremely weak emitters. The molecule we studied, NDI-2TEG-3T, was specifically designed to emit in the near-infrared range, but with a very low quantum yield of 1×10^{-4}, and a large Stokes shift of 150 nm. Our work provides a suitable demonstration of single-molecule fluorescence enhancement by a single gold nanorod. Our numerical simulations show that, in order to optimize count rates from molecules with low quantum yield and large Stokes shift, we need to optimize the excitation wavelength and the plasmon resonance of the gold nanorod. Based on our theoretical study, we successfully detected single-molecule fluorescence bursts with enhancement factors of up to 10^4 with a simple gold nanorod. The squeezing of the effective near-field volume for enhancement of low-quantum-yield dyes allows us to detect single-molecule signals from solutions of high molecular concentrations, in the range of μM, with high contrast. Theoretical analysis further shows that even for quantum yields as low as 10^{-6}, we will still be able to detect single molecules by fluorescence enhancement by a single gold nanorod, provided the residence time in the effective near-field is longer than tens of ms. The experimental method and the theoretical model presented in this work can be readily extended to other plasmonic nanostructures, which may promote single-molecule techniques based on fluorescence enhancement to a wider range of applications.

S3.1. Supporting information

S3.1.1. Experimental Details

Synthesis and Characterization
Reagents
All reagents and solvents were commercial and were used as received. [2,2':5',2"-terthiophen]-5-yltributylstannane and 2-(2-(2-ethoxyethoxy)ethoxy)ethanamine were synthesized according to literature procedures[49, 50]
Characterization
^{1}HNMR and ^{13}CNMR were performed on a Varian Unity Plus (400 MHz) instrument at 25 ^{o}C, using tetramethylsilane (TMS) as an internal standard. NMR shifts are reported in ppm, relative to the residual protonated solvent signals of $CDCl_3$ (δ= 7.26 ppm) or at the carbon absorption in $CDCl_3$ (δ = 77.23 ppm). Multiplicities are denoted as: singlet (s), doublet (d), triplet (t) and multiplet (m). High Resolution Mass Spectroscopy (HRMS) was performed on a JEOL JMS 600 spectrometer. FT-IR spectra were recorded on a Nicolet Nexus FT-IR fitted with a Thermo Scientific Smart iTR sampler.

Synthesis of NDI-2TEG-3T

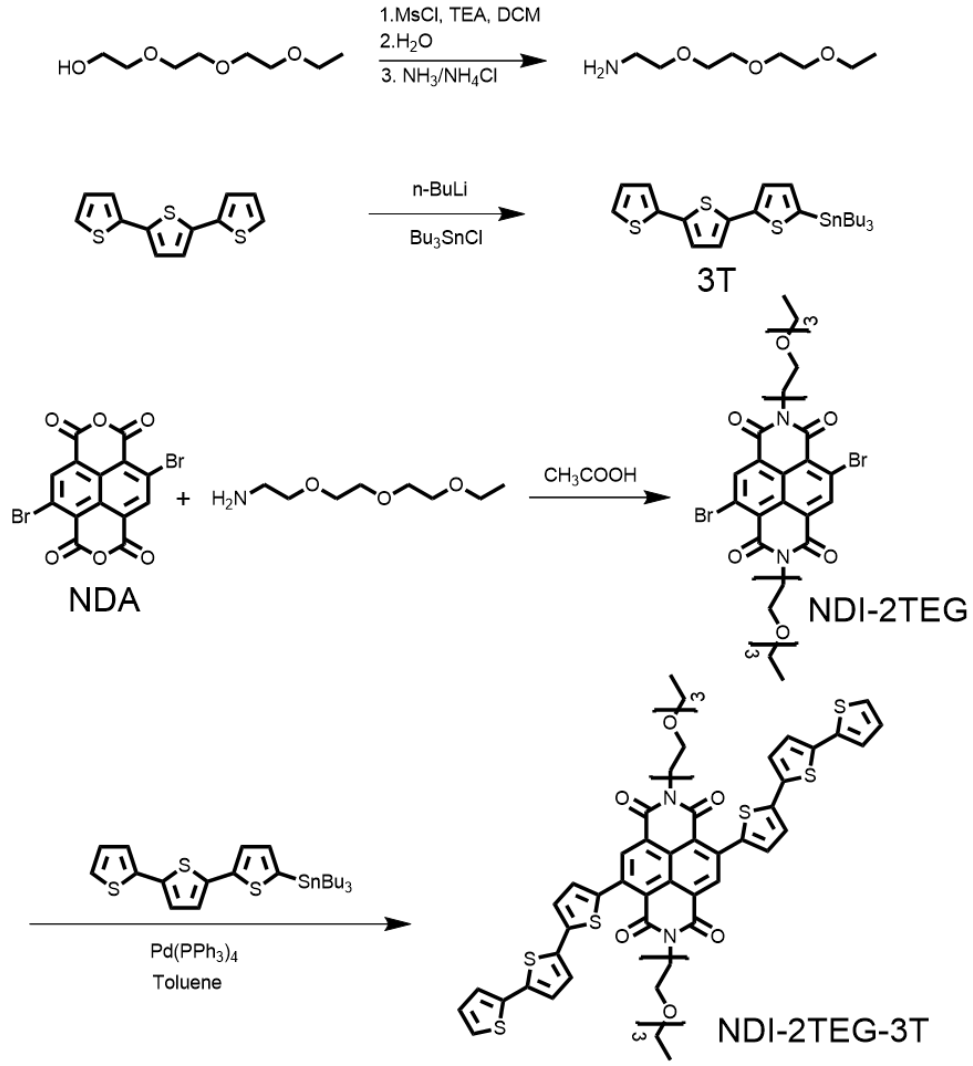

Figure S3.1: Synthetic route for NDI-2TEG-3T

4,9-dibromo-2,7-bis(2-(2-(2-ethoxyethoxy)ethoxy)ethyl)benzo[lmn][3,8]phenanthroline-1,3,6,8(2H,7H)-tetraone (**NDI-2TEG**) was synthesized according to literature procedures[51].

Synthesis of NDI-2TEG-3T

To a dry three-neck flask, NDI based monomer (**NDI-2TEG**) (20 mg, 0.027 mmol) and thiophene based monomer (**3T**) (60 mg, 0.1 mmol) were added under N_2 followed by catalyst Tetra(triphenylphosphine) palladium [$Pd(PPh_3)_4$] (8 mg). The flask and its contents were subjected to 3 pump/purge cycles with N_2 followed by addition of anhydrous, degassed

Toluene (5 mL) via syringe. The reaction mixture was stirred at 120 °C for overnight. After cooling to room temperature, the deeply colored reaction mixture was poured into 100 mL water, then extracted with CH_2Cl_2. The organic phase was washed with brine, dried over anhydrous sodium sulfate and removed solvent by rotary evaporator. The crude product was purified by silica gel column chromatography with CH_2Cl_2/acetone (20:1) as the eluent afforded 10 mg (34 % yield) target compound as solid.
^{1}HNMR (400 MHz, $CDCl_3$) δ: 8.78 (s, 2H), 7.30 (d, J = 3.7 Hz, 2H), 7.24 − 7.23 (m, 4H), 7.23 − 7.19 (m, 2H), 7.17 (d, J = 3.7 Hz, 2H), 7.12 (d, J = 3.7 Hz, 2H), 7.06 − 7.01 (m, 2H), 4.42 (t, J = 3.6 Hz, 4H), 3.91 − 3.77 (m, 4H), 3.77 − 3.65 (m, 4H), 3.65 − 3.56 (m, 8H), 3.54 − 3.42 (m, 8H), 1.15 (t, J = 3.6 Hz, 6H).
^{13}CNMR (100 MHz, $CDCl_3$) δ: 164.86, 164.84, 143.03, 142.07, 141.83, 139.80, 139.59, 139.18, 138.07, 132.90, 130.60, 130.27, 128.07, 127.76, 127.42, 127.11, 126.60, 126.54, 125.35, 73.34, 73.29, 72.79, 72.44, 70.54, 69.27, 42.42, 17.81.
HRMS(ESI) Calcd. for $C_{54}H_{51}N_2O_{10}S_6$ $[M+H]^+$: 1079.18625, found: 1079.18744; Calcd. for $C_{54}H_{54}N_3O_{10}S_6$ $[M+NH_4]^+$: 1096.21280, found: 1096.21404; Calcd. for $C_{54}H_{50}N_2O_{10}S_6Na_1$ $[M+Na]^+$: 1101.16819, found: 1101.16896.

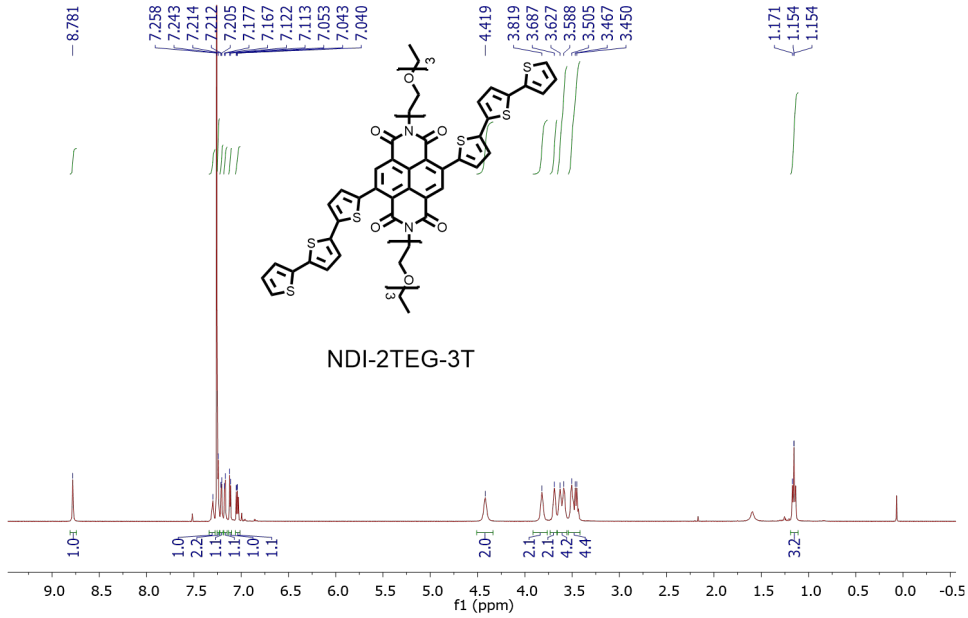

Figure S3.2: ^{1}HNMR spectrum of NDI-2TEG-3T.

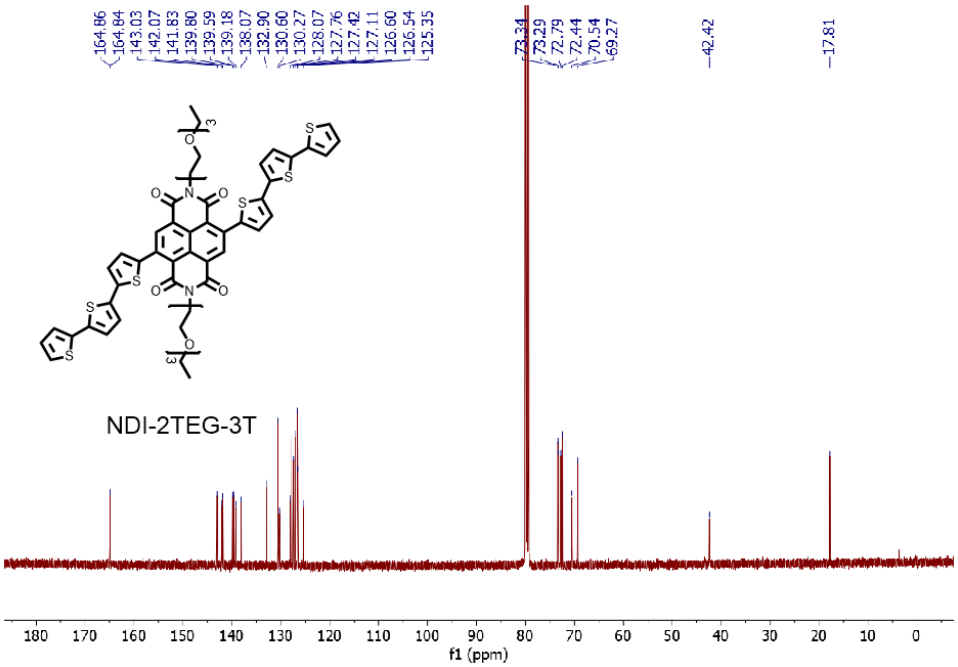

Figure S3.3: ^{13}CNMR spectrum of NDI-2TEG-3T.

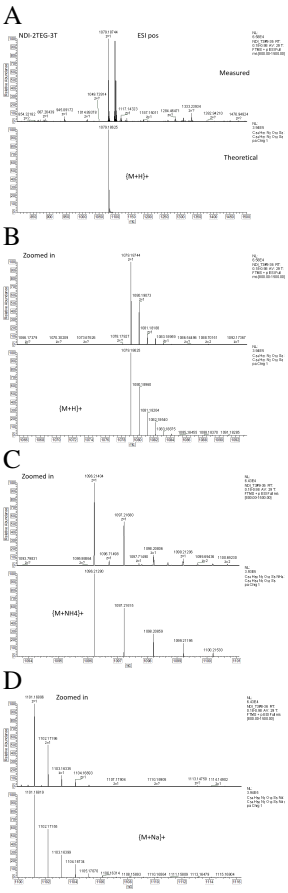

Figure S3.4: HRMS spectrum of NDI-2TEG-3T.

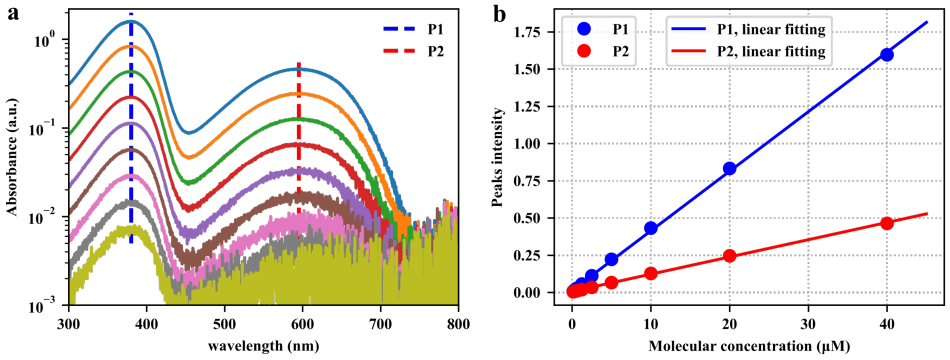

Figure S3.5: Absorption spectrum of NDI-2TEG-3T as a function of molecular concentration. The concentration of NDI-2TEG-3T was reduced by half at each step from top ($40\ \mu M$) to the bottom. Blue and red dashed lines represent the absorption peaks of the high-energy $\pi - \pi^*$ transition (P1) band and the low-energy intramolecular charge-transfer band (P2), respectively. (b) The two measured (dot) absorption peak intensities (P1 blue, P2 red) and their corresponding linear fits (solid lines) as functions of molecular concentration.

Fluorescence of NDI-2TEG-3T in Bulk

Quantum yield measurements of NDI-2TEG-3T

We estimated the quantum yield of NDI-2TEG-3T molecules by comparing their absorption and emission properties with commercial Alexa Fluor 647 dye, which has the quantum yield of 33%. Figure S3.6 gives the absorption and emission spectra of NDI-2TEG-3T (a) and Alexa Fluor 647 (b) in bulk solutions, respectively. The absorption spectra were recorded using a Cary 50 UV-Vis spectrometer (Varian Inc. Agilent Technology, USA), and the emission spectra were measured on a Cary Eclipse fluorescence spectrometer (Varian Inc. Agilent Technology, USA). The spectra for both NDI-2TEG-T3 and Alexa Fluor 647 were taken in the same experimental conditions, except that the solvent and molecular concentration were different. For Alexa Fluor 647, the molecular concentration was 290 nM in water, while for NDI-2TEG-T3, the molecules were dissolved in toluene with the concentration of 50 μM. In the plots, the spectra were normalized by the molecular concentration. As an approximation, we estimated the quantum yield of the NDI-2TEG-3T as,

$$Q_{\mathrm{NDI}} = Q_{\mathrm{Alexa647}} \cdot \frac{C_{\mathrm{Alexa647}}(\omega_{\mathrm{exc}}) < f_{\mathrm{NDI}} >}{C_{\mathrm{NDI}}(\omega_{\mathrm{exc}}) < f_{\mathrm{Alexa647}} >} \cdot \frac{n^2_{\mathrm{toluene}}}{n^2_{\mathrm{water}}}, \tag{S3.1}$$

from which we got the quantum yield of NDI-2TEG-3T, $Q_{\mathrm{NDI}} \approx 1.3 \times 10^{-4}$. Here, the subscripts "Alexa647" and "NDI" represent the Alexa Fluor 647 dye and NDI-2TEG-3T, respectively. C denotes the molecular absorption cross section. f_{NDI} and $f_{Alexa647}$ are the corresponding measured emission spectra, and $< \cdots >$ represents the averaging over the frequency. n_{toluene} and n_{water} are the refractive indices of toluene and water, respectively.

Average fluorescence intensity of an individual NDI-2TEG-3T molecule

To get the fluorescence enhancement factor, we measured the average brightness of NDI-2TEG-3T molecules in the focal volume without gold nanorods. The experimental conditions were the same as in the single-molecule enhancement measurement, except that the ex-

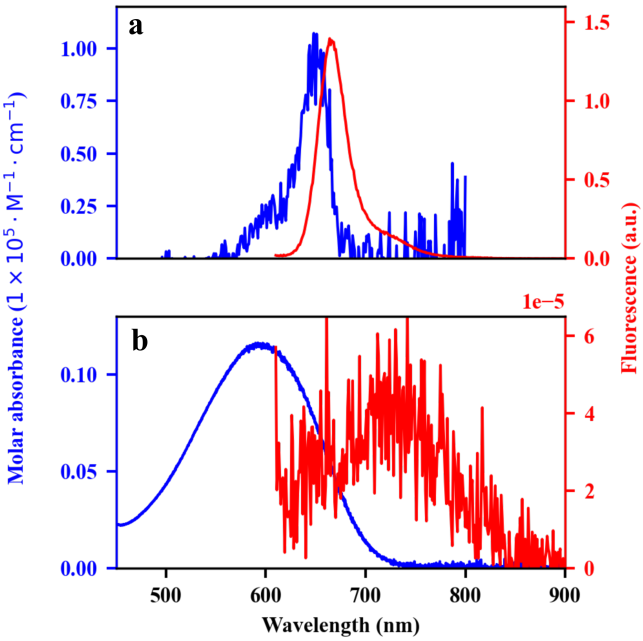

Figure S3.6: Fluorescence characterization of NDI-2TEG-3T. (a) Molecular absorption (blue) and emission (red) spectra of the commercial standard dye Alexa Fluor 647. (b) Molecular absorption (blue) and emission (red) spectra of NDI-2TEG-3T. The emission intensities were normalized with the corresponding molecular concentrations.

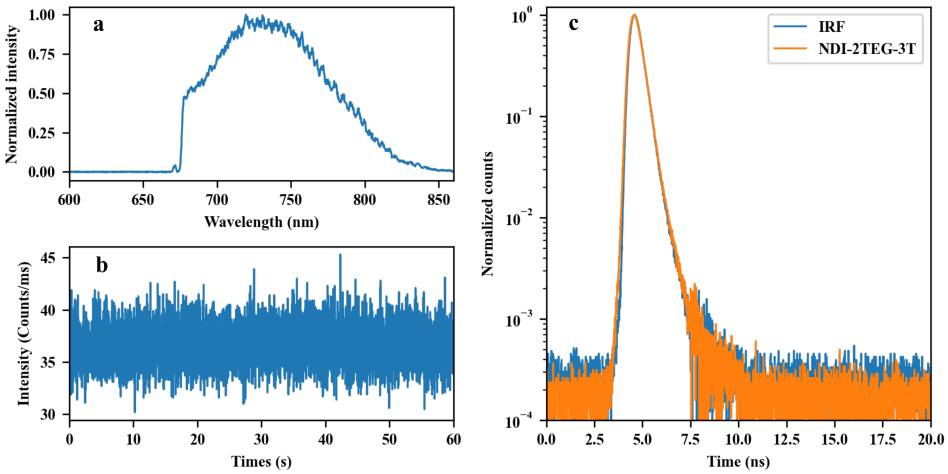

Figure S3.7: Non-enhanced fluorescence of NDI-2TEG-3T in the focal volume of the microscope. (a) Photoluminescence spectrum of NDI-2TEG-3T. (b) Photoluminescence time trace of non-enhanced molecules in the focal volume.(c) Lifetime histogram curve of NDI-2TEG-3T molecules (orange) in bulk solution. The lifetime of NDI-2TEG-3T is much shorter than the time resolution of our setup, as the curve is completely indistinguishable from the instrument response function (IRF, blue), which has an exponential decay with a time of about 0.38 ns.The molecular concentration of NDI-2TEG-3T was kept equal to 50 μM.

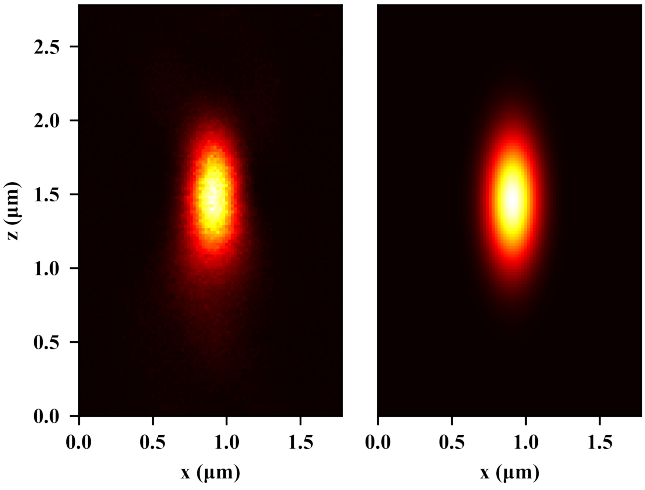

Figure S3.8: Left, XZ cross section of the scattering point spread function (PSF) with a gold nanorod. Right, two-dimensional Gaussian fit of the PSF, from which we get the widths of the PSF, $w_x = 0.24\,\mu$m and $w_z = 0.58\,\mu$m, and the PSF volume of 0.061 fL.

citation power was 3.3 times larger, and the concentration of molecules was higher. A $50\ \mu\mathrm{M}$ solution of NDI-2TEG-3T was excited with a $671\ \mathrm{nm}$ continuous wave (CW) laser (circularly polarized), and the fluorescence signal was separated from the background of scattered light by means of a long-pass filter ($\geq 675\ \mathrm{nm}$, LongPass U-Grade 671/RazorEdge, Semrock). The fluorescence intensity collected from the focal volume is depicted as time trace in Figure S3.7.b, and the corresponding emission spectrum of the non-enhanced molecules is shown in Figure S3.7.a. From the time trace, we got the average fluorescence intensity of about $36 \pm 6\ \mathrm{counts/ms}$. By considering that all the photoluminescence photons were due to the contribution of molecules in the focal volume, we got an estimated value of about $20 \pm 3\ \mathrm{counts/s}$ for the average intensity of each molecule. The focal volume is approximated by the volume of the point spread function of the microscope, which is about $0.061\ \mathrm{fL}$ (see Figure S3.8). Considering the difference in power, we estimated $6 \pm 1\ \mathrm{counts/s}$ the rate detected counts per molecule for the calculation of the enhancement factors.

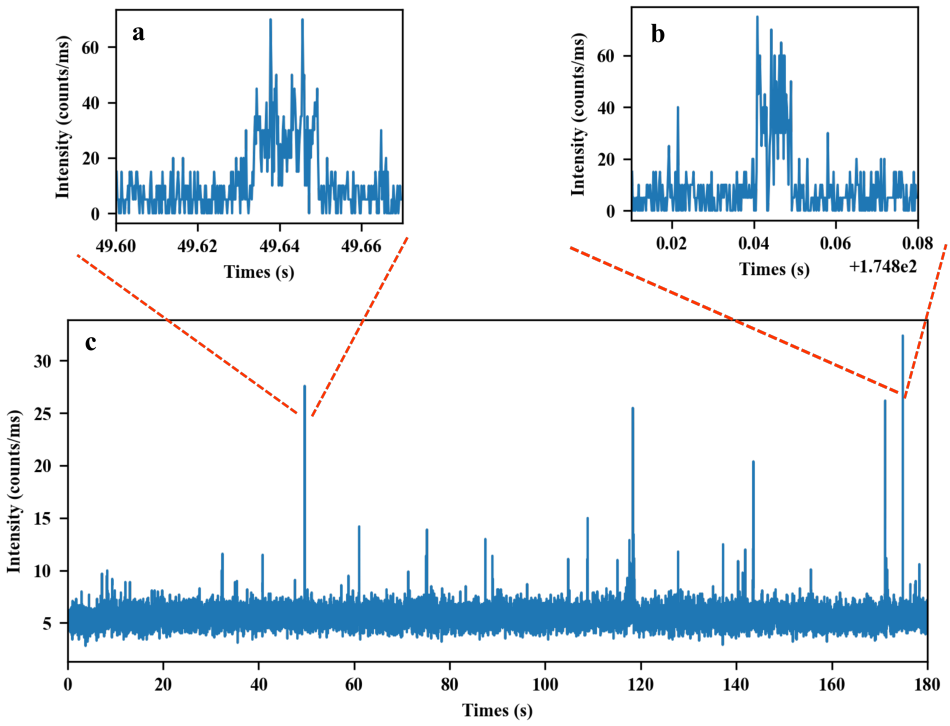

Figure S3.9: Single-molecule fluorescence enhancement by a gold nanorod. (c) Photoluminescence time trace with the binning time of 10 ms. (a, b) The zoomed views of the two highest bursts of the time trace in (a) with the binning time of 200 μs. The single-step intensity changes of these bursts confirm that the enhanced fluorescence signals are stemming from single molecules.

Single-molecule Fluorescence of NDI-2TEG-3T Enhanced by a Gold Nanorod.

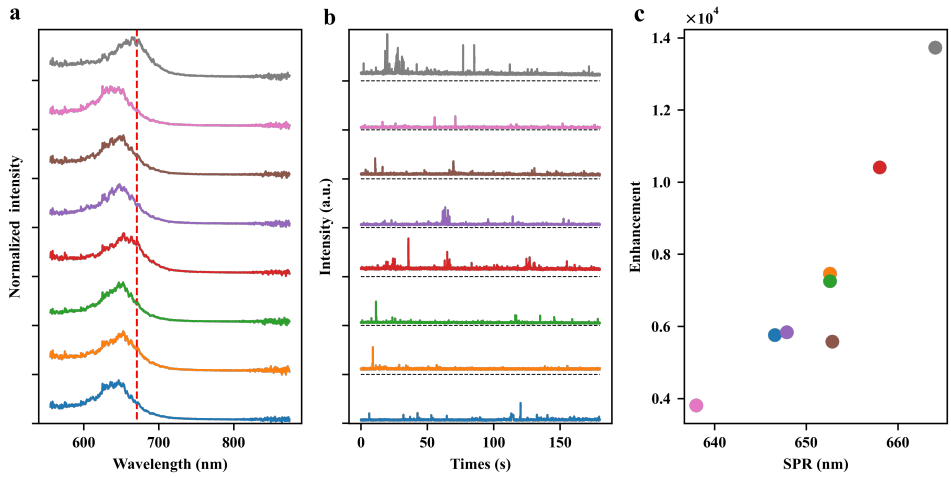

Figure S3.10: (a) Photoluminescence spectra of gold nanorods with different plasmon resonances. The red dashed line represents the excitation laser's wavelength of 671 nm. (b) The corresponding fluorescence time traces recorded on these gold nanorods, and (c) the maximum fluorescence enhancement as a function of the plasmon wavelength. The data recorded on every gold nanorod are indicated by their color in the plots. All time traces were recorded at the same molecular concentration of 1 μM.

S3.1.2. Theoretical Framework

Fluorescence enhancement simulations

In this paper, we follow the notations and definitions of Khatua et al. [24]. We consider the single molecule as a dipole $\mathbf{p_0}$ oscillating with frequency ω. As the theoretical absorption rate of the molecule is proportional to the intensity of the local field at its position, the excitation enhancement factor by a nanoantenna can be expressed as

$$\xi_{\mathrm{exc}} = \frac{I(\omega_{\mathrm{exc}})}{I_0(\omega_{\mathrm{exc}})} = \frac{|\mathbf{E}(\omega_{\mathrm{exc}})|^2}{|\mathbf{E}_0(\omega_{\mathrm{exc}})|^2}, \tag{S3.2}$$

where $\mathbf{E}(\omega_{\mathrm{exc}})$ and $\mathbf{E}_0(\omega_{\mathrm{exc}})$ are the electric fields at the position of the dipole with and without the nanoantenna, and ω_{exc} is the frequency of the illuminating light source. In the vicinity of the nanoantenna, the decay rate of the excited molecule is modified by coupling to the plasmon mode. On the basis of a simple two-level scheme, the emission factor can been expressed as[24]

$$\xi_{\mathrm{em}} = \xi_{\mathrm{rad}} \frac{\eta_0 C_{\mathrm{abs}} I_{\mathrm{exc}}/k_{\mathrm{r}}^0 + 1}{\xi_{\mathrm{exc}} \cdot \eta_0 C_{\mathrm{abs}} I_{\mathrm{exc}}/k_{\mathrm{r}}^0 + 1 + \eta_0(\xi_{\mathrm{rad}} + K_{\mathrm{nr}}/k_{\mathrm{r}}^0 - 1)}, \tag{S3.3}$$

here, I_{exc} is the intensity of the excitation wave, C_{abs} is the absorption cross section of the molecules, and $\xi_{\mathrm{rad}} = k_{\mathrm{r}}/k_{\mathrm{r}}^0$ is the radiative enhancement factor, which accounts for the increased local density of states in the vicinity of the antenna (Purcell effect [2, 52]). k_r and k_r^0 are the radiative decay rates with and without the nanoantenna, respectively, η_0 is the

intrinsic quantum yield of the emitter, and K_{nr} is the additional non-radiative absorption rate due to dissipative losses of the nanoantenna.

In Eq (S3.3), $\eta_0 C_{\mathrm{abs}} I_{\mathrm{exc}}$ accounts for the non-enhanced fluorescence rates of single molecules, which in our experiment is less than $10\ \mathrm{counts/s}$ (see previous section). From the simulations (see figure S3.11a.), the maximum radiative enhancement factor ($\xi_{\mathrm{rad,max}}$) and the additional non-radiative absorption rate ($K_{\mathrm{nr,max}}/k_{\mathrm{r}}^0$) are

$$\xi_{\mathrm{rad,max}} \sim 330, \tag{S3.4}$$

and

$$K_{\mathrm{nr,max}}/k_{\mathrm{r}}^0 \sim 4300. \tag{S3.5}$$

The intrinsic radiative rate of the molecules can be deduced from the quantum yield η_0 and the fluorescence lifetime τ_0 as $k_{\mathrm{r}}^0 = \eta_0/\tau_0$. For NDI-2TEG-3T, $\eta_0 \sim 1 \times 10^{-4}$ and $\tau_0 < 0.5\ \mathrm{ns}$. Therefore, we have

$$k_{\mathrm{r}}^0 > 2 \times 10^5\ \mathrm{s}^{-1}. \tag{S3.6}$$

From the discussion above, we find that, in our experiment conditions,

$$\eta_0 C_{\mathrm{abs}} I_{\mathrm{exc}}/k_{\mathrm{r}}^0 < 5 \times 10^{-5} \ll 1, \tag{S3.7}$$

and

$$\xi_{\mathrm{exc}} \eta_0 C_{\mathrm{abs}} I_{\mathrm{exc}}/k_{\mathrm{r}}^0 < 0.04 \ll \eta_0(\xi_{\mathrm{rad}} + K_{\mathrm{nr}}/k_{\mathrm{r}}^0 - 1) \sim 0.46, \tag{S3.8}$$

which means that the saturation of excitation is negligible. Therefore, the emission enhancement factor can been expressed as

$$\xi_{\mathrm{em}} = \frac{\xi_{\mathrm{rad}}}{1 + \eta_0(\xi_{\mathrm{rad}} + K_{\mathrm{nr}}/k_{\mathrm{r}}^0 - 1)}. \tag{S3.9}$$

In the discussions above, we have taken $0.5\ \mathrm{ns}$ as an upper bound for the NDI-2TEG-3T lifetime, which is in fact much shorter than the time resolution of our setup, as can be seen from the lifetime measurement in Figure S3.7.c. Therefore, in our experiment, we will be even further away from saturation than indicated by conditions of (S3.8), further supporting the simplified model of the emission enhancement factor in Eq (S3.9).

Consequently, the fluorescence intensity coming from the enhanced emitter is

$$I_{\mathrm{fluo}} = I_{\mathrm{exc}} \cdot C_{\mathrm{abs}} \cdot \eta_0 \cdot \xi_{\mathrm{exc}} \cdot \xi_{\mathrm{em}}. \tag{S3.10}$$

Considering the photoluminescence signal I_{GNR} of the gold nanorod as the only source of background, we can define the signal-to-noise ratio of the coupled system between the emitter and the gold nanorod as

$$S/N = I_{\mathrm{fluo}} \cdot \Delta t/\sqrt{I_{\mathrm{GNR}} \cdot \Delta t}, \tag{S3.11}$$

where Δt is the binning time for single-photon counting, supposing the signal to remain constant during the acquisition time.

To evaluate the enhancement factor by a single gold nanorod numerically, we applied a classical electrodynamics approach based on a boundary element method (SCUFF-EM)

to simulate the excitation and emission enhancement, respectively [53, 54]. To get the excitation enhancement, we assumed the gold nanorod is excited by a plane wave, while for the decay rates, we modeled the excited emitter as a radiating dipole, whose time-averaged radiated power in a medium without nanorod is

$$P_{r0}(\omega) = \frac{|\mathbf{p}_0|^2}{4\pi\varepsilon_0}\frac{n\omega^4}{3c^3}, \tag{S3.12}$$

where n is the refractive index of the medium, c is the speed of light and ε_0 is the vacuum permittivity. The enhancement factor of radiative rates (ξ_{rad}) and the non-radiative dissipation rate (K_{nr}) by the nanoantenna were derived from

$$\xi_{\mathrm{rad}} = k_{\mathrm{r}}/k_{\mathrm{r}}^0 = P_{\mathrm{rad}}/P_{\mathrm{r0}}, \tag{S3.13}$$

and

$$K_{\mathrm{nr}}/k_{\mathrm{r}}^0 = P_{\mathrm{abs}}/P_{\mathrm{r0}}. \tag{S3.14}$$

In the simulations, the power absorbed by the gold nanorod P_{abs} was calculated by integrating the Poynting vector over the nanorod surface, which was modeled as a spherically capped cylinder, and the radiated power P_{rad} was obtained from

$$P_{\mathrm{rad}}(\omega) + P_{\mathrm{abs}}(\omega) = \frac{\omega^3}{2c^2\varepsilon_0}|\mathbf{p}_0|^2[\mathbf{n}\cdot\mathrm{Im}[\mathbf{G}(\mathbf{r},\mathbf{r};\omega)]\cdot\mathbf{n}], \tag{S3.15}$$

where $\mathbf{G}(\mathbf{r},\mathbf{r};\omega)$ is the Green tensor at the emitter's position $\mathbf{r}$ and $\mathbf{n}$ represents the direction of the dipole moment[55].

From Eqs. (S3.12) and (S3.15), we can clearly see that the radiative rate enhancement ($\xi_{\mathrm{rad}}^{\omega}$) and the non-radiative relaxation rate $K_{\mathrm{nr}}^{\omega}(\omega)$ both depend on the frequency of the emitted photons (ω). To get the emission enhancement for all the photons, we calculate the average radiative rate enhancement and non-radiative relaxation rate:

$$\xi_{\mathrm{rad}} = \int \xi_{\mathrm{rad}}^{\omega}(\omega)F_{\mathrm{dye}}(\omega)d\omega, \tag{S3.16}$$

$$K_{\mathrm{nr}} = \int K_{\mathrm{nr}}^{\omega}(\omega)F_{\mathrm{dye}}(\omega)d\omega, \tag{S3.17}$$

here, $F_{\mathrm{dye}}(\omega)$ is the normalized emission spectra of the molecule and $\int F_{\mathrm{dye}}(\omega)d\omega = 1$.

Dependence of the Emission Enhancement on the Gap and on the Quantum Yield

The simple cube root dependence of the optimal gap on the quantum yield (Fig S3.11c.) can be explained briefly as followed. At a given quantum yield, considering the emission enhancement factor as a function of the gap, the derivative of Eq (S3.9) at the optimal gap d_{m} gives

$$\frac{d\xi_{\mathrm{em}}}{d(\mathrm{gap})}\Big|_{\mathrm{gap=d_m}} = \frac{d}{d(\mathrm{gap})}\left[\frac{\xi_{\mathrm{rad}}}{1+\eta_0(\xi_{\mathrm{rad}}+K_{\mathrm{nr}}/k_{\mathrm{r}}^0-1)}\right]\Bigg|_{\mathrm{gap=d_m}} = 0, \tag{S3.18}$$

from which we can get a relationship between the quantum yield and the optimal gaps as,

$$\eta_0 = \frac{1}{\frac{\xi_{\mathrm{rad}}}{\xi'_{\mathrm{rad}}} K'_{\mathrm{nr}}/k^0_{\mathrm{r}} - K_{\mathrm{nr}}/k^0_{\mathrm{r}} + 1}, \tag{S3.19}$$

here, $\xi'_{\mathrm{rad}} = \frac{d}{d(\mathrm{gap})}\xi_{\mathrm{rad}}(\mathrm{gap})\big|_{\mathrm{gap}=\mathrm{d_m}}$ and $K'_{\mathrm{nr}} = \frac{d}{d(\mathrm{gap})}K_{\mathrm{nr}}(\mathrm{gap})\big|_{\mathrm{gap}=\mathrm{d_m}}$.

Considering the simplest power dependence of the enhanced radiative and nonradiative rates on the gap: $\xi_{\mathrm{rad}}(\mathrm{gap}) \propto \mathrm{gap}^{-\alpha}$ and $K_{\mathrm{nr}}(\mathrm{gap})/k^0_{\mathrm{r}} \propto \mathrm{gap}^{-\beta}$, Eq (S3.19) can be expressed as

$$\eta_0 = \frac{1}{(\beta/\alpha - 1)K_{\mathrm{nr}}/k^0_{\mathrm{r}} + 1} \approx \frac{1}{(\beta/\alpha - 1)}(K_{\mathrm{nr}}/k^0_{\mathrm{r}})^{-1} \propto {\mathrm{d_m}}^{\beta}, \tag{S3.20}$$

from this, we get the power law approximation for the optimal gap: $\mathrm{d_m} \propto \eta_0^{1/\beta}$. Here $\beta > \alpha$, because the enhanced non-radiative rates decreases more rapidly than the radiative rates as the molecules move away from the metal surface(Figure S3.11.a). The decay rate β can vary from 3 to 6[56], depending on the geometric configuration of the coupling system, such as the surface curvature of the particle, the position and orientation of the molecules et al. In our case, for the typical size of gold nanorod, we find that $\beta \sim 3$ gives a good approximation (Figure S3.11), therefore $\mathrm{d_m} \propto \eta_0^{1/3}$.

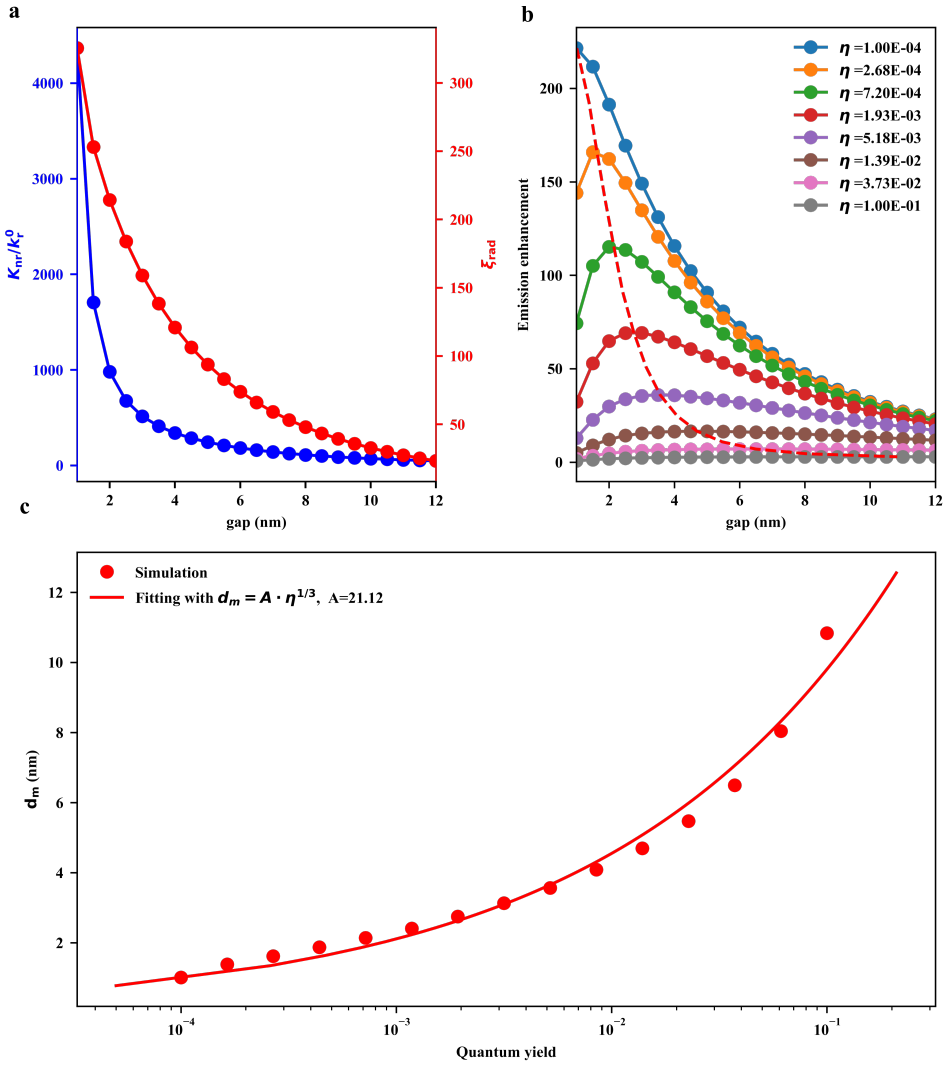

Figure S3.11: (a) Radiative rate enhancement factor (red) and additional non-radiative rate (blue) as functions of the gap. (b) Emission enhancement as a function of the gap for the molecules with different quantum yields. Red dashed line indicates the maximum emissions of different quantum yields. (c) The corresponding positions (d_m) of maximum emission enhancements for different quantum yields. Here, we find that the quantum yield dependence of the optimal distance can be approximated by a very simple power law as $d_\mathrm{m} \propto \eta^{\frac{1}{3}}$.

Dual-Lorentzian Model for Fluorescence Enhancement by a Gold Nanorod

In order to quickly optimize plasmon enhanced fluorescence without performing time consuming fullwave-simulation, we can apply a dual-Lorentzian model to the gold nanorod-emitter system for the molecules with very low quantum yields. As we can see from Eq (S3.9), the emission enhancement ξ_{em} reduces to the radiative enhancement ξ_{rad} for vanishing quantum yields:

$$\xi_{\mathrm{em}} \sim \xi_{\mathrm{rad}}[1-\eta_0(\xi_{\mathrm{rad}}+K_{\mathrm{nr}}/k_{\mathrm{r}}^0-1)] \xrightarrow{\eta_0\to 0} \xi_{\mathrm{rad}}, \tag{S3.21}$$

The emission enhancement factor ξ_{rad} depends on the frequency (ω) of the emitted photon and on the plasmon frequency (ω_{sp}) of the nanorod and can be expressed as an integral over all emitted photons (as in Eq. (S3.16)):

$$\xi_{\mathrm{em,avg}}(\omega_{\mathrm{sp}}) \sim \int \xi_{\mathrm{rad}}^{\omega}(\omega_{\mathrm{sp}},\omega)F_{\mathrm{dye}}(\omega)d\omega. \tag{S3.22}$$

Substituting this Eq. (S3.22) into the Eq. (S3.10), we can estimate the enhanced fluorescence intensity from the molecule, which is linearly dependent on the molecular absorption spectrum and emission, and the plasmon response of the gold nanorod (represented by the enhancement factors of excitation and radiative rates),

$$\begin{aligned} I_{fluo}(\omega_{\mathrm{exc}},\omega_{\mathrm{sp}}) &= I_{\mathrm{exc}}\cdot C_{\mathrm{abs}}(\omega_{\mathrm{exc}})\cdot\eta_0\cdot\xi_{\mathrm{exc}}(\omega_{\mathrm{exc}},\omega_{\mathrm{sp}})\cdot\xi_{\mathrm{em,avg}}(\omega_{\mathrm{sp}}) \\ &\sim I_{\mathrm{exc}}\cdot\eta_0\cdot\int C_{\mathrm{abs}}(\omega_{\mathrm{exc}})\cdot\underbrace{[\xi_{\mathrm{exc}}(\omega_{\mathrm{exc}},\omega_{\mathrm{sp}})\cdot\xi_{\mathrm{rad}}^{\omega}(\omega_{\mathrm{sp}},\omega)]}_{\text{plasmon response}}\cdot F_{\mathrm{dye}}(\omega)d\omega. \end{aligned} \tag{S3.23}$$

As a result of the square dependence on the near-field, both the enhanced excitation and emission rates, $\xi_{\mathrm{ext}}(\omega_{exc},\omega_{\mathrm{sp}})$ and $\xi_{\mathrm{rad}}(\omega_{\mathrm{sp}},\omega)$, have similar lineshapes as the spectra of the the gold nanorod plasmon resonance, all of which can be expressed by using the same Lorentzian lineshape

$$\xi_{[\mathrm{exc,rad}]}(\omega_i,\omega_{\mathrm{sp}}) \sim L_{[\mathrm{exc,rad}]}(\omega_{\mathrm{sp}})\cdot\frac{\Gamma/2}{(\omega_i-\omega_{\mathrm{sp}})^2+(\Gamma/2)^2}, \tag{S3.24}$$

where, Γ is the width of the plasmon resonance, ω_i represents the frequencies of excitation, emission, or scattering photons by the nanorod. $L_{[\mathrm{exc,rad}]}(\omega_{\mathrm{sp}})$ is the normalization factor, which depends on plasmon wavelengths of the nanorods. Simply, we can set $L_{\mathrm{rad}}(\omega_{\mathrm{sp}})$ as a constant, and $L_{\mathrm{exc}}(\omega_{\mathrm{sp}}) \propto C_{\mathrm{sca}}(\omega_{\mathrm{sp}})$. Here $C_{\mathrm{sca}}(\omega_{\mathrm{sp}})$ is the scattering cross section of the nanorod at resonance wavelength, which can be easily calculated by using Mie-Gans theory (green dashed line in Figure S3.12)[57].

From Eq. (S3.23) and Eq. (S3.24), we can get a quick estimation of the dependence of the enhancement factors and the fluorescence intensity on wavelengths of the excitation and of the plasmon resonance, by simply considering the spectral overlap of the molecular absorption and emission and the square of Lorentzian lineshape of the plasmon resonance. This simplified form allows us to select the best experimental condition to get maximum intensity without the need for time-consuming fullwave-simulations. As an example, in our case we got $\omega_{\mathrm{exc}} = 669$ nm and $\omega_{\mathrm{sp}} = 674$ nm, which is very close to the full-wave simulation result as shown in Figure 1.c in the main text. The detailed comparison of the

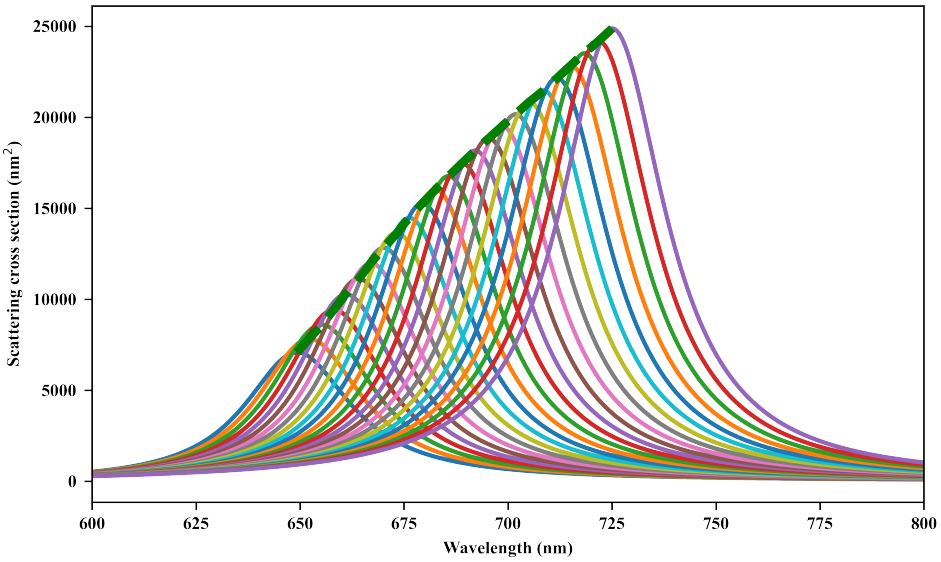

Figure S3.12: Scattering cross section of gold nanorods with the same diameter but with different aspect ratios. The green dashed line gives the values at the resonance wavelengths, which are proportional to normalization factors $L_{\mathrm{exc}}(\omega_{\mathrm{sp}})$ in Eq. (S3.24). The cross sections were calculated by using Mie-Gans theory, where the diameter of the gold nanorods was a constant set as 25 nm.

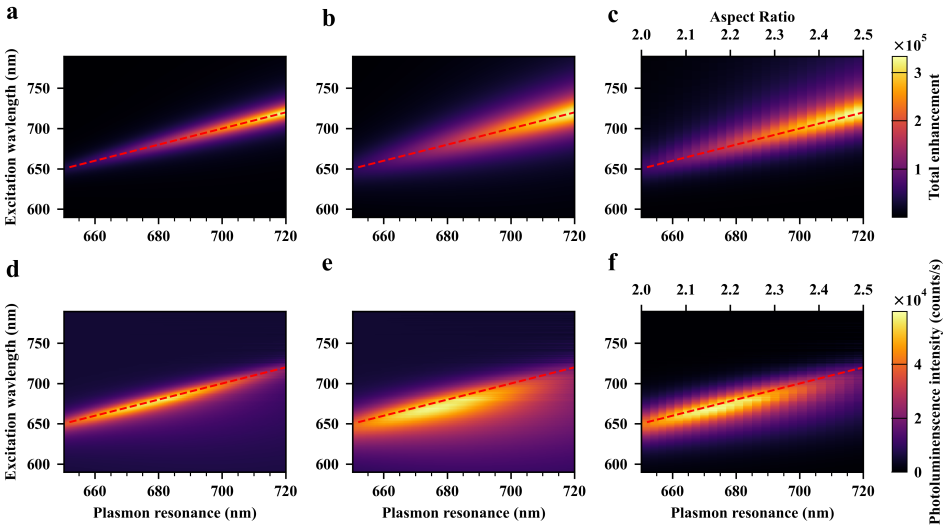

Figure S3.13: Dual-Lorentzian model for gold nanorod-emitter system. (a, b, c) are the total fluorescence enhancement as a function of excitation wavelength and plasmon wavelength of the gold nanorod, (d, e, f) are the corresponding fluorescence intensities. Here, (a, d) correspond to the Lorentzian model with the FWHM of 20 nm, (b, e) correspond to FWHM of 40 nm, and (c, f) were calculated with full-wave simulations.

full-wave simulation and the models with different full width at half maximum (FWHM) of the gold nanorod plasmon is shown in Figure S3.13. From the Figure S3.13.(e, f), we can see that the “sweet spot" for the optimized fluorescence is the same for the wavelengths of the excitation and plasmon. We should mention here, as we can see in Figure S3.13.(b,c), that the optimized wavelengths of excitation and plasmon to get maximum total enhancement are much red-shifted compared to the fluorescence intensity, due to the large Stokes shift ($3,000\ \mathrm{cm}^{-1}$) of the molecule.

References

[1] C. Zander, J. Enderlein, and R. A. Keller. *Single-molecule detection in solution—methods and applications.* VCH-Wiley, 2002.

[2] Guowei Lu, Tianyue Zhang, Wenqiang Li, Lei Hou, Jie Liu, and Qihuang Gong. Single-Molecule Spontaneous Emission in the Vicinity of an Individual Gold Nanorod. *The Journal of Physical Chemistry C*, 115(32):15822–15828, August 2011.

[3] W. Ho. Single-molecule chemistry. *The Journal of Chemical Physics*, 117(24):11033–11061, December 2002.

[4] Denis Garoli, Hirohito Yamazaki, Nicolò Maccaferri, and Meni Wanunu. Plasmonic Nanopores for Single-Molecule Detection and Manipulation: Toward Sequencing Applications. *Nano Letters*, 19(11):7553–7562, November 2019.

[5] Aleksandr Barulin, Jean-Benoît Claude, Satyajit Patra, Nicolas Bonod, and Jérôme Wenger. Deep Ultraviolet Plasmonic Enhancement of Single Protein Autofluorescence in Zero-Mode Waveguides. *Nano Letters*, 19(10):7434–7442, October 2019.

[6] W. E. Moerner and L. Kador. Optical detection and spectroscopy of single molecules in a solid. *Physical Review Letters*, 62(21):2535–2538, May 1989.

[7] W. E. Moerner and Michel Orrit. Illuminating Single Molecules in Condensed Matter. *Science*, 283(5408):1670–1676, March 1999.

[8] W. E. (William E.) Moerner. Nobel Lecture: Single-molecule spectroscopy, imaging, and photocontrol: Foundations for super-resolution microscopy. *Reviews of Modern Physics*, 87(4):1183–1212, October 2015.

[9] M. Orrit and J. Bernard. Single pentacene molecules detected by fluorescence excitation in a p-terphenyl crystal. *Physical Review Letters*, 65(21):2716–2719, November 1990.

[10] Taekjip Ha. Single-Molecule Fluorescence Resonance Energy Transfer. *Methods*, 25(1):78–86, September 2001.

[11] Richard A. Keller, W. Patrick Ambrose, Peter M. Goodwin, James H. Jett, John C. Martin, and Ming Wu. Single-Molecule Fluorescence Analysis in Solution. *Applied Spectroscopy*, 50(7):12A–32A, July 1996.

[12] W. E. Moerner and David P. Fromm. Methods of single-molecule fluorescence spectroscopy and microscopy. *Review of Scientific Instruments*, 74(8):3597–3619, August 2003.

[13] Pascal Anger, Palash Bharadwaj, and Lukas Novotny. Enhancement and Quenching of Single-Molecule Fluorescence. *Physical Review Letters*, 96(11):113002, March 2006.

[14] Joseph R Lakowicz. *Principles of fluorescence spectroscopy*. Springer Science & Business Media, 2013.

[15] Jeff W. Lichtman and José-Angel Conchello. Fluorescence microscopy. *Nature Methods*, 2(12):910–919, December 2005.

[16] Jianhong Chen, Weimin Liu, Bingjiang Zhou, Guangle Niu, Hongyan Zhang, Jiasheng Wu, Ying Wang, Weigang Ju, and Pengfei Wang. Coumarin- and Rhodamine-Fused Deep Red Fluorescent Dyes: Synthesis, Photophysical Properties, and Bioimaging in Vitro. *The Journal of Organic Chemistry*, 78(12):6121–6130, June 2013.

[17] Melari Davies, Christophe Jung, Philipp Wallis, Tobias Schnitzler, Chen Li, Klaus Müllen, and Christoph Bräuchle. Photophysics of New Photostable Rylene Derivatives: Applications in Single-Molecule Studies and Membrane Labelling. *ChemPhysChem*, 12(8):1588–1595, 2011.

[18] BR Henry and W Siebrand. Organic molecular photophysics. *by JB Birks, Wiley, New York*, 1:153, 1973.

[19] Jord C. Prangsma, Robert Molenaar, Laura van Weeren, Daphne S. Bindels, Lindsay Haarbosch, Jente Stouthamer, Theodorus W. J. Gadella, Vinod Subramaniam, Willem L. Vos, and Christian Blum. Quantitative Determination of Dark Chromophore Population Explains the Apparent Low Quantum Yield of Red Fluorescent Proteins. *The Journal of Physical Chemistry B*, 124(8):1383–1391, February 2020.

[20] Kateryna S. Morozova, Kiryl D. Piatkevich, Travis J. Gould, Jinghang Zhang, Joerg Bewersdorf, and Vladislav V. Verkhusha. Far-Red Fluorescent Protein Excitable with Red Lasers for Flow Cytometry and Superresolution STED Nanoscopy. *Biophysical Journal*, 99(2):L13–L15, July 2010.

[21] Daria M. Shcherbakova and Vladislav V. Verkhusha. Near-infrared fluorescent proteins for multicolor in vivo imaging. *Nature Methods*, 10(8):751–754, August 2013.

[22] Sergei Kühn, Ulf Håkanson, Lavinia Rogobete, and Vahid Sandoghdar. Enhancement of Single-Molecule Fluorescence Using a Gold Nanoparticle as an Optical Nanoantenna. *Physical Review Letters*, 97(1):017402, July 2006.

[23] Paolo Ponzellini, Xavier Zambrana-Puyalto, Nicolò Maccaferri, Luca Lanzanò, Francesco De Angelis, and Denis Garoli. Plasmonic zero mode waveguide for highly confined and enhanced fluorescence emission. *Nanoscale*, 10(36):17362–17369, September 2018.

[24] Saumyakanti Khatua, Pedro M. R. Paulo, Haifeng Yuan, Ankur Gupta, Peter Zijlstra, and Michel Orrit. Resonant Plasmonic Enhancement of Single-Molecule Fluorescence by Individual Gold Nanorods. *ACS Nano*, 8(5):4440–4449, May 2014.

[25] Haifeng Yuan, Saumyakanti Khatua, Peter Zijlstra, Mustafa Yorulmaz, and Michel Orrit. Thousand-fold Enhancement of Single-Molecule Fluorescence Near a Single Gold Nanorod. *Angewandte Chemie International Edition*, 52(4):1217–1221, 2013.

[26] Saumyakanti Khatua, Haifeng Yuan, and Michel Orrit. Enhanced-fluorescence correlation spectroscopy at micro-molar dye concentration around a single gold nanorod. *Physical Chemistry Chemical Physics*, 17(33):21127–21132, August 2015.

[27] Deep Punj, Mathieu Mivelle, Satish Babu Moparthi, Thomas S. van Zanten, Hervé Rigneault, Niek F. van Hulst, María F. García-Parajó, and Jérôme Wenger. A plasmonic 'antenna-in-box' platform for enhanced single-molecule analysis at micromolar concentrations. *Nature Nanotechnology*, 8(7):512–516, July 2013.

[28] Deep Punj, Juan de Torres, Hervé Rigneault, and Jérôme Wenger. Gold nanoparticles for enhanced single molecule fluorescence analysis at micromolar concentration. *Optics Express*, 21(22):27338–27343, November 2013.

[29] Valentin Flauraud, Raju Regmi, Pamina M. Winkler, Duncan T. L. Alexander, Hervé Rigneault, Niek F. van Hulst, María F. García-Parajo, Jérôme Wenger, and Jürgen Brugger. In-Plane Plasmonic Antenna Arrays with Surface Nanogaps for Giant Fluorescence Enhancement. *Nano Letters*, 17(3):1703–1710, March 2017.

[30] Anastasiya Puchkova, Carolin Vietz, Enrico Pibiri, Bettina Wünsch, María Sanz Paz, Guillermo P. Acuna, and Philip Tinnefeld. DNA Origami Nanoantennas with over 5000-fold Fluorescence Enhancement and Single-Molecule Detection at 25 μM. *Nano Letters*, 15(12):8354–8359, December 2015.

[31] Anika Kinkhabwala, Zongfu Yu, Shanhui Fan, Yuri Avlasevich, Klaus Müllen, and W. E. Moerner. Large single-molecule fluorescence enhancements produced by a bowtie nanoantenna. *Nature Photonics*, 3(11):654–657, November 2009.

[32] Anika A. Kinkhabwala, Zongfu Yu, Shanhui Fan, and W. E. Moerner. Fluorescence correlation spectroscopy at high concentrations using gold bowtie nanoantennas. *Chemical Physics*, 406:3–8, October 2012.

[33] Peter Zijlstra, Pedro M. R. Paulo, and Michel Orrit. Optical detection of single non-absorbing molecules using the surface plasmon resonance of a gold nanorod. *Nature Nanotechnology*, 7(6):379–382, June 2012.

[34] Leonid Vigderman, Bishnu P. Khanal, and Eugene R. Zubarev. Functional Gold Nanorods: Synthesis, Self-Assembly, and Sensing Applications. *Advanced Materials*, 24(36):4811–4841, 2012.

[35] Huanjun Chen, Lei Shao, Qian Li, and Jianfang Wang. Gold nanorods and their plasmonic properties. *Chemical Society Reviews*, 42(7):2679–2724, March 2013.

[36] Joseph R. Lakowicz. Radiative decay engineering 5: Metal-enhanced fluorescence and plasmon emission. *Analytical Biochemistry*, 337(2):171–194, February 2005.

[37] O. L. Muskens, V. Giannini, J. A. Sánchez-Gil, and J. Gómez Rivas. Strong Enhancement of the Radiative Decay Rate of Emitters by Single Plasmonic Nanoantennas. *Nano Letters*, 7(9):2871–2875, September 2007.

[38] R. Carminati, J. J. Greffet, C. Henkel, and J. M. Vigoureux. Radiative and non-radiative decay of a single molecule close to a metallic nanoparticle. *Optics Communications*, 261(2):368–375, May 2006.

[39] David Canevet, Marc Sallé, Guanxin Zhang, Deqing Zhang, and Daoben Zhu. Tetrathiafulvalene (TTF) derivatives: Key building-blocks for switchable processes. *Chemical Communications*, (17):2245–2269, April 2009.

[40] Yanlin Chen, Xianfeng Liang, Haiyan Yang, Qin Wang, Xubing Zhou, De Guo, Shayu Li, Cailong Zhou, Lichun Dong, Zitong Liu, Zhengxu Cai, Wei Chen, and Luxi Tan. Strong Near-Infrared Solid Emission and Enhanced N-Type Mobility for Poly(naphthalene Diimide) Vinylene by a Random Polymerization Strategy. *Macromolecules*, 52(21):8332–8338, November 2019.

[41] P. B. Johnson and R. W. Christy. Optical Constants of the Noble Metals. *Physical Review B*, 6(12):4370–4379, December 1972.

[42] E. Dulkeith, A. C. Morteani, T. Niedereichholz, T. A. Klar, J. Feldmann, S. A. Levi, F. C. J. M. van Veggel, D. N. Reinhoudt, M. Möller, and D. I. Gittins. Fluorescence Quenching of Dye Molecules near Gold Nanoparticles: Radiative and Nonradiative Effects. *Physical Review Letters*, 89(20):203002, October 2002.

[43] Fabio Cannone, Giuseppe Chirico, Anna Rita Bizzarri, and Salvatore Cannistraro. Quenching and Blinking of Fluorescence of a Single Dye Molecule Bound to Gold Nanoparticles. *The Journal of Physical Chemistry B*, 110(33):16491–16498, August 2006.

[44] Sinisa Vukovic, Stefano Corni, and Benedetta Mennucci. Fluorescence Enhancement of Chromophores Close to Metal Nanoparticles. Optimal Setup Revealed by the Polarizable Continuum Model. *The Journal of Physical Chemistry C*, 113(1):121–133, January 2009.

[45] Martín Caldarola, Biswajit Pradhan, and Michel Orrit. Quantifying fluorescence enhancement for slowly diffusing single molecules in plasmonic near fields. *The Journal of Chemical Physics*, 148(12):123334, March 2018.

[46] Biswajit Pradhan, Saumyakanti Khatua, Ankur Gupta, Thijs Aartsma, Gerard Canters, and Michel Orrit. Gold-Nanorod-Enhanced Fluorescence Correlation Spectroscopy of Fluorophores with High Quantum Yield in Lipid Bilayers. *The Journal of Physical Chemistry C*, 120(45):25996–26003, November 2016.

[47] A. Mooradian. Photoluminescence of Metals. *Physical Review Letters*, 22(5):185–187, February 1969.

[48] Weichun Zhang, Martín Caldarola, Xuxing Lu, Biswajit Pradhan, and Michel Orrit. Single-molecule fluorescence enhancement of a near-infrared dye by gold nanorods using DNA transient binding. *Physical Chemistry Chemical Physics*, 20(31):20468–20475, August 2018.

[49] Eilaf Ahmed, Guoqiang Ren, Felix S. Kim, Emily C. Hollenbeck, and Samson A. Jenekhe. Design of New Electron Acceptor Materials for Organic Photovoltaics: Synthesis, Electron Transport, Photophysics, and Photovoltaic Properties of Oligothiophene-Functionalized Naphthalene Diimides. *Chemistry of Materials*, 23(20):4563–4577, October 2011.

[50] Dávid Komáromy, Marc C. A. Stuart, Guillermo Monreal Santiago, Meniz Tezcan, Victor V. Krasnikov, and Sijbren Otto. Self-Assembly Can Direct Dynamic Covalent Bond Formation toward Diversity or Specificity. *Journal of the American Chemical Society*, 139(17):6234–6241, May 2017.

[51] Heather F. Higginbotham, Subashani Maniam, Steven J. Langford, and Toby D. M. Bell. New brightly coloured, water soluble, core-substituted naphthalene diimides for biophysical applications. *Dyes and Pigments*, 112:290–297, January 2015.

[52] Anonymous. Proceedings of the American Physical Society. *Physical Review*, 69(11-12):674–674, June 1946.

[53] M. T. Homer Reid and Steven G. Johnson. Efficient Computation of Power, Force, and Torque in BEM Scattering Calculations. *IEEE Transactions on Antennas and Propagation*, 63(8):3588–3598, August 2015.

[54] `http://github.com/homerreid/scuff-EM`.

[55] Lukas Novotny and Bert Hecht. *Principles of Nano-Optics*. Cambridge University Press, 2006.

[56] Maxim Sukharev, Noa Freifeld, and Abraham Nitzan. Numerical Calculations of Radiative and Non-Radiative Relaxation of Molecules Near Metal Particles. *The Journal of Physical Chemistry C*, 118(20):10545–10551, May 2014.

[57] R v Gans. Über die form ultramikroskopischer silberteilchen. *Annalen der Physik*, 352(10):270–284, 1915.

4

Controlled synthesis of gold nanorod dimers with end-to-end configurations

End-to-end gold nanorod dimers provide unique plasmonic hotspots with extremely large near-field enhancements in the gaps. Thereby they are beneficial in a wide range of applications, such as enhancing the emissions from ultra-weak emitters. For practical purposes, synthesis of gold nanorod dimers with high yield, especially on the substrates, is essential. Here, we demonstrate two controllable strategies to synthesize gold nanorod dimers based on the self-assembly of gold nanorods, either in bulk solution or on the surface of a glass substrate directly. Both methods can give a high yield of gold nanorod dimers, yet, assembling them directly on the substrate provides more flexibility in controlling the shape and size of each nanorod within the dimer.

4.1. Introduction

Plasmonic coupling between metallic nanoparticles can strengthen the near-field enhancement inside the interparticle gaps[1–10], as well as the local density of photon states[6, 11–15], compared to individual nanoparticles. As a consequence, metal nanoparticle aggregates can be applied to enhance ultra-weak signals, such as two-photon-excited (TPE) fluorescence[16]. These TPE fluorescence signals are normally too weak to be detected at single-molecule level, particularly when single nanoparticles are used. Nanoparticle dimers provide single plasmonic hotspots without reducing the overall fluorescence enhancements. Therefore nanoparticle dimer structures can be considered as the best plasmon-coupling systems for single-molecule fluorescence enhancement in the sense that, i) they provide single sites for fluorescence enhancements, and ii) the photoluminescence background from the nanoparticles can be reduced compared to multimer aggregates.

Among all the metal nanoparticles, chemically synthesised gold nanorods (GNRs) with elongated shape have proven to be the excellent building blocks for constructing plasmonic dimers. Compared to spherical nanoparticles, the anisotropy of the GNRs gives rise to much richer flexibility in tailoring the optical responses of the dimer structures. GNRs support two surface plasmon modes along their transversal and longitudinal axes[17, 18]. The longitudinal plasmon resonance can be tuned from visible to the near-infrared region by varying the aspect ratio[17, 19, 20]. While two GNRs are placed adjacent to each other, the plasmon resonance can be further adjusted by the interparticle gap and by the relative orientation[21–24]. End-to-end GNR dimers are of particular interest as they produce higher near-field enhancement than other configurations as a result of the stronger coupling between the longitudinal modes. Preparation of end-to-end GNR dimers with high yield, especially on the substrate, is therefore beneficial for various plasmon-mediated applications[24, 25]. With this aim, various approaches have been developed to link the GNRs in an end-to-end fashion.

DNA origami templates can be used to assemble individual GNRs into well-defined nanoarchitectures[22, 26–28], including the end-to-end dimer[29–31], yet this approach requires harsh treatments to both the GNR suspensions and the DNA templates. A more straightforward approach is to link GNRs directly in an end-to-end fashion through electrostactic attraction[32, 33] or through covalent binding via molecular linkers[34–36]. Chemically synthesised GNRs are highly anisotropic in surface reactivity due to their anisotropic crystal structures, hence allow site-specific functionalization on the surfaces. For cetyltrimethylammonium bromide (CTAB) stabilized GNRs, for instance, the tips are more accessible to dithiol groups as the results of smaller population of CTAB[37, 38], which thus can trigger the end-to-end self-assembly of GNRs in the suspension[17]. For most cases, the dithiol ligands can serve not only as linkers, but also as spacers that separate the GNRs. Hence, dithiol ligands with different molecular sizes can be used to control the interparticle gaps of GNR assemblies[34, 39–41]. Despite the facilitation of end-to-end connections, controlled synthesis of GNR dimers with high yield in bulk suspension remains challenging because lack controls to stop the dimers from randomly growing into chain-like morphologies in the suspensions[34–36, 39–43].

Here, we have applied two strategies to synthesize end-to-end GNR dimers with the aid of biotinylated streptavidin as molecular linkers. Firstly, we illustrate the assembly in a bulk

suspension of GNRs in the presence of the biotinylated streptavidin. The biotinylated streptavidin can bind specifically to the tips of the GNRs in the presence of the surfactant CTAB, hence ensuring the end-to-end assemblies of the GNRs. The assembly was monitored by recording the extinction spectra of the assembly suspension over time, and a drop of this suspension was later deposited and dried between two glass slides. Secondly, we performed the GNR dimer assembly directly on glass slides. We first immobilized single nanorods on a clean glass slide, and functionalized them with the biotinylated streptavidin specifically on the tips of the each GNR. The molecular linkers functionalized on the immobilized gold nanorods have the chance of adsorbing a second GNR in the solution, hence forming dimer structures. During the assembly, based on the bottom-up flipped strategy, we can separate the inevitable multimer aggregates in the suspensions. Thereby we can get purified end-to-end GNR dimer structures on glass.

4.2. Materials and Method

4.2.1. Materials

The following chemicals and materials were used for the synthesis of the GNR dimers: Unconjugated streptavidin (SNN1001, invitrogen), N-[6-(biotinamido)hexyl]-3'-(2'-pyridyldithio) propionamide (EZ-link HPDP-biotin; Pierce), tris(2-carboxyethyl)phosphine) (TCEP, Pierce), Cetyltrimethylammonium bromide (CTAB), CTAB-stabilized Gold nanorods with plasmon resonance of $700\ \mathrm{nm}$ (NA-40-700, OD-50, Nanoseedz), Glass slides (Menzel-Gläser, $\phi = 25\ \mathrm{mm}$).

4.2.2. Methods

Figure 4.1 schematically illustrates the two assembly strategies we applied for the synthesis of gold nanorod dimers: (a) assembly in solution, which we can call bulk-assembly process; and (b) step-wise assembly on the surface of the substrate. The processes can be briefly described as follows.

Preparation of the molecular linkers.
A biotin disulfide solution ($20\ \mu\mathrm{M}$), EZ-link HPDP-biotin, was pretreated with a reducing agent solution, TCEP (tris(2-carboxyethyl)phosphine), with a 1:10 biotin/TCEP ratio. This reaction was allowed at room temperature for $15\ \mathrm{min}$ to break the disulfide bonds in the HPDP-biotin molecules. This process can be verified by monitoring the extinction peak at $343\ \mathrm{nm}$ [44](see figure S4.1b in Supporting Information). The mixture solution was added to the streptavidin solution ($1\ \mu\mathrm{M}$) in phosphate-buffered saline solution (PBS, pH=7.4), with a ratio of 4:1 for biotin/streptavidin. The incubation lasted for $45\ \mathrm{min}$ to allow the binding of streptavidin with at least two biotins. The excess of unbound biotin disulfide and TCEP was removed by centrifugation in centrifugal filter devices (Ultra-0.5 10K, Amicon). The residue was dispersed in $100\ \mu\mathrm{L}$ deionized (DI) water.

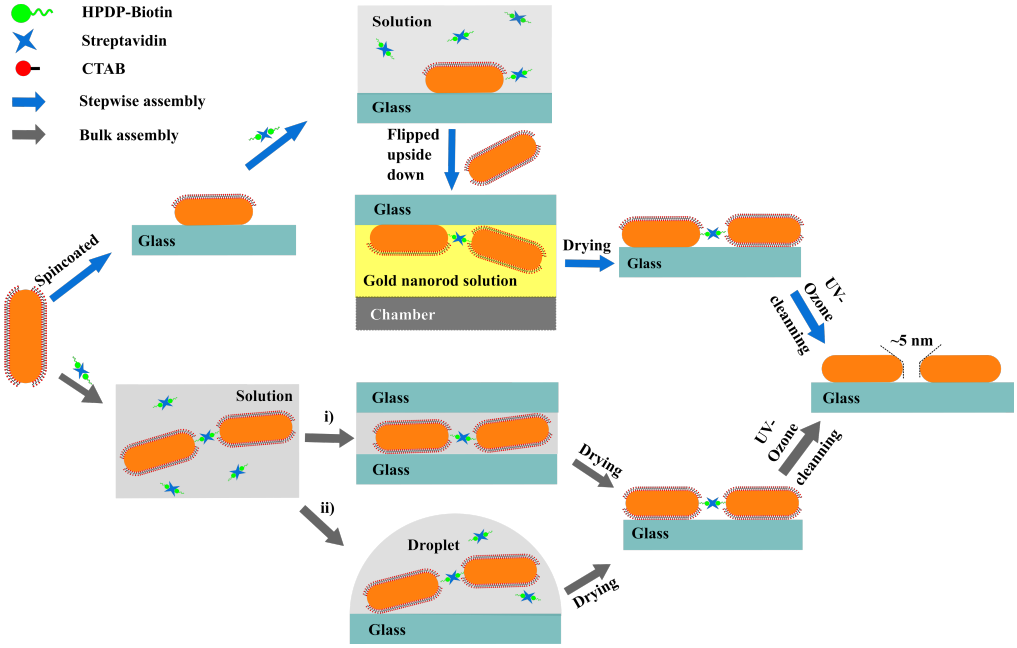

Figure 4.1: Assembly schemes for two synthesis approaches of gold nanorod dimers. Blue arrows illustrate the step-wise assembly approach where two GNRs of the dimer are immobilized sequentially on the glass surface, by spin-coating and by molecular linking, respectively. Grey arrows show the bulk-assembly approach.

(a) Step-wise assembly of GNRs on the glass surface.
Step 1. Immobilized GNRs on the glass side: Individual GNRs were immobilized onto a clean glass slide by spin-coating a suspension of CTAB-stabilized GNRs. These isolated GNRs can be viewed as the "first" GNRs of the dimers. After spin-coating, UV/Ozone cleaning was performed to remove the CTAB around GNRs' surfaces to ensure proper sticking of these GNRs on the glass surface. The slide was immersed in a CTAB solution ($1\ \mathrm{mM}$) for about $30\ \mathrm{min}$. This step created a bilayer of CTAB that covered the sides of the GNRs more compactly, leaving the tips exposed and accessible to the thiolated molecular linkers.
Step 2. Tip-specific functionalization of the GNRs: The CTAB solution was replaced with the pretreated biotinylated streptavidin solution ($\sim 200\ \mathrm{nM}$). In the presence of $\sim 1\ \mathrm{mM}$ CTAB, the thiolated linkers can bind specifically at the tip of the GNRs. The tip-specific binding reaction was allowed to proceed for $90\ \mathrm{min}$, and afterward the slide was cleaned gently with DI water to remove any reactant residues on the surface.
Step 3. Synthesis of GNR dimers on the glass surface: The glass slide was then flipped and immersed in GNR colloid in an upside-down manner for $12\ \mathrm{hours}$, with the surface containing tip-functionalized GNRs facing the bottom of the sample chamber (see the scheme in figure 4.1). This upside-down strategy can significantly reduce the deposition of GNR monomers or aggregated multimers onto the substrate under the influence of gravity. The thiol-functionalized GNRs on the glass slide provided binding sites for the GNRs, and had the chances to "adsorb" the second GNR to form a GNR dimer through gold-thiol bonds. This step-wise assembly approach allows us to construct high-purity gold nanorod dimers on the substrate, and provides the flexibility of adjusting the shapes or sizes of each particle in the dimers.

(b) Assembly of GNRs in bulk suspension.
The assembly of GNRs can also be performed in the bulk suspension. Briefly, a commercially available GNR suspension (NA-40-700, OD-50, Nanoseedz) was diluted to the concentration according to its optical density (OD) of ~ 0.3. The GNR suspension had plasmon absorption at $700\ \mathrm{nm}$, and the average diameter of the GNRs was $40\ \mathrm{nm}$. $40\ \mu\mathrm{L}$ of the pretreated biotin-streptavidin solution were added into $500\ \mu\mathrm{L}$ as-prepared GNR solution to trigger the end-to-end assembly of the GNRs. The assembly of GNRs was monitored by recording the extinction spectrum of the solution with a Cary 50 UV-Vis spectrometer (Varian Inc. Agilent Technology, USA) every $2\ \mathrm{min}$. After the extinction peak of the longitudinal plasmonic modes dropped by about $1/4$, the GNR assemblies can be immobilized onto the glass slides through the following two strategies:
i) Deposition of the GNR assemblies between two glass slides. A small amount of the GNR assembly solution ($\sim 10\ \mu\mathrm{L}$) was deposited onto a clean cover glass slide, and was immediately covered with a second glass slide. The capillary action between the two slides squeezed the assembled solution and formed a thin layer. This strategy helps stop further assembly of GNR, and deposit the GNR assemblies uniformly on the surfaces of the glass slides. After deposition, the two slides were separated by immersing them in clean water.
ii) Drop-coating deposition of the GNR assemblies. As a comparison, a traditional drop-coating approach of depositing the GNR assemblies was also examined in this study. Briefly, a small drop of GNR assembly solution was deposited on a clean glass slide, and blown dry gently with nitrogen gas.

Removing of the organic molecules around GNRs.
We performed UV/Ozone cleaning to remove all the organic molecules around the deposited GNRs to ensure the proper sticking of the GNRs on the glass surface, and to create free gaps between the GNRs of the assemblies.

4.3. Results and discussion

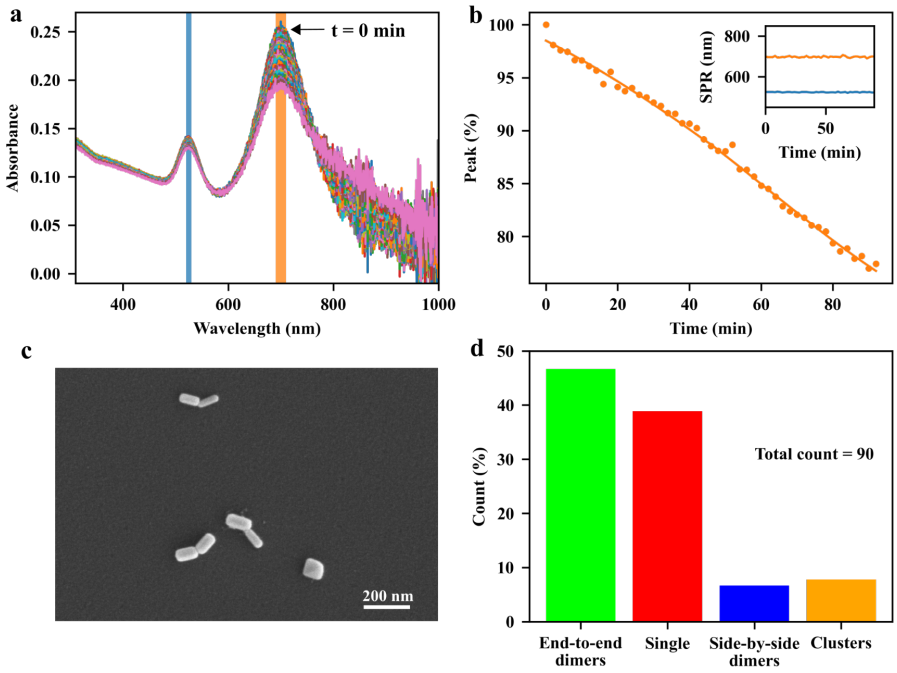

Figure 4.2: Bulk assembly experiment. (a) Spectral change during the assembly process. (b) Percentage decrease in the peak value of spectra as time progresses. The orange shaded area shown in (a) is used to calculate the normalized values. Inset: the resonance wavelenths of the transverse (blue) and longitudinal (orange) plasmon modes. (c) SEM image of typical gold nanorod dimers on glass slide deposited by using "two-slide" strategy. (d) The statistics percentages of end-to-end dimers (green), single GNRs (red), side-by-side dimers (blue), and clusters (orange). The statistics was done by counting 90 nanoparticles.

We begin our discussion with the assembly process of GNRs in the bulk suspension. As is well known, the formation of nanoparticle aggregates, or nanoparticle assemblies, can be characterized by the change of their plasmon resonances compared to single particles. The assembly process in bulk solution can be visualized by the evolution of the visible-near-infrared (vis-NIR) extinction spectra of the GNR suspension mixed with the linkers. Specifically, the elongated GNRs can be assembled side-by-side, end-to-side, or end-to-end, depending on the binding sites of the molecular linkers on the surface of each GNR. In the bulk-assembly experiments, the formation of these assemblies can be probed by monitoring the absorption bands corresponding to the transverse or longitudinal SPR of the GNRs: the

side-by-side and the end-to-side assemblies will induce a red-shift to the initial transverse SPR band of single GNRs, while the end-to-end assemblies will give rise to a red-shift of the longitudinal SPR band. The red-shifts of the plasmon modes depend on the sizes of the individual GNRs and on the gaps between them. Considering the interparticle gap of about $5\ \mathrm{nm}$, determined by the size of streptavidin[39], and the average sizes $40\ \mathrm{nm} \times 97\ \mathrm{nm}$ of the GNRs, we expect a red-shift of about $100\ \mathrm{nm}$ for the longitudinal SPR of the end-to-end and a red-shift of about $30\ \mathrm{nm}$ for the transverse SPR of the side-by-side dimer, compared to the modes of single GNRs (see figure S4.2 in Supporting Information).

Figure 4.2a shows the evolution of the vis-NIR extinction spectra of the GNR suspension after the addition of the pretreated dithiolated streptavidin-biotin compounds. The spectra were acquired every $2\ \mathrm{min}$ at room temperature. After adding the molecular linkers, the extinction peak, corresponding to longitudinal SPR band of isolated GNRs, decreases gradually in intensity without shift of its spectral position, while the red-side shoulder became broader, indicating the formation of the end-to-end assemblies of GNRs in the solution. After certain time, we observed a small tail at the longer-wavelength side of the longitudinal plasmon band, which could be assigned to the increased content of the end-to-end GNR chains over time. From the spectra, we conclude that the fraction of the longer chain assemblies (e.g. the assemblies with more than three GNRs) in the solution is low, as the extinction at the end of the longer-wavelength tail is relatively small compared to the extinction at the red-side shoulder at the wavelength of around $800\ \mathrm{nm}$ (which corresponds to the SPR of end-to-end dimer from simulations, see figure S4.2). The ratio of short-chain assemblies (e.g. GNR dimers) can be further controlled by adjusting the assembly time and the stoichiometric ratio between GNR and the molecular linker.

From figure 4.2a, we didn't observe any noticeable change in the shape of the transverse SPR band except for a reduction of the intensity, which indicated that the GNRs assembled in the side-by-side configuration were rare in the solution. Here, the facilitation of end-to-end GNR assembly can be attributed to the rigid structure of the streptavidin and of the streptavidin-biotin complexes. The relative large size of streptavidin makes it more difficult for the short thiol-end groups of the compounds to bind with the gold surfaces on the sides of the GNRs, which are coated with a CTAB layer, favoring the binding of the linkers to the GNR's tips, where the CTAB density is lower. We therefore propose that the pre-treatments of the molecular linkers mentioned earlier make them more robust to assemble the GNRs into end-to-end configurations. This statement can be confirmed by a control experiment, where we added the solutions of streptavidin, biotin and TCEP into the GNR suspension simultaneously to trigger the GNR assembly, instead of using the pre-treated solution that contained only the streptavidin-biotin compounds. Figure S4.3 shows the time-dependent extinction spectra of GNRs after the addition of the mixture of streptavidin, HPDP-biotin and TCEP, with the stoichiometric ratio of $1:4:8$. As shown in the plot, the transverse SPR band was red-shifted slightly as time evolved, accompanied by an increase of the extinction at the dip of the spectra between the two SPR peaks. Hence it was evident that the GNRs could also be assembled side-by-side in the presence of free thiolated biotin and unconjugated streptavidin. Additionally, the assembly rate was faster than the assembly process with only streptavidin-biotin compouds. More controlled experiments were performed using: i) biotin and TCEP, ii) streptavidin and TCEP and iii) streptavidin-biotin linker molecules. As is shown in figure 4.3, we see that biotin-only or streptavidin-only yields negligible spectral

change as time goes, compared to the case with streptavidin-biotin linker molecules.

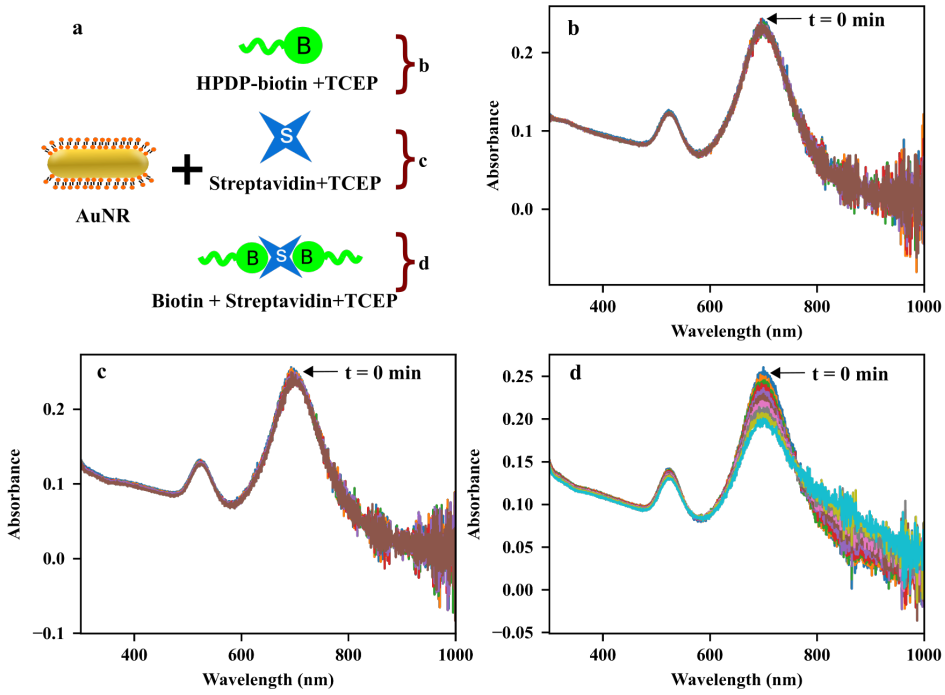

Figure 4.3: Control experiments: (a) Schematic showing the different linker molecules used for the experiment. (b, c d) Time evolution of the extinction spectra when the linker is only biotin and TCEP (b), only streptavidin and TCEP (c), and when the linker molecule is biotin-streptavidin and TCEP (d). The TCEP concentration for (b) and (c) was 100 μM. The spectra were acquired every 10 min for 2 hours.

The GNR assemblies were examined via SEM measurements after deposition onto a clean glass slide. We applied the two-slide-sandwich strategy mentioned in the method section to deposit the GNR assemblies onto the glass slides. Compared to other methods, such as the drop-coating or spin-coating deposition approaches, our strategy is very simple, yet, very effective in the distribution of the assemblies on the glass surface, and can maintain the configurations of the assemblies during the deposition process. A typical SEM image of GNR dimers with well-defined end-to-end configuration is shown in figures 4.2c. More images taken from the same sample (see figure S4.5, S4.6 and S4.7 in Supporting Information) indicate that our approaches are very efficient in preparing end-to-end GNR dimers in the substrate. As shown in figures 4.2d., we obtained a ratio of 47% for the end-to-end dimers from the total count of 90 particles. More comparisons of different deposition approaches can be found in the Supporting Information.

So far we have discussed the bulk assembly approach to synthesize the end-to-end GNR dimers in GNR suspension. Our result shows that suitable treatments of the thiolated streptavidin-biotin complex facilitate the assembly of the GNRs into end-to-end configurations, which had earlier been proved by K. K. Caswell et al.[39]. Yet assembly of GNRs in bulk sus-

pension normally ends up with long chains of GNRs, and the separation of the GNR dimers from the monomers and multimers could be an issue to prepare the sample with GNR dimers on the substrate with high yields.

Inspired by the extraordinarily high affinity of streptavidn for biotin and by the chemical stability of the complex, we developed a step-wise assembly approach to synthesize GNR dimers directly on a glass surface. Briefly, the first GNR of the dimer was first immobilized on the glass surface, and later combined with the second GNR through the thiol-gold bond with the aid of the thiolated streptavidin-biotin compound functionalized at the tip of the first GNR. Similar step-wise assembly approach had been reported to create gold nanoparticle dimer with high yield by using the alkanedithiol ($\mathrm{SH(CH_2)}n\mathrm{SH}$) or double-stranded DNA as the molecular linkers[45–48]. So far, however, this strategy has only be exploited to the assembly of spherical gold nanoparticles with small sizes ($\sim 20\ \mathrm{nm}$), and special functionalizations of the glass surface were needed. Here, we show that the step-wise assembly method can also be applied to fabricate GNR dimers on the substrate. By using the flipped upside-down strategy shown in figure 4.1, where the targeted GNRs were in the solution below the glass surface with tip-functionalized GNRs, we can prevent precipitation of the monomers or sedimentation of the inevitable aggregated multimers on the substrate, hence seletively bind dimer structures onto the glass surface.

Figure 4.4 shows a representative SEM image of the GNR dimers assembled using the step-wise upside-down approach. As shown in the SEM image, we got 8 GNR dimers with end-to-end configurations (noted with the green dashed circles) out of the 15 nanoparticles in the area. Meanwhile, we also see 3 particles with GNRs aggregated in the side-by-side configurations. Interestingly, we don't see any end-to-end assemblies in this area with more than three GNRs in the arrangement, which confirms that our method is effective in the fabrication of end-to-end GNR assemblies of short chains (in principle 3 GNRs at most).

Several factors could affect the efficiency of the fabrication of end-to-end dimers on the substrate by using our step-wise upside-down strategy: i) the number of the active binding sites for the targeted GNRs at the tips of the individual GNRs on the glass; ii) the denaturation of the dithiolated streptavidin-biotin complex during the assembly process; iii) the surface conditions of the glass, such as the surface roughness or the surface charge of the glass, which may influence the sticking of the second GNRs on the glass surface; iv) after taking away the glass from the GNR suspension after the assembly, there might also be some GNR suspension left on the glass surface, which might stick on the glass or even aggregate into clusters during the drying process.

We examined the SEM images in 12 different areas recorded on three different samples (including the area shown in figure 4.4) using the same method of step-wise assembly. Shown in figure S4.8 and figure S4.9, we see that the ratios of end-to-end GNR dimers can be very different in different areas. The non-uniform distribution of GNR dimers on the glass surface might be due to the non-uniform surface conditions of the glasses, which might affect the tip functionalization of each GNR, or might affect the binding efficiency of the linker with the second GNR. The random distribution of the GNR residues on the glass surface after the assembly might also affect the ratio of GNR dimer in different areas, as they will add more single GNRs on the surface. Nonetheless, we got a total of 50 end-to-end GNR dimers out of the 140 particles in all areas, which yields a ratio of 36% for end-to-end GNR dimers, as can be seen in figure 4.5 (green bar).

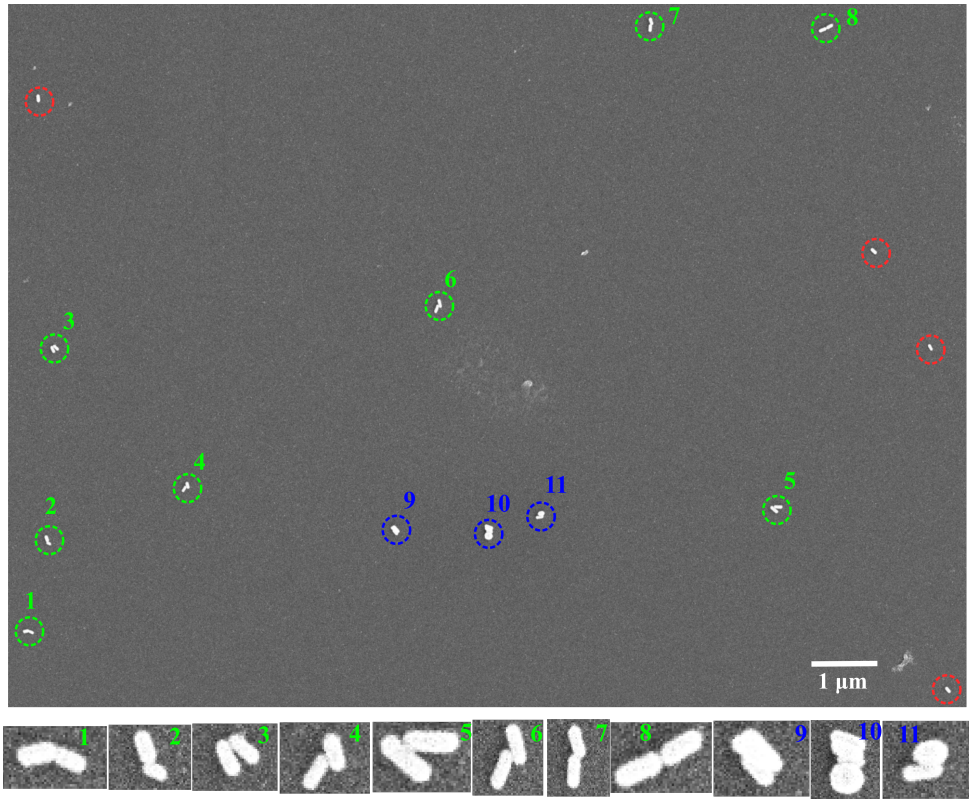

Figure 4.4: SEM image of the assembly sample prepared by using the step-wise assembly method. We see a total of 8 end-to-end GNR dimers out of 15 nanoparticles (green dashed circles) in this area. The blue and red circles represent the side-by-side assemblies and single GNRs, respectively. Below shows the zoomed in configurations of the assemblies.

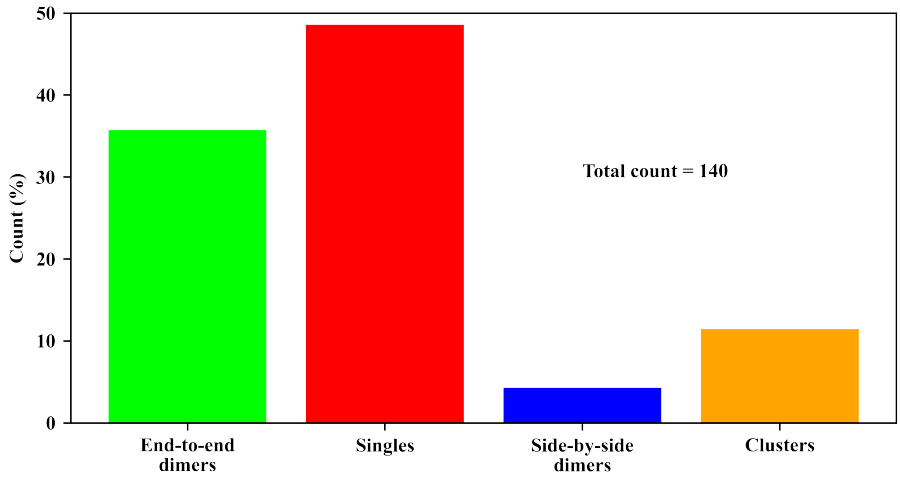

Figure 4.5: Yields of the nanoparticles with different configurations. The statistics was done by counting 140 nanoparticles from different areas of three samples, all of which were prepared by using the step-wise assembly approach.

4.4. Conclusions

In conclusion, we have demonstrated two different approaches for the fabrication of end-to-end GNR dimers based on the self-assembly of GNRs. Our results showed that pre-conjugation of streptavidin with thiolated-biotin as molecular linkers will facilitate GNR assembly into end-to-end dimers in the suspension. In this work, we illustrated a simple but very efficient way of depositing the GNR assemblies onto glass slide by sandwiching a small amount of GNR assembly between two glass slides. This approach helps us to deposit the GNR assemblies uniformly onto the glass slides, and maintain the configurations of the GNR assemblies during the deposition process.

We further developed a step-wise assembly method to synthesize GNR dimers directly on the glass. In this method, the two GNRs of the dimer were immobilized sequentially on the glass surface. Briefly, the first GNR of the dimer was immobilized by spin-coating, and adsorbed the second GNR in the suspension with the aid of the molecular linker. By applying a simple upside-down flipping strategy, where the targeted GNRs were in the solution below the glass surface with tip-functionalized GNRs, we ended up with a high yield of end-to-end GNR dimers. Our step-wise assembly method can be readily applied to different nanoparticles, providing the flexibility of controlling the shapes, sizes or materials of each nanoparticle in the assembly.

S4.1. Supporting information

GNR assembly in bulk suspension.

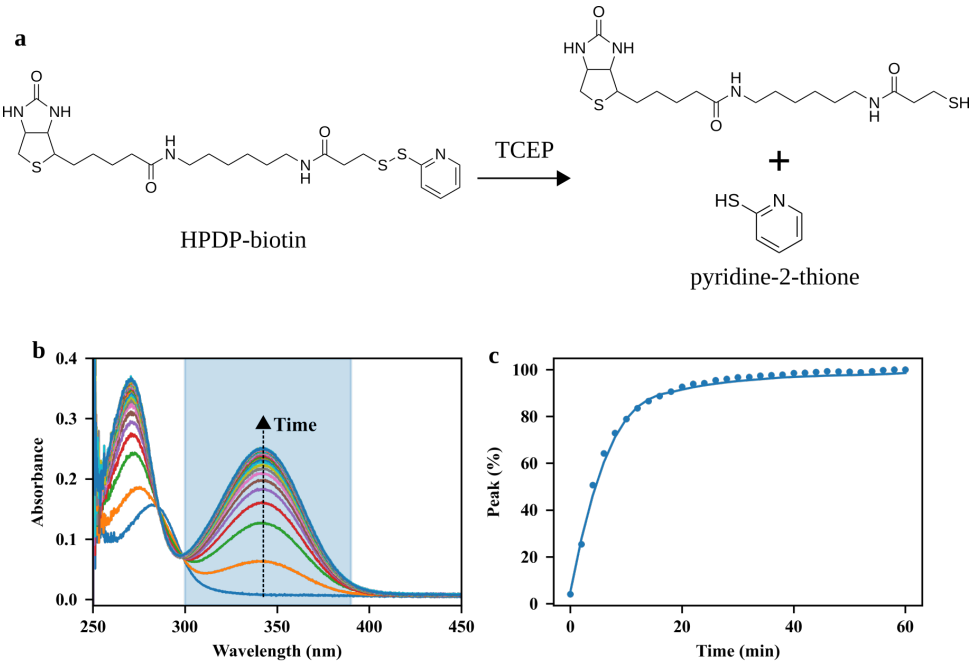

Figure S4.1: (a) Cleavage of the disulfide bond in HPDP-biotin molecule by the reducing agent TCEP. (b) Spectral evolution for HPDP-biotin at the concentration of 40 μM after the addition of 40 μM TCEP. The disulfide-bond cleavage of HPDP-biotin molecules is verified by monitoring the release of pyridine-2-thione, which has a maximum absorption at 343 nm. The spectra were acquired every 2 min. (b) Time evolution for the percentage of the peak at 343 nm.

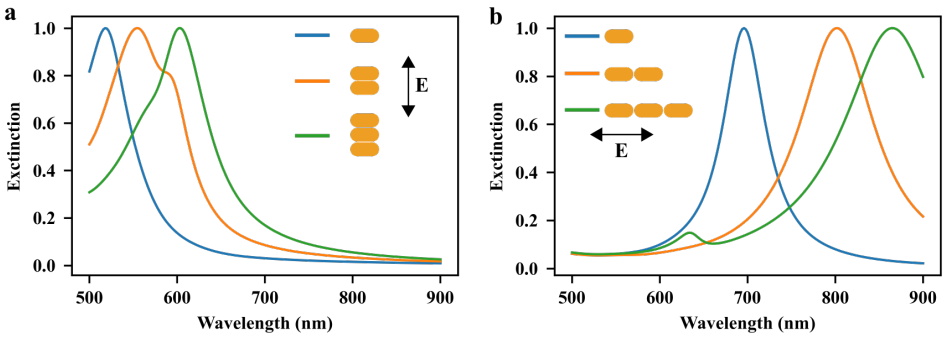

Figure S4.2: Simulated extinction spectra for GNR of different morphologies. (a) The extinction spectra excited transversely for a single GNR (blue), a side-by-side GNR dimer (orange), and a side-by-side trimer(green). (b) The extinction spectra excited longitudinally for a single GNR (blue), a end-to-end GNR dimer (orange), and a end-to-end trimer(green). Each GNR was modeled as a spherically capped clinder with the shape of $40\,\mathrm{nm} \times 97\,\mathrm{nm}$. The interparticle gap was set as $5\,\mathrm{nm}$. The simulations were performed by using boundary element method[49, 50].The dielectric permitivity for gold was taken from Johnson and Christy[51], and the refractive index of ambient medium was taken as 1.33.

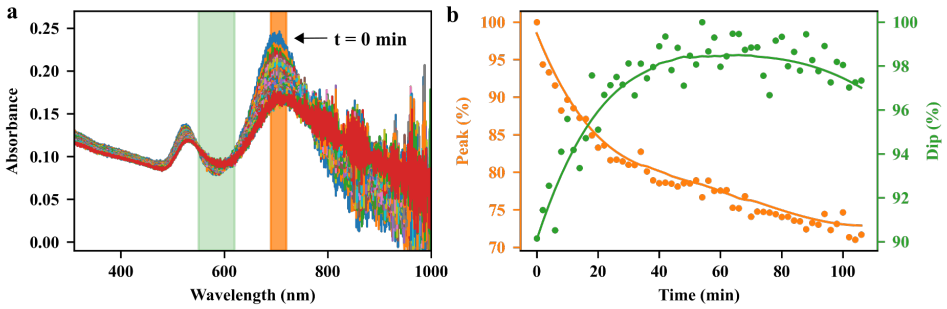

Figure S4.3: (a) Spectral evolution for GNRs in the presence of the HPDP-biotin, streptavidn, and TCEP. The assembly was triggered by adding the mixture without centrifugal filtering. (b) Time evolution of the pectcentage of the longitudinal plasmon peaks (orange line with dots), and the pectcentage of the dips (green line with dots) in the special window indicated by the green shadow in (a). The spectra were acquired every $2\,\mathrm{min}$.

Drop-coating deposition of the GNR assemblies

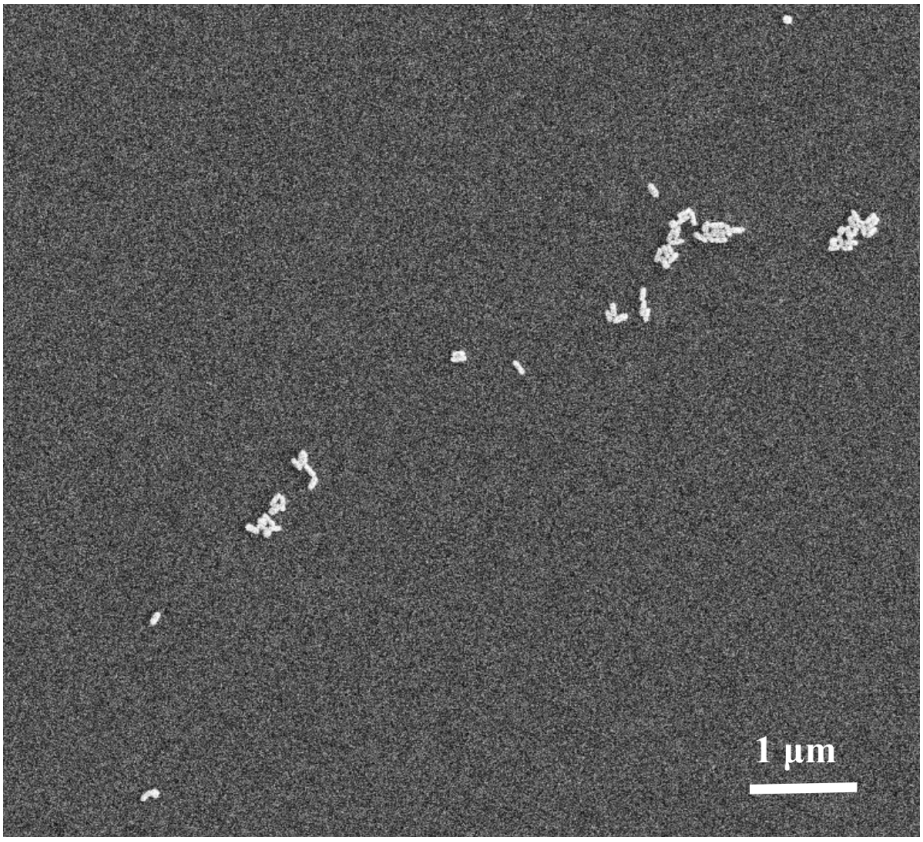

Figure S4.4: SEM images of GNR assemblies on a glass slide. The assembly was triggered by adding the dithiolated streptavidin-biotin compounds to the GNR suspension. The assemblies were deposited onto the glass slide by drop-coasting.

Deposition of the GNR assemblies between two cover slides

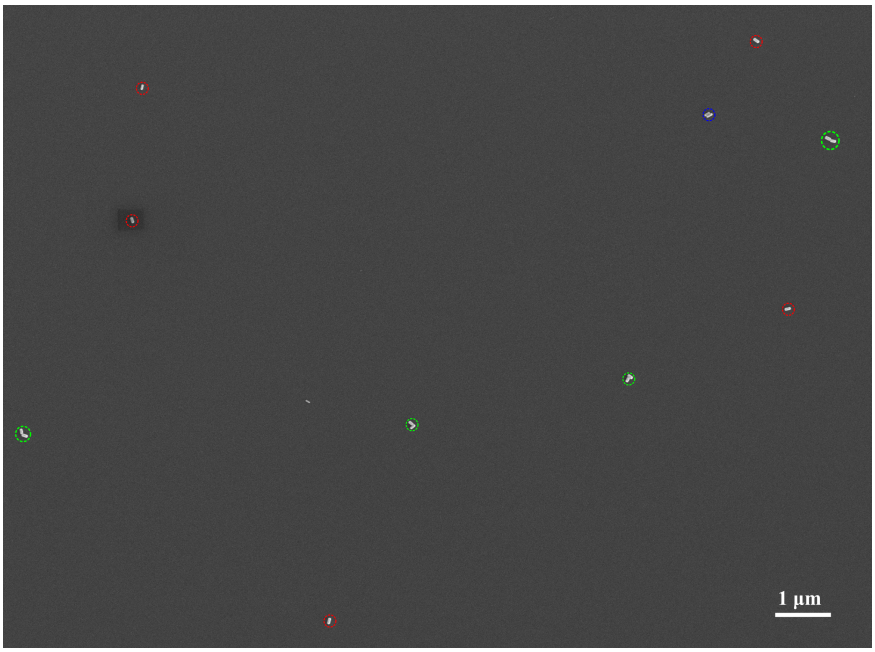

Figure S4.5: SEM images of GNR assemblies on a glass slide. The assembly was triggered by adding the dithiolated streptavidin-biotin compounds to the GNR suspension. The assemblies were deposited onto the glass slides and dried between two cover slides. The assemblies of different morphologies are highlighted by the colored circles: end-to-end GNR-dimer: green, single GNR: red, side-by-side GNR dimer: blue, and clusters: orange.

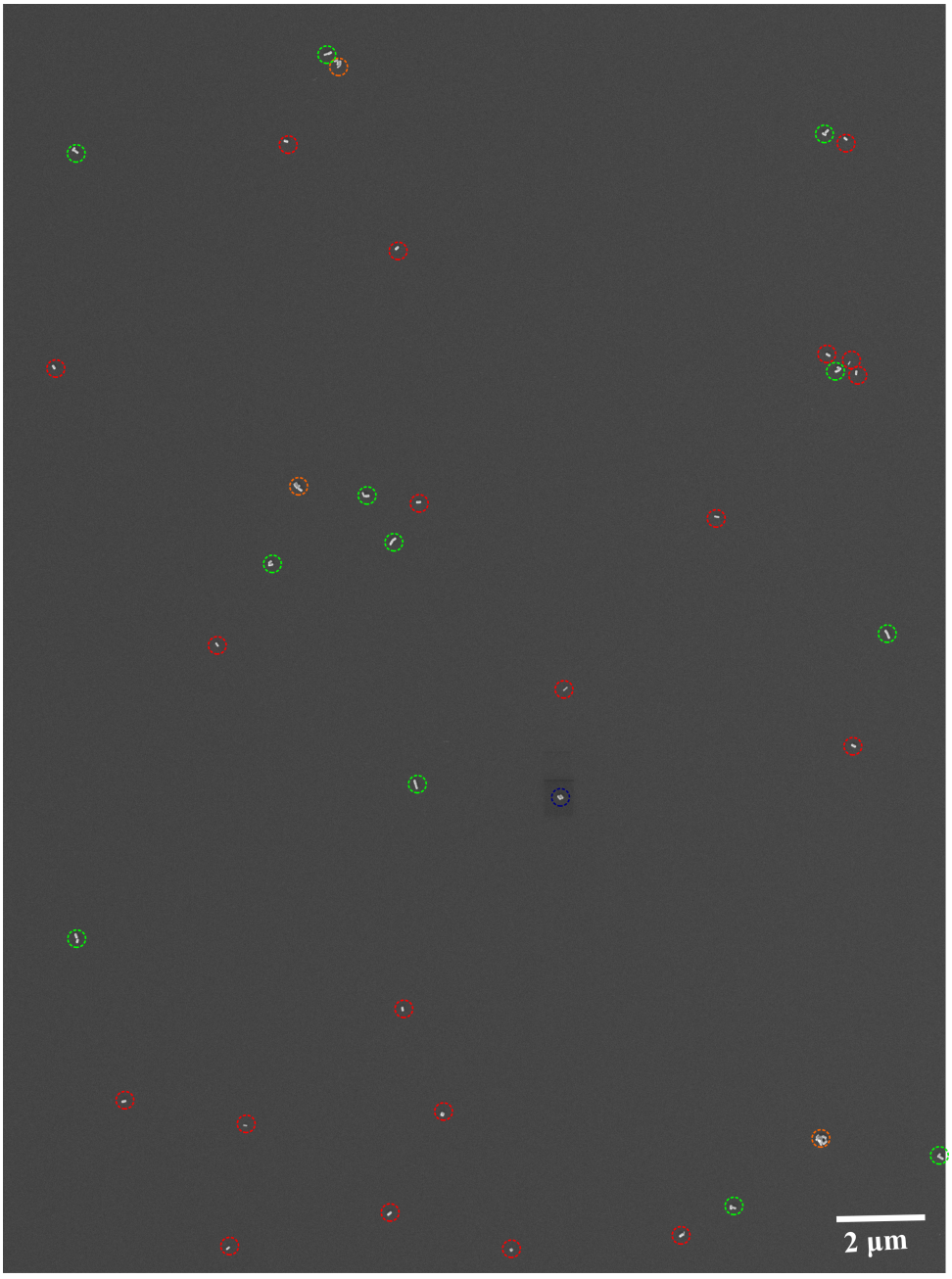

Figure S4.6: SEM images of GNR assemblies on the same glass slide as figure S4.5. The assemblies of different morphologies are highlighted by the colored circles: end-to-end GNR-dimer: green, single GNR: red, side-by-side GNR dimer: blue, and clusters: orange.

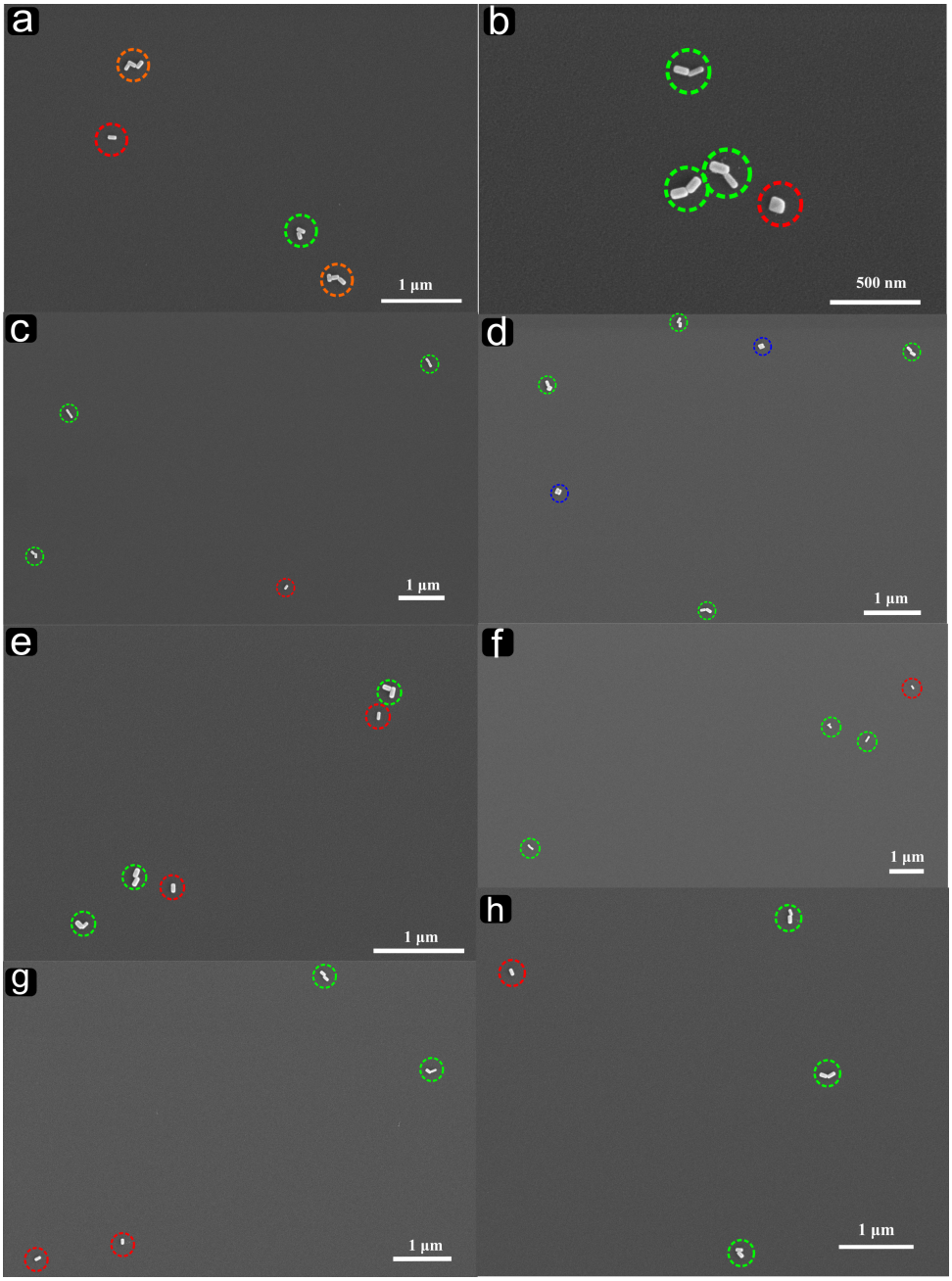

Figure S4.7: SEM images of GNR assemblies on the same glass slide as figure S4.5. (a-h) These SEM images are of different areas from the same sample. The assemblies of different morphologies are highlighted by the colored circles: end-to-end GNR-dimer: green, single GNR: red, side-by-side GNR dimer: blue, and clusters: orange.

Step-wise assembly of GNRs on the glass surface.

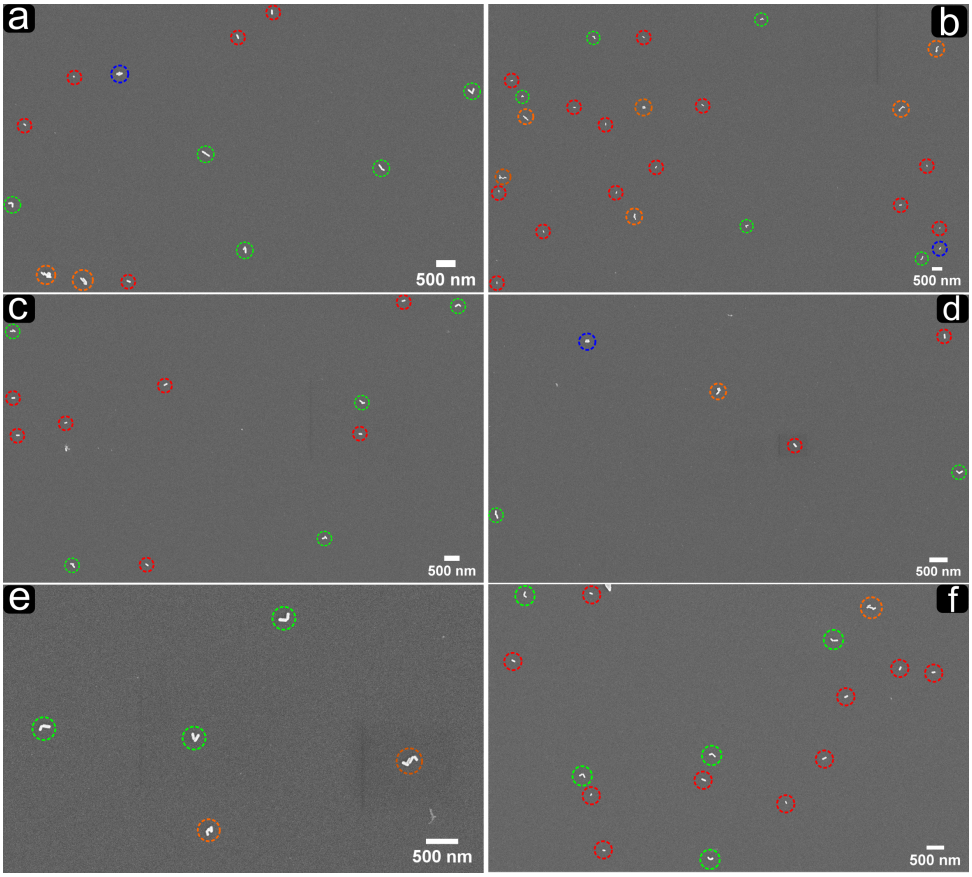

Figure S4.8: SEM images of GNR assemblies on a glass slide. The sample was prepared using the step-wise assembly method. (a-f) These SEM images are of different areas from the same sample. The assemblies of different morphologies are highlighted by the colored circles: end-to-end GNR-dimer: green, single GNR: red, side-by-side GNR dimer: blue, and clusters: orange.

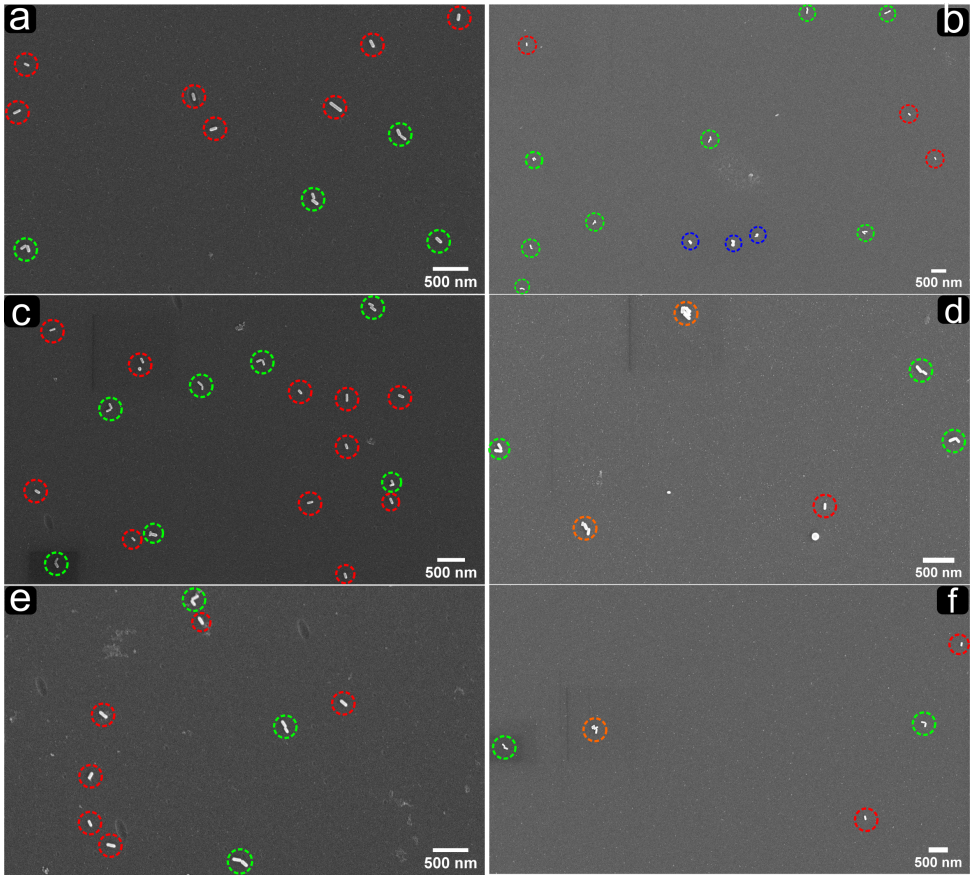

Figure S4.9: SEM images from two different samples prepared by using the step-wise assembly method. (a, c, e) Assemblies of different areas from the first sample. (b, d, f) SEM images from the second sample. The assemblies of different morphologies are highlighted by the colored circles: end-to-end GNR-dimer: green, single GNR: red, side-by-side GNR dimer: blue, and clusters: orange.

References

[1] H. Xu, J. Aizpurua, M. Käll, and P. Apell, *Electromagnetic contributions to single-molecule sensitivity in surface-enhanced Raman scattering,* Physical Review E **62**, 4318 (2000).

[2] A. Kinkhabwala, Z. Yu, S. Fan, Y. Avlasevich, K. Müllen, and W. E. Moerner, *Large single-molecule fluorescence enhancements produced by a bowtie nanoantenna,* Nature Photonics **3**, 654 (2009).

[3] T. Kang, S. Hong, Y. Choi, and L. P. Lee, *The Effect of Thermal Gradients in SERS Spectroscopy,* Small **6**, 2649 (2010).

[4] J. C. Fraire, L. A. Pérez, and E. A. Coronado, *Rational Design of Plasmonic Nanostructures for Biomolecular Detection: Interplay between Theory and Experiments,* ACS Nano **6**, 3441 (2012).

[5] X. Lan, Z. Chen, X. Lu, G. Dai, W. Ni, and Q. Wang, *DNA-Directed Gold Nanodimers with Tailored Ensemble Surface-Enhanced Raman Scattering Properties,* ACS Applied Materials & Interfaces **5**, 10423 (2013).

[6] P. M. R. Paulo, D. Botequim, A. Jóskowiak, S. Martins, D. M. F. Prazeres, P. Zijlstra, and S. M. B. Costa, *Enhanced Fluorescence of a Dye on DNA-Assembled Gold Nanodimers Discriminated by Lifetime Correlation Spectroscopy,* The Journal of Physical Chemistry C **122**, 10971 (2018).

[7] L. Tie, M. Focsan, J. Bosson, C. Tira, A. Campu, A. Vulpoi, and S. Astilean, *Controlling the end-to-end assembly of gold nanorods to enhance the plasmonic response in near infrared,* **6**, 095038 (2019).

[8] J. Langer, L. M. Liz-Marzán, *et al.*, *Present and Future of Surface-Enhanced Raman Scattering,* ACS Nano **14**, 28 (2020).

[9] M. Blanco-Formoso, N. Pazos-Perez, and R. A. Alvarez-Puebla, *Fabrication and SERS properties of complex and organized nanoparticle plasmonic clusters stable in solution,* Nanoscale **12**, 14948 (2020).

[10] J. Zheng, X. Cheng, H. Zhang, X. Bai, R. Ai, L. Shao, and J. Wang, *Gold Nanorods: The Most Versatile Plasmonic Nanoparticles,* Chemical Reviews (2021), 10.1021/acs.chemrev.1c00422.

[11] M. Ringler, A. Schwemer, M. Wunderlich, A. Nichtl, K. Kürzinger, T. A. Klar, and J. Feldmann, *Shaping Emission Spectra of Fluorescent Molecules with Single Plasmonic Nanoresonators,* Physical Review Letters **100**, 203002 (2008).

[12] M. P. Busson, B. Rolly, B. Stout, N. Bonod, and S. Bidault, *Accelerated single photon emission from dye molecule-driven nanoantennas assembled on DNA,* Nature Communications **3**, 962 (2012).

[13] Z. Zhang, P. Yang, H. Xu, and H. Zheng, *Surface enhanced fluorescence and Raman scattering by gold nanoparticle dimers and trimers,* Journal of Applied Physics **113**, 033102 (2013).

[14] A. Szenes, B. Bánhelyi, T. Csendes, G. Szabó, and M. Csete, *Enhancing Diamond Fluorescence via Optimized Nanorod Dimer Configurations,* Plasmonics **13**, 1977 (2018).

[15] I. Kaminska, J. Bohlen, S. Mackowski, P. Tinnefeld, and G. P. Acuna, *Strong Plasmonic Enhancement of a Single Peridinin–Chlorophyll a–Protein Complex on DNA Origami-Based Optical Antennas,* ACS Nano **12**, 1650 (2018).

[16] O. S. Ojambati, R. Chikkaraddy, W. M. Deacon, J. Huang, D. Wright, and J. J. Baumberg, *Efficient Generation of Two-Photon Excited Phosphorescence from Molecules in Plasmonic Nanocavities,* Nano Letters **20**, 4653 (2020).

[17] H. Chen, L. Shao, Q. Li, and J. Wang, *Gold nanorods and their plasmonic properties,* Chemical Society Reviews **42**, 2679 (2013).

[18] P. Zijlstra, P. M. R. Paulo, and M. Orrit, *Optical detection of single non-absorbing molecules using the surface plasmon resonance of a gold nanorod,* Nature Nanotechnology **7**, 379 (2012).

[19] W. Ni, X. Kou, Z. Yang, and J. Wang, *Tailoring Longitudinal Surface Plasmon Wavelengths, Scattering and Absorption Cross Sections of Gold Nanorods,* ACS Nano **2**, 677 (2008).

[20] S. E. Lohse and C. J. Murphy, *The Quest for Shape Control: A History of Gold Nanorod Synthesis,* Chemistry of Materials **25**, 1250 (2013).

[21] A. M. Funston, C. Novo, T. J. Davis, and P. Mulvaney, *Plasmon Coupling of Gold Nanorods at Short Distances and in Different Geometries,* Nano Letters **9**, 1651 (2009).

[22] X. Lan, Z. Chen, G. Dai, X. Lu, W. Ni, and Q. Wang, *Bifacial DNA Origami-Directed Discrete, Three-Dimensional, Anisotropic Plasmonic Nanoarchitectures with Tailored Optical Chirality,* Journal of the American Chemical Society **135**, 11441 (2013).

[23] X. Lu, J. Wu, Q. Zhu, J. Zhao, Q. Wang, L. Zhan, and W. Ni, *Circular dichroism from single plasmonic nanostructures with extrinsic chirality,* Nanoscale **6**, 14244 (2014).

[24] M. A. Beuwer and P. Zijlstra, *Correlative microscopy of single self-assembled nanorod dimers for refractometric sensing,* The Journal of Chemical Physics **155**, 044701 (2021).

[25] C. Li, S. Li, A. Qu, H. Kuang, L. Xu, and C. Xu, *Directing Arrowhead Nanorod Dimers for MicroRNA In Situ Raman Detection in Living Cells,* Advanced Functional Materials **30**, 2001451 (2020).

[26] X. Lan, X. Lu, C. Shen, Y. Ke, W. Ni, and Q. Wang, *Au Nanorod Helical Superstructures with Designed Chirality,* Journal of the American Chemical Society **137**, 457 (2015).

[27] P. Zhan, P. K. Dutta, P. Wang, G. Song, M. Dai, S.-X. Zhao, Z.-G. Wang, P. Yin, W. Zhang, B. Ding, and Y. Ke, *Reconfigurable Three-Dimensional Gold Nanorod Plasmonic Nanostructures Organized on DNA Origami Tripod,* ACS Nano **11**, 1172 (2017).

[28] X. Lan, T. Liu, Z. Wang, A. O. Govorov, H. Yan, and Y. Liu, *DNA-Guided Plasmonic Helix with Switchable Chirality,* Journal of the American Chemical Society **140**, 11763 (2018).

[29] Y. Liu, Y. Liu, and Y. Shen, *Nano-assembly and welding of gold nanorods based on DNA origami and plasmon-induced laser irradiation,* International Journal of Intelligent Robotics and Applications **2**, 445 (2018).

[30] L. A. McCarthy, K. W. Smith, X. Lan, S. A. H. Jebeli, L. Bursi, A. Alabastri, W.-S. Chang, P. Nordlander, and S. Link, *Polarized evanescent waves reveal trochoidal dichroism,* Proceedings of the National Academy of Sciences **117**, 16143 (2020).

[31] Z. Zhao, X. Chen, J. Zuo, A. Basiri, S. Choi, Y. Yao, Y. Liu, and C. Wang, *Deterministic assembly of single emitters in sub-5 nanometer optical cavity formed by gold nanorod dimers on three-dimensional DNA origami,* Nano Research (2021), 10.1007/s12274-021-3661-z.

[32] S. M. H. Abtahi, N. D. Burrows, F. A. Idesis, C. J. Murphy, N. B. Saleh, and P. J. Vikesland, *Sulfate-Mediated End-to-End Assembly of Gold Nanorods,* Langmuir **33**, 1486 (2017).

[33] A. Kar, V. Thambi, D. Paital, G. Joshi, and S. Khatua, *Synthesis of Solution-Stable End-to-End Linked Gold Nanorod Dimers via pH-Dependent Surface Reconfiguration,* Langmuir **36**, 9894 (2020).

[34] P. K. Sudeep, S. T. S. Joseph, and K. G. Thomas, *Selective Detection of Cysteine and Glutathione Using Gold Nanorods,* Journal of the American Chemical Society **127**, 6516 (2005).

[35] Z. Sun, W. Ni, Z. Yang, X. Kou, L. Li, and J. Wang, *pH-Controlled Reversible Assembly and Disassembly of Gold Nanorods,* Small **4**, 1287 (2008).

[36] W. Ni, R. A. Mosquera, J. Pérez-Juste, and L. M. Liz-Marzán, *Evidence for Hydrogen-Bonding-Directed Assembly of Gold Nanorods in Aqueous Solution,* The Journal of Physical Chemistry Letters **1**, 1181 (2010).

[37] P. Zijlstra, P. M. R. Paulo, K. Yu, Q.-H. Xu, and M. Orrit, *Chemical Interface Damping in Single Gold Nanorods and Its Near Elimination by Tip-Specific Functionalization,* Angewandte Chemie International Edition **51**, 8352 (2012).

[38] P. M. R. Paulo, P. Zijlstra, M. Orrit, E. Garcia-Fernandez, T. C. S. Pace, A. S. Viana, and S. M. B. Costa, *Tip-Specific Functionalization of Gold Nanorods for Plasmonic Biosensing: Effect of Linker Chain Length,* Langmuir **33**, 6503 (2017).

[39] K. K. Caswell, J. N. Wilson, U. H. F. Bunz, and C. J. Murphy, *Preferential End-to-End Assembly of Gold Nanorods by Biotin-Streptavidin Connectors,* Journal of the American Chemical Society **125**, 13914 (2003).

[40] J. Liu, C. Kan, Y. Li, H. Xu, Y. Ni, and D. Shi, *End-to-end and side-by-side assemblies of gold nanorods induced by dithiol poly(ethylene glycol),* Applied Physics Letters **104**, 253105 (2014).

[41] Y. Xu, X. Wang, and X. Ma, *Efficient end-to-end assembly of gold nanorods via cyclodextrin-bisphenol A based supramolecular linker,* Dyes and Pigments **144**, 168 (2017).

[42] Y. Zhu, H. Kuang, L. Xu, W. Ma, C. Peng, Y. Hua, L. Wang, and C. Xu, *Gold nanorod assembly based approach to toxin detection by SERS,* Journal of Materials Chemistry **22**, 2387 (2012).

[43] A. F. Stewart, A. Lee, A. Ahmed, S. Ip, E. Kumacheva, and G. C. Walker, *Rational Design for the Controlled Aggregation of Gold Nanorods via Phospholipid Encapsulation for Enhanced Raman Scattering,* ACS Nano **8**, 5462 (2014).

[44] H. Chen, H. Zou, H. J. Paholak, M. Ito, W. Qian, Y. Che, and D. Sun, *Thiol-reactive amphiphilic block copolymer for coating gold nanoparticles with neutral and functionable surfaces,* Polymer Chemistry **5**, 2768 (2014).

[45] H. Cha, J. H. Yoon, and S. Yoon, *Probing Quantum Plasmon Coupling Using Gold Nanoparticle Dimers with Tunable Interparticle Distances Down to the Subnanometer Range,* ACS Nano **8**, 8554 (2014).

[46] D. Lee and S. Yoon, *Gold Nanocube–Nanosphere Dimers: Preparation, Plasmon Coupling, and Surface-Enhanced Raman Scattering,* The Journal of Physical Chemistry C **119**, 7873 (2015).

[47] H. Cha, D. Lee, J. H. Yoon, and S. Yoon, *Plasmon coupling between silver nanoparticles: Transition from the classical to the quantum regime,* Journal of Colloid and Interface Science **464**, 18 (2016).

[48] J. Li, T.-S. Deng, X. Liu, J. A. Dolan, N. F. Scherer, and P. F. Nealey, *Hierarchical Assembly of Plasmonic Nanoparticle Heterodimer Arrays with Tunable Sub-5 nm Nanogaps,* Nano Letters **19**, 4314 (2019).

[49] M. T. Homer Reid and S. G. Johnson, *Efficient Computation of Power, Force, and Torque in BEM Scattering Calculations,* ArXiv e-prints (2013), arXiv:1307.2966 [physics.comp-ph] .

[50] `http://github.com/homerreid/scuff-EM`.

[51] P. B. Johnson and R. W. Christy, *Optical Constants of the Noble Metals,* Physical Review B **6**, 4370 (1972).

5

Two-photon-excited single-molecule fluorescence enhanced by gold nanorod dimers

In this chapter, we demonstrate for the first time two-photon-excited single-molecule fluorescence enhancement by end-to-end self-assembled gold nanorods dimers. We developed a controllable method to create end-to-end gold nanorod dimer structures based on the specific molecular recognition of biotin and streptavidin. The typical size of streptavidin of around $5\ \mathrm{nm}$ *separates the gold nanorods with gaps suitable for the access of fresh dyes in aqueous solution, yet give very high two-photon fluorescence enhancement. Simulations show that enhancements of more than seven orders of magnitude can be achieved for two-photon-excited fluorescence in the plasmonic hotspots. With such high enhancements, we successfully detect two-photon-excited fluorescence for a common organic dye (ATTO 610) at the single-molecule level.*

5.1. Introduction

Two-photon-excited fluorescence is a nonlinear optical process, where a fluorophore simultaneously absorbs two photons of identical frequency, leading to the emission of a photon with higher energy[1, 2]. Ever since its first prediction by Maria Goeppert-Mayer in 1931[3], and its experimental demonstration by Frank et al in the 1960s[4, 5], two-photon excitation has attracted significant interest for several advantages, such as strong background suppression[1], deeper tissue penetration[6, 7], less photodamage to the samples[8, 9], and intrinsic optical sectioning[10–12]. Practical applications of two-photon excitation, however, are limited by the requirement of extremely high photon density. The invention of ultrashort-pulse lasers, has led to a rapid growth of two-photon-based techniques in various scientific fields[10], such as imaging[6, 7, 10–12], microfabrication[13–17] or optical storage[18–21].

Recent progress in nano-optics has made it possible to enhance the two-photon excitation process through near-field confinement by plasmonic nanostructures[22, 23]. The local electromagnetic field around the plasmonic structures can be enhanced by one or more orders of magnitude, depending on their shapes, sizes and the materials. Among all kinds of plasmonic structures, wet-chemically synthesized gold nanorods have been widely exploited in the context of field-enhanced spectroscopy for their facile synthesis and narrow tunable plasmon resonances[24, 25]. In the past few years, gold nanorods have been applied to enhance the fluorescence of single weak emitters[26–29]. Fluorescence enhancements by $3 \sim 4$ orders of magnitude have been reported with single nanorods (GNRs) of suitable plasmon resonances, through enhancement of both the excitation and radiative rates of the emitters[26–29]. Higher enhancement factors of about $10^5 \sim 10^6$ have also been achieved in strongly coupled gold nanosphere dimers[30].

Fluorescence upon two-photon excitation is expected to give rise to much larger enhancement than one-photon excited fluorescence due to the quadratic dependence of this process on the excitation intensity[31–35]. The effective enhancing volume under two-photon excitation is restricted to much smaller regions, which improves the sensitivity of detecting the enhanced two-photon-excited fluorescence signals. Single-molecule or single-particle detection of two-photon-excited fluorescence opens up the door to reveal the intrinsic nature of nonlinear interaction between photons and molecules[36], which usually hidden in ensemble experiments. By using a single GNR, we have earlier reported strong two-photon-excited photoluminescence enhancement of single colloidal quantum dots (Qdots), with enhancement factors larger than 10,000-fold[34]. Such high enhancement, however, is still not enough to distinguish the enhanced two-photon-excited fluorescence of single organic molecules from background molecules, which usually have much lower two-photon absorption cross-section than Qdots (about 1000 times smaller). A few other plasmonic structures, such as nanofabricated bow-tie antennas[33], have also been reported to give two-photon enhancement, yet the enhancement factors were even lower than those of GNRs. Oluwafemi et al. have recently demonstrated that two-photon absorption of Rubpy molecules can be enhanced by 10^8 inside the nanoparticle-on-mirror (NPoM) sub-nm cavities[35]. Despite the extremely large enhancement factor, in order to enhance single-molecule two-photon-excited fluorescence, the NPoM structures are limited by i) the requirement of large illumination angles to efficiently excite the cavity modes; ii) photobleaching of the molecules,

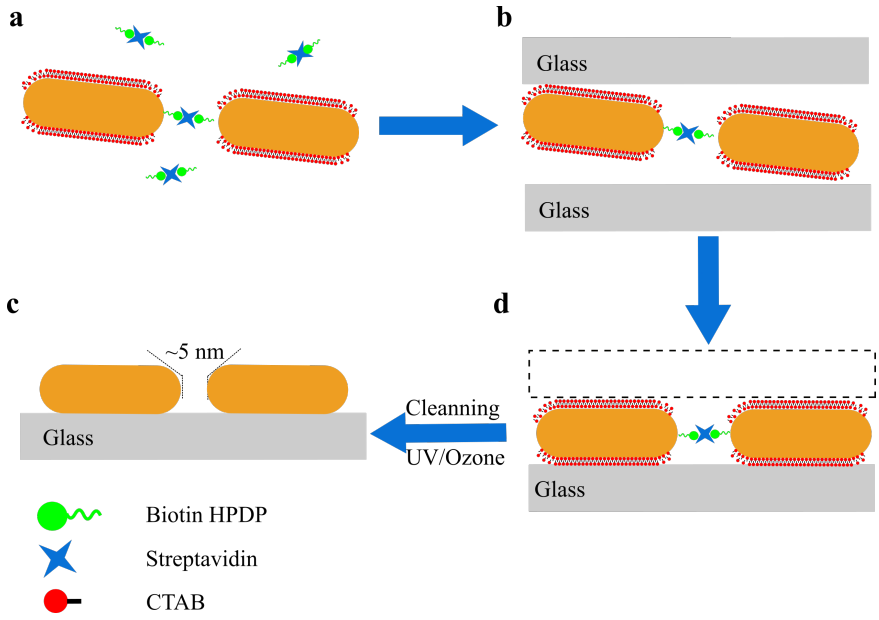

Figure 5.1: Scheme for end-to-end assembly of gold nanorod dimers. (a) Pretreated molecular linkers based on biotin disulfides-streptavidin biomolecular pairs were added to the GNRs solution to trigger the end-to-end assembly of GNRs. (b,d) The assembled GNR dimers were deposited onto a clean glass, which was covered by other glass sides to stop the assembling of GNRs. (c) UV/Ozone cleanning was performed to remove the organic molecules around the GNRs.

which leads to signal loss, as the cavities are not accessible to fresh molecules.

In this work, we demonstrate the first two-photon-excited fluorescence enhancement experiments on single organic fluorophores using end-to-end assembled GNR dimers. The end-to-end assembly was achieved by tip-specific functionalization of the GNRs with molecular linkers. We employed the molecular linkers based on biomolecule pairs consisting of two biotin disulfides bridged by a streptavidin, which ensured an open cavity for single-molecule detection with an interparticle gap of around 5 nm[37]. We applied the GNR dimers to enhance the two-photon-excited fluorescence of commercial organic dyes, which have a broad two-photon absorption band in the infrared range. Theoretical results indicate that two-photon-excited fluorescence enhancement of these molecules can reach 10^7 in the gaps between the GNRs. With such high enhancement factors, we successfully detected enhanced two-photon-excited fluorescence from single molecules.

5.2. Results and discussion

Fig 5.1 schematically illustrates our approach of GNR dimers synthesis. Briefly, a GNR colloid solution (simplified as GNR solution in following) was mixed with the pretreated biomolecular linkers that consisted of at least two biotin disulfides linked with one streptavidin. These molecular linkers were bound to the tips of the GNR through thiol attachment in the present of cetyl(trimethyl)ammonium bromide (CTAB), which occupied more com-

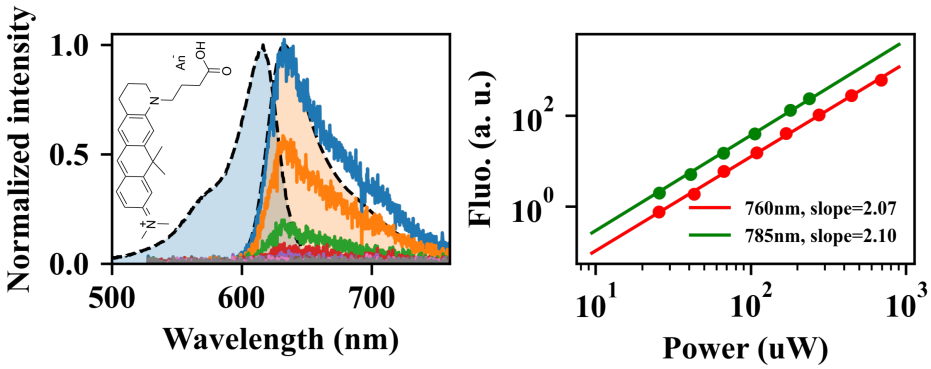

Figure 5.2: Optical characterization of ATTO 610. (a) The blue- and yellow-shaded bands with dashed outline represent the normalized one-photon absorption (blue-shaded) and emission (yellow-shaded) spectra of ATTO 610 , respectively. The solid lines give the emission spectra of 4 μM ATTO 610 excited by $\sim$ 220 fs laser pulses at 760 nm with different powers. The integrating time for recording the spectra was set as 120 s. The inset shows the chemical structure of ATTO 610. (b) Power dependence of the emission integrated over wavelengths ranging from 555 nm to 728 nm, excited at the wavelength of 760 nm (red dots) and 785 nm (green dots). The power law fits (solid lines) show perfect quadratic dependence of the emission on the excitation power for both excitation wavelengths.

pactly the sides of GNRs, leaving only the tips reactive for the linkers. Therefore, the GNRs were linked by the molecular linker at the ends, leading to the end-to-end assembly of GNRs in the solution (figure 5.1a). We monitored the assembly process by measuring the real-time absorption spectrum of the mixture to ensure most assembled structures to be the end-to-end dimers. A small amount (10 μL) of the assemblies of GNRs were deposited from the solution onto a clean cover glass slide. We stop the assembling by covering the slide with the assembly solution with an other clean slide (see figures 5.1b and d). By using this strategy, a very thin film of the assembly solution is formed between the two slides, which dry very quickly, leaving every assembled GNRs sticking on one of the glass slides. We performed UV/Ozone cleaning to remove all the organic molecules around the GNRs to ensure the proper sticking of the GNRs on the glass surface, and to create free gaps between the GNRs of the assemblies.

We performed two-photon-excited single-molecule fluorescence experiments on a commercial dye called ATTO 610 (ATTO-TEC) enhanced by the GNR dimer structures. ATTO 610 is a bright dye with high photostability under one-photon excitation. It has a one-photon absorption maximum at 616 nm and an emission maximum at 633 nm. ATTO 610 also exhibits two-photon absorption in the infrared range under illumination with ultrashort pulses. In our experiment, a mode-locked Ti:Sapphire laser (Coherent Mira 900) with a pulse width of $\sim$ 220 fs was used as the two-photon excitation source. The experiment was performed on a home-built confocal microscope. Circular polarization was used to enable the excitation of all the GNR dimers irrespective of their random orientations in the focal plane.

By illuminating the aqueous solution of ATTO 610 with the fs laser at different wavelengths in the infrared, we got very faint fluorescence signals with spectral shape similar to the fluorescence of ATTO 610 under one-photon excitation. To verify that the emission stems from TPA, we collected the emission spectra with respect to the excitation intensity.

Fig 5.2a illustrates the power dependence of the emission spectra at the excitation wavelength of 760 nm. As is shown in Fig 5.2a, the emission spectra show little change in the shape but the intensities decrease dramatically as we reduce the excitation power. As is depicted in Fig 5.2b, the integrated intensities over the emission spectra, for both the excitation wavelengths of 760 nm and 785 nm, show a perfect quadratic dependence on the excitation power, confirming that the observed fluorescence arose from two-photon excitation for both excitation wavelengths. The broad TPA band of ATTO 610 offers us the flexibility of optimizing the collected signals by tuning the excitation wavelength and the plasmon resonance of the GNR dimers.

We performed single-molecule experiments on the assembled GNR dimers immobilized on a clean glass cover slide. The GNRs were immobilized on the glass by strong Van der Waals force after removal of all organic moleclules through ozone/UV cleaning. A cross was scratched on the slide as the alignment mark to locate the positions of the observed particles for further studies. In the experiments, we chose commercial GNRs (NR-40-700, NanoSeedz) as the building blocks of the assemblies. These rods have an average diameter of 40 nm and a longitudinal plasmon mode at the wavelength of 700 nm. Simulations predict the bright plasmon mode of the end-to-end gold nanorod redshifted to $\sim$ 760 nm after removing all the organic molecules, if we assume the interparticle separation of the dimer to be $\sim$ 5 nm, considering the molecular size of streptavidin. Thereafter the laser wavelength of 760 nm was used as the excitation to ensure maximum enhancement. After the optical measurements, SEM images were taken to examine the structural details of the measured assemblies.

Fig 5.3 illustrates a typical single-molecule measurement of the two-photon-excited fluorescence enhanced by a GNR assembly. We first recorded the photoluminescence of each particle under excitation with the femtosecond laser, in the presence of 20 nM ATTO 610 molecules. A short-pass filter ($\leq$ 725 nm,) was used to remove intrinsic luminescence background from the gold particles. The particles showing intensity bursts in these luminescence time traces were supposed to be the assembled structures. Indeed simulations and further experiments both show that, with enhancement by a single GNR, it is very difficult to extract single molecule fluorescence from the luminescence background of the nanorod under two photon excitation. After rinsing the sample with clean water several times, we measured the one-photon excited luminescence spectra of the particles to determine their plasmon resonances. With the help of the masked cross, we further identified the structures of these gold nanorod assemblies by comparing the SEM image with the scatter image, as one can see from the example in Fig 5.3a.

We first compared two-photon-excited fluorescence enhancement on two typical GNR dimers, assembled in either the end-to-end or the side-by-side configuration. As is shown in Fig 5.3b, for the end-to-end dimers, the plasmon resonance was red-shifted to wavelengths around 760 nm as a result of the longitudinal plamonic coupling of each rod, while for the side-by-side structure, the plasmon resonance showed little change compared to the single GNRs. As is depicted in Fig 5.3b, for both side-by-side and end-to-end dimers, we observed the intensity bursts in the luminescence time traces. From Fig 5.3b, we can see for the maximum intensity of the bursts from the end-to-end dimer was significantly greater than those from the side-by-side structure, indicating the much larger two-photon fluorescence enhancement within the plasmonic hotspot of the end-to-end dimers. By analyzing the

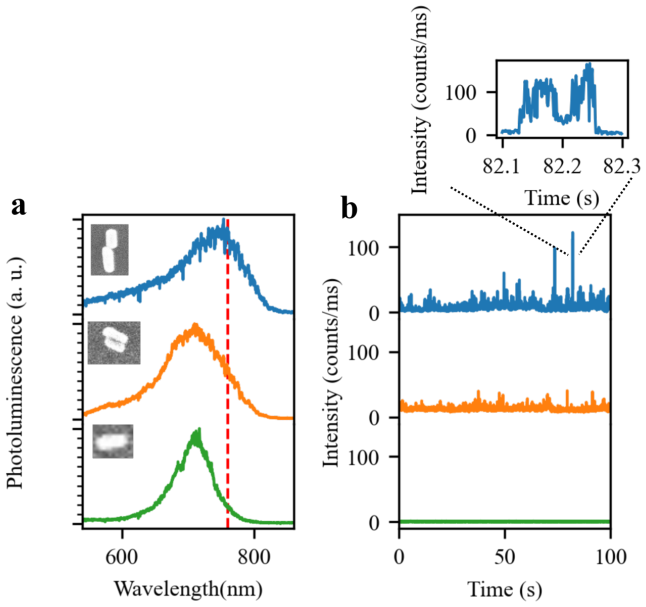

Figure 5.3: Two-photon-excited single molecule fluorescence enhancement. (a) One-photon-excited luminescence spectrum taken on three different structures made of gold nanorods: end-to-end dimer, side-by-side dimer, and a single gold nanorod, acquired under the excitation by a circular polarized 532 nm CW laser. Inset shows the SEM images of the structures. (b) The respective intensity traces taken in the presence of 20 nM ATTO 610 dyes, excited by a femtosecond laser at the wavelength of 760 nm and at the power of $\sim 2\ \mu$W.

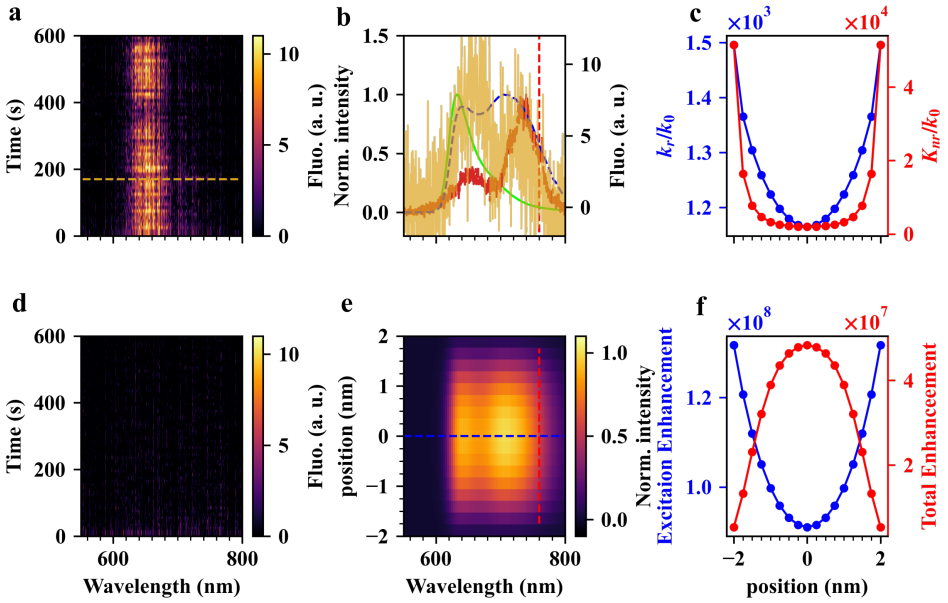

Figure 5.4: Two-photon-excited fluorescence enhancement in the plasmonic hotspot of an end-to-end gold nanorod dimer. (a) and (d) Real-time spectra on gold nanorod dimer with (a) and without (d) the presence of 100 nM ATTO 610 in solution. (b) Comparison of the measured spectrum (orange, corresponding to the recorded time of orange dashed in a) with the spectrum of free ATTO 610 dye in solution (green solid), and the simulated enhanced spectra (blue dashed, corresponding the positions of blue dashed in e) in the hotspot. Red solid line is the scattering spectrum of the nanoparticle. (e) Simulated emission spectra of the ATTO 610 molecules at different positions along the main axis of the gold nanorod dimer in the gap. (c) Calculated radiative (blue) and non-radiative (red) enhancement factor as functions of the position in the hotspot, and (f) the respective excitation (blue) and total emission (red) enhancements. The vetical red dashed lines in (b, e) represent the wavelength of the fs laser.

highest bursts in the fluorescence time trace enhanced by the end-to-end dimer (figure 5.3b, inset), we see typical single-step single-molecule bursts with a time duration in the order of 10 ms, which confirm that the enhanced fluorescence signals are stemming form single molecules. We also notice that, as a result of the plasmon red shift, the remaining luminescence backgrounds of the end-to-end dimers, after passing through the short-pass filter, were reduced more obviously than the background of the side-by-side structure, which may further improve the single-molecule detection sensitivity of the two-photon-excited fluorescence.

Before attributing the intensity bursts to the fluorescence from single ATTO 610 molecules enhanced inside the plasmonics hotspot, we monitored the real-time spectra on the particle excited by the femtosecond laser, with/without the presence of 100 nM ATTO 610 in solution. Fig 5.4a shows one case of the real-time recording of the plasmon-enhanced two-photon-excited single-molecule emission spectra. The spectra were recorded in a time series of 10 minutes with spectral acquisition time of 10 s for each step. In the measurement, we kept the excitation power as low as possible ($\sim 0.5\ \mu$W) to exclude the influence of the luminescence backgrounds from gold particles. From Fig 5.4a, we can see clearly the emission

pattern between $620\ \mathrm{nm}$ and $690\ \mathrm{nm}$, with the intensities fluctuating over the time. Such emission pattern can be removed by replacing the ATTO 610 solution with clean water, as is shown in Fig 5.4d, which implies the signals were from ATTO 610 molecules near the particle. The spectral range, shown in figure 5.4a, was noticeably wider compared to the emission of free dyes in solution (green solided line), which was mainly due to coupling of the molecules with the plasmonic modes.

Specifically, we compare one recorded spectrum (corresponding to the dashed line in figure 5.4a) with the spectrum of the free dye (green dashed line) in figure 5.4b. The result shows drastic spectral shaping for the emission enhanced by the plasmoic nanoresonator, as we can clearly see a second peak at the wavelength around $730\ \mathrm{nm}$ in the enhanced spectrum (orange line). This spectral shaping can be explained by the the well-known effect that the far-field emission of an emitter can be modified by coupling with a plasmonic structure[38, 39], through i) the Purcell effect that enhances the spontaneous emission rate; ii) the nonradiative dissipation loss inside the metal that quenches the emission. Here, we employed a simple radiative dipole model to investigate the influence of the emission of ATTO 610 molecules by the GNR dimer. For the sake of simplicity, we considered the dimer consisting of two identical GNRs with the longitudinal axes oriented in parallel, and separated by a gap of $5\ \mathrm{nm}$. More details about the simulations are given in the Supporting Information.

From Fig 5.4b, we see a good agreement between the spectral shapes of the measured emission and the simulated emission calculated at two different positions showing in Fig 5.4e (the green and blue dashed). The increase of the emission rates in the band of longer wavelength, therefore, can be attributed to the selective enhancement of the vibrational subbands in resonance with the plasmon modes. From the simulations, we also notice that the nonradiative dissipation dominates the decay rates of the excited molecule inside the gap (figure 5.4c), which quench the emission rates by a factor of about 2 in the center of the dimer (figure 5.4f). As the molecule moves closer to the gold surface, the non-radiative rate increases more than the excitation and radiative enhancements, which further reduce the fluorescence enhancement, as is shown in Figs. 5.4e and 5.4f. As a consequence, we see a maximum enhancement factor of about 5×10^7 for the two-photon-excited fluorescence at the center of the dimer.

To confirm the observed emission indeed steams from two-photon excitation, we performed a power dependence measurement on an individual GNR self-assembled nanostructure that gave single-molecule bursts. Time traces with intensity bursts excited at different powers are displayed in figure 5.5a. At the lower excitation power, as expected, we see the increase of intensity bursts as the excitation power increases. After the burst intensities reach values of about $10^2\ \mathrm{counts/ms}$, we see the recorded intensity bursts is saturated as the excitation power is continually increased. This saturation might come from saturation of the molecules, or due to the plasmon damping as the result of hot electron generation, which might reduce the enhancement factor. Nonetheless, we find a quadratic dependence of the maximum fluorescence bursts on the excitation power (blue line in figure 5.5b) for the intensities below $10^5\ \mathrm{counts/s}$. These maximum intensity bursts could be attributed to the signals from the molecules at the best position for enhancement. As the molecules can approach or stick to glass surface at any position inside plasmonic hotspot, with random orientations, the enhancement factor for the molecules can vary very randomly, resulting in

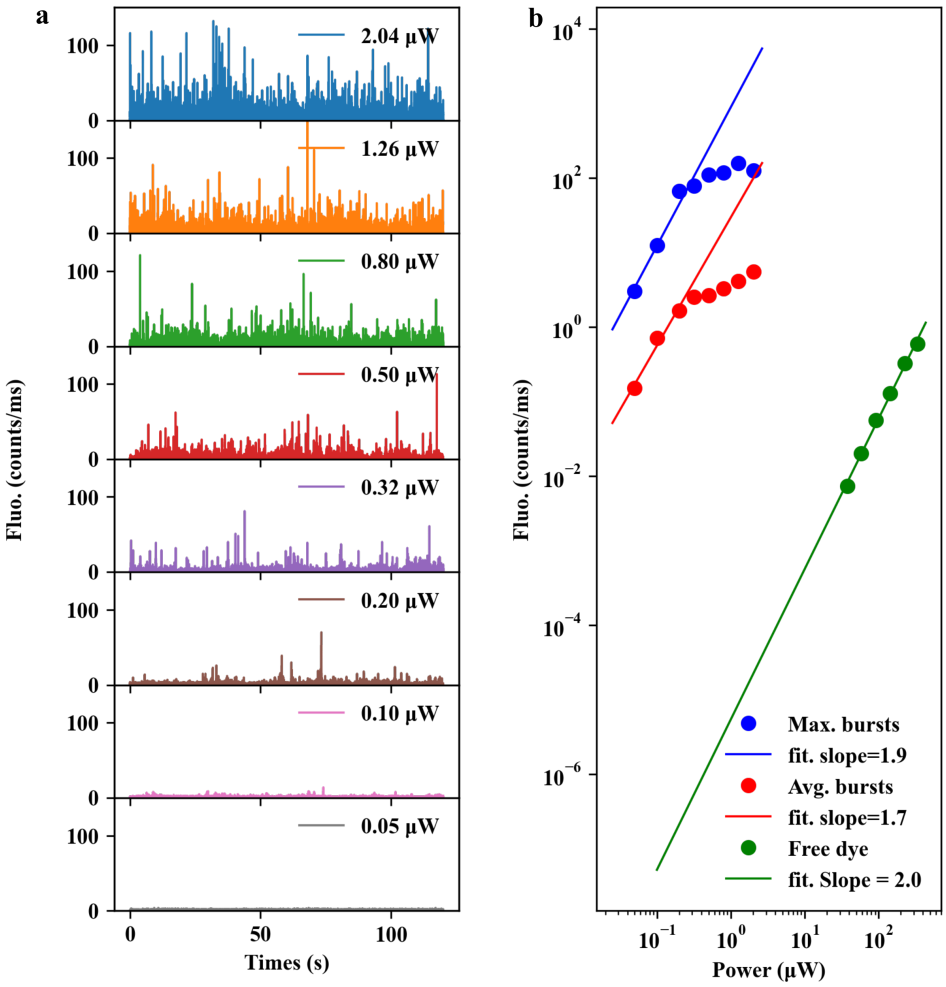

Figure 5.5: Power dependence of the emission. (a) Emission time trace (1 ms/bin) as a function of excitation power recorded on a gold nanorod self-assembled nanostructure. The particle was immersed in a solution of ATTO 610 with the concentration of 30 nM. (b) Power dependence of the maximum fluorescence burst intensity (blue), the averaged burst intensity (red), and the averaged unenhanced fluorescence per molecule.

a random distribution of intensity bursts in each time trace. This random effect can be considered by taking the average of the burst intensities for each trace. As shown in figure 5.5b, we see an approximated quadratic dependence of the averaged intensity on the excitation power with the fitted slope of 1.7 (red line).

In order to calculate the enhancement factor of the two-photon-excited fluorescence, we compared the enhanced burst intensities with the unenhanced signals from a molecule in solution. We performed power-dependent measurements for ATTO 610 molecules in the solution ($3\ \mu\mathrm{M}$) to estimate the two-photon-excited fluorescence signals excited at low power, especially for excitation below the saturation power, where the unenhanced signal in the solution is too weak to be detected. Shown in figure S5.2b, the averaged intensity of the fluorescence time trace measured in the solution (figure S5.2a) also scales quadratically with the excitation power. By taking account of the number of molecules in the focus volume, we show the quadratic dependence of the averaged fluorescence per molecule on the excitation power (green line) in figure 5.5b. By scaling the unenhanced fluorescence quadratically with the excitation power, we can estimate an enhancement factor of up to $\sim 10^8$ for the two-photon-excited fluorescence below saturation.

5.3. Conclusion

In summary, we have demonstrated the single-molecule detection of two-photon-excited fluorescence via the enhancement of self-assembled GNR dimers. In the experiment, we control the interparticle gaps by exploring the streptavidin-biotion disulfides as molecular linkers, which separate the nanorods by a distance of about $5\ \mathrm{nm}$. Theoretical results indicate that two-photon-excited fluorescence rates can be enhanced by factor of up to $10^7 \sim 10^8$. With such high enhancement factor, we were able to detect the two-photon-excited fluorescence from single ATTO 610 dyes. Correlated scanning electron microscope images (SEM) were taken later to examine the configurations of the GNR dimer structures.

S5.1. Supporting Information

Assembly of gold nanorods

The GNRs were self-assembled in an end-to-end fashion through the molecular linkers based on the specific molecular recognition of biotin and streptavidin. For the assembly, a biotin disulfide solution ($20\mu\mathrm{M}$), EZ-link Biotin HPDP (Pierce), was pretreated with a reducing agent solution, TCEP (tris(2-carboxyethyl)phosphine), with a 1:10 biotin/TCEP ratio. This reaction was allowed at room temperature for $15\ \mathrm{min}$ to break the disulfide bonds in the Biotin HPDP molecules. The mixture solution was added to the streptavidin solution ($1\ \mu\mathrm{M}$) in phosphate buffered saline solution (PBS, pH = 7.4), with a ratio of 4:1 for biotin/streptavidin. The incubation lasted for $45\ \mathrm{min}$ to allow the binding of streptavidin with at least two biotin. The excess unbound biotin disulfide and TCEP were removed by centrifugation in centrifugal filter devices (Ultra-0.5 10K, Amicon). The residue was dispersed in $100\ \mu\mathrm{L}$ deionized water. A commercially available GNR solution (NA-40-700, OD-50, Nanoseedz) was diluted to the concentration according to its optical density (OD) of ~ 0.3. The GNR solution had plasmon absorption at $700\ \mathrm{nm}$, and the average diameter of the GNRs were $40\ \mathrm{nm}$.

40 μL of a biotin-streptavidin solution was added into 500 μL as-prepared GNR solution to trigger the end-to-end assembly of the GNRs. The assembly of GNRs was monitored and recorded by a Cary 50 UV-Vis spectrometer (Varian Inc. Agilent Technology, USA) every 2 min (see figure S5.1).

Deposition of gold nanorod assemblies

When the extinction peak of the solution dropped by a ratio of $1/4$, 10 μL of the GNR assembly solution was deposited onto a clean cover glass slide (Menzel-Gläser, $\phi = 25$ mm, No. 1) with a scratched cross, and was immediately covered with a second glass slide. The capillary action between the two slides squeezed the assembled solution and formed a thin layer. This strategy helps stop further assembly of GNR, and deposit the GNR assemblies uniformly on the surfaces of the glass slides. After deposition, the two slides were separated by immersing in clean water. After that, we performed UV/Ozone cleaning to remove all the organic molecules around the GNRs to ensure the proper sticking of the GNRs on the glass surface, and to create free gaps between the GNRs of the assemblies.

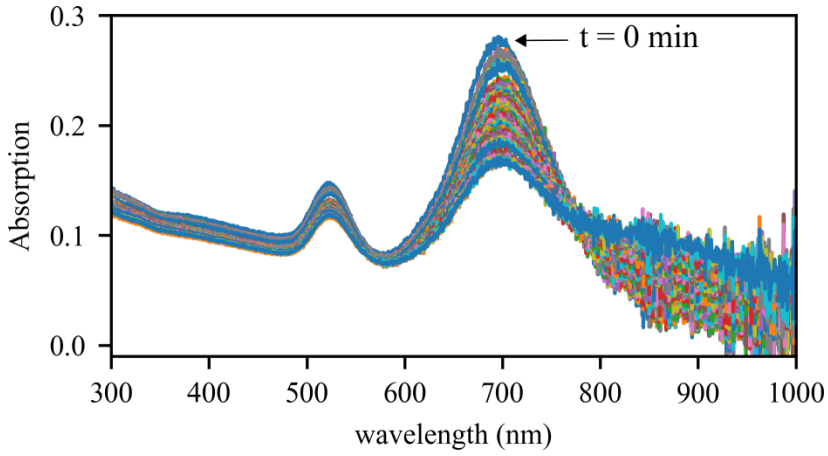

Figure S5.1: Extinction spectral evolution for gold nanorods in the presence of biotinylated streptavidin. The spectra were recorded every 2 min.

Two-photon microscopy

We performed two-photon-excited fluorescence measurements on a home-built confocal microscopy. A mode-locked titanium-sapphire laser (Coherent Mira 900), with the pulse repetition rate of 76 MHz and pulse width of $\sim$ 220 fs, was used as the two-photon excitation source. Circular polarization was in the whole study, as it can efficiently excite all gold nanorod assemblies, regardless of their random orientations in the focal plane. The light source was focused by an oil immersion objective with a numerical aperture (NA) of 1.4. A short-pass filter (Fluorescence Edge Filter 745/SP, BrightLine) was used to separate the flu-

orescence signal from the background of scattered laser. To get the one-photon excited photoluminescence spectrum of each gold nanorod assembly, a 532 nm continuous-wave laser was used as the excitation source, and the spectrum was recorded with a liquid-nitrogen-cooled spectrometer (Acton SP-500i, Princeton Instruments). Fluorescence time traces were recorded with an avalanche photodiode (SPCM-AQRH-16, Excelitas) and processed with a time-correlated single-photon counting (TCSPC) card (TimeHarp 200, PicoQuant GmbH).

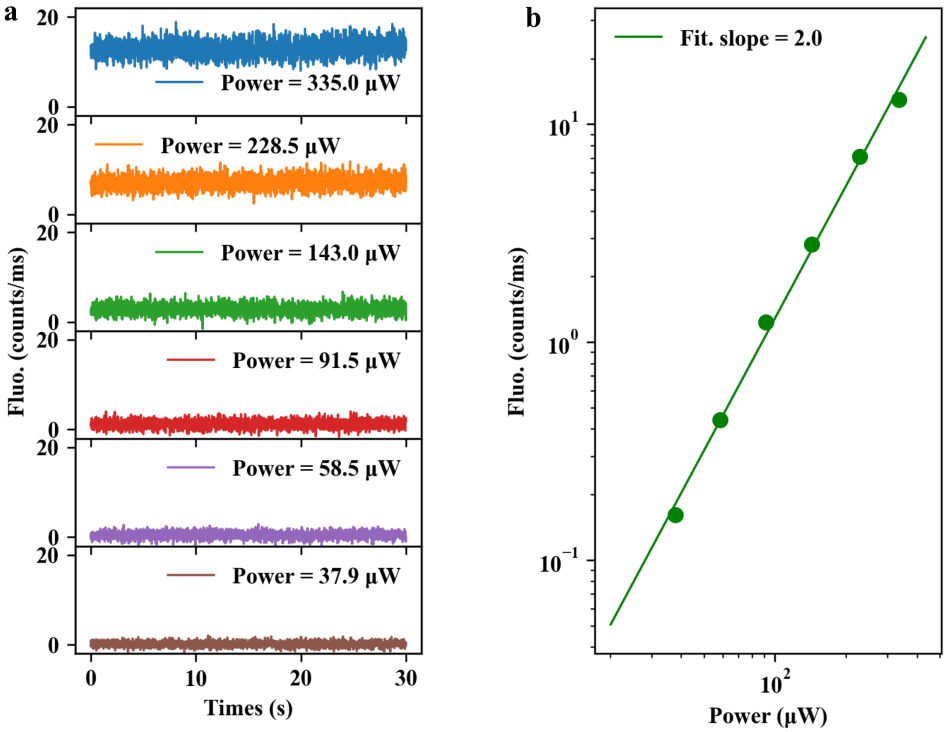

Figure S5.2: Power dependence of the emission measured in ATTO 610 solution (3 μM). (a) Fluorescence time traces excited with different laser powers. (b) Averaged fluorescence intensity as a function of the excitation power.

Two-photon-excited fluorescence of ATTO 610 in solution

We first recorded the emission spectra from the ATTO 610 solution ($\sim$ 5 μM) excited at different laser powers. The exposure time was set as 120 s for each spectrum. In the study, we compared the power-dependent emission of ATTO 610 for two different excitation wavelengths 760 nm and 785 nm, while keeping the width and repetition rate of the pulse as constant. For both wavelengths, the integrated intensity (wavelength range from 555 nm to 728 nm) depends quadratically on the excitation power.

To estimate the average fluorescence rate of individual ATTO 610 molecules without enhancement, we performed power-dependent measurements on an ATTO 610 solution with the concentration of 3 μM. Due to the extremely weak two-photon excitation efficiency

of these molecules, much higher laser power was required to get enough signal from the solution, compared to enhanced experiments. To get rid of the unavoidable background of the scattered laser at high power, we first performed power-dependent measurements in a blank solution without any dyes in it. Time traces were recorded again after replacing the water with an ATTO 610 solution at the same conditions of the blank experiments. The fluorescence signals from the molecules, therefore, can be represented by intensity time traces with molecules after subtraction of the mean intensity recorded in the blank solution (see figure S5.2a).

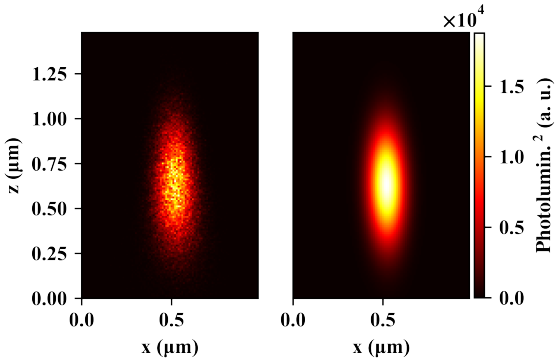

Figure S5.3: xz section of the two-photon excitation point spread function measured with a gold nanorod. Left, the xz section of the square of one-photon excited photoluminescence exited by pulse laser. Right two-dimensional Gaussian fit of the PFS, from which we get width of PSF, $\omega_x = 0.14\ \mu$m and $\omega_z = 0.42\ \mu$m and the PSF volume of 0.02 ± 0.01 fL.

Figure S5.2b shows the quadratic dependence of the average fluorescence intensity measured in solution on the excitation laser power, indicating the fluorescence arose from TPA. The overall recorded signals can be simply considered as coming from the contributions of the molecules in the confocal volume.

We calculated the size of the confocal volume for two-photon excitation by measuring the confocal point spread function (PSF) of the setup. We first scanned sectional one-photon excited luminescence images of a single GNR immersed in water excited with the pulse laser. The PSF of the setup for two-photon excitation can expressed as the square of the PSF for one photon. Shown in figure S5.3, we estimated the two-photon excitation confocal volume to be 0.02 ± 0.01 fL, hence we estimate that about 20 molecules are in the upper half of the confocal volume for dye concentration of 3 μM.

Numerical simulations of two-photon-excited fluorescence enhancement

We performed numerical simulations for the two-photon-excited fluorescence enhancement under weak excitation, where the excitation enhancement and the emission enhancement can be treated separately[27]. The scheme for the simulations is illustrated in figure S5.4. For the sake of simplicity, we considered the dimer consisting of two identical GNRs with the longitudinal axes oriented in parallel, and separated by a gap of 5 nm. The size of each GNR was set as 40 nm × 88 nm to guarantee a resonance at 760 nm. The ATTO 610

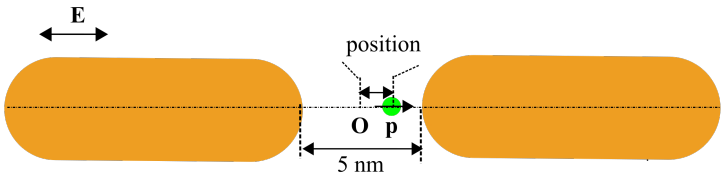

Figure S5.4: Scheme for the numerical simulations.

molecule was modeled as a radiative dipole with the position and dipole moment aligned along the longitudinal axis of the GNR dimer inside the gap. In the simulations, each GNR was modeled a spherically capped cylinder. The dielectric permitivity for gold was taken from Johnson and Chiristy[40], and the refractive index of the ambient medium was taken as 1.33.

For two-photon-excited fluorescence, the excitation enhancement is related to near-field enhancement as

$$\xi_{\mathrm{exc}}^{(2)} = |\mathbf{E}|^4/|\mathbf{E}_0|^4, \tag{S5.1}$$

where ($\mathbf{E}$) and $\mathbf{E}_0$ is the (near-)field (with) and without the gold nanorod dimer.

To evaluate the enhancement factor by the GNR dimer numerically, we applied a classical electrodynamics approach based on a boundary element method (SCUFF-EM) [41, 42] to simulate the excitation and emission enhancement, respectively. To calculate the excitation enhancement, we excited the dimer structure with a plane wave with the polarization along the longitudinal axis of the dimer. The enhancement factor of the radiative rate (ξ_{rad}) and the additional non-radiative rate ($K_{\mathrm{nr}}/k_{\mathrm{r}}^0$) were calculated following [29, 34], where k_{r}^0 is the intrinsic radiative rate of the dye. The expected emission spectrum enhanced by the dimer can expressed as[38]

$$F(\omega) = \xi_{\mathrm{exc}}^{(2)} \cdot f(\omega) \cdot \xi_{\mathrm{rad}}(\omega) \cdot \frac{1/\eta_0}{<\xi_{\mathrm{rad}} + K_{\mathrm{nr}}/k_{\mathrm{r}}^0 - 1> + 1/\eta_0}, \tag{S5.2}$$

where $f(\omega)$ is the normalized emission spectrum of ATTO 610 in solution, $<\cdots>$ represents the averaging over the emission spectrum of $f(\omega)$, η_0 is the intrinsic quantum yield of the molecule, which is 0.7 for ATTO 610. The overall enhancement can be written as

$$\xi_{\mathrm{total}} = \xi_{\mathrm{exc}}^{(2)} \cdot <\xi_{\mathrm{rad}}> \cdot \frac{1/\eta_0}{<\xi_{\mathrm{rad}} + K_{\mathrm{nr}}/k_{\mathrm{r}}^0 - 1> + 1/\eta_0}. \tag{S5.3}$$

References

[1] Peter T. C. So, Chen Y. Dong, Barry R. Masters, and Keith M. Berland. Two-Photon Excitation Fluorescence Microscopy. *Annual Review of Biomedical Engineering*, 2(1):399–429, August 2000.

[2] Patrik R. Callis. On the theory of two-photon induced fluorescence anisotropy with application to indoles. *The Journal of Chemical Physics*, 99(1):27–37, July 1993.

[3] Maria Göppert-Mayer. Über Elementarakte mit zwei Quantensprüngen. 401(3):273–294.

[4] P. A. Franken, A. E. Hill, C. W. Peters, and G. Weinreich. Generation of Optical Harmonics. *Physical Review Letters*, 7(4):118–119, August 1961.

[5] W. Kaiser and C. G. B. Garrett. Two-Photon Excitation in Ca${\mathrm{F}}_{2}$: ${\mathrm{Eu}}ˆ{2+}$. *Physical Review Letters*, 7(6):229–231, September 1961.

[6] Patrick Theer, Mazahir T. Hasan, and Winfried Denk. Two-photon imaging to a depth of 1000 Mm in living brains by use of a Ti:Al_2O_3 regenerative amplifier. *Optics Letters*, 28(12):1022–1024, June 2003.

[7] Fritjof Helmchen and Winfried Denk. Deep tissue two-photon microscopy. *Nature Methods*, 2(12):932–940, December 2005.

[8] William A. Mohler, Jeffrey S. Simske, Ellen M. Williams-Masson, Jeffrey D. Hardin, and John G. White. Dynamics and ultrastructure of developmental cell fusions in the Caenorhabditis elegans hypodermis. *Current Biology*, 8(19):1087–1091, September 1998.

[9] Jayne M. Squirrell, David L. Wokosin, John G. White, and Barry D. Bavister. Long-term two-photon fluorescence imaging of mammalian embryos without compromising viability. *Nature Biotechnology*, 17(8):763–767, August 1999.

[10] W. Denk, J. H. Strickler, and W. W. Webb. Two-photon laser scanning fluorescence microscopy. *Science*, 248(4951):73–76, April 1990.

[11] CJ R SHEPPARD and Min Gu. Image formation in two-photon fluorescence microscopy. *Optik (Stuttgart)*, 86(3):104–106, 1990.

[12] Min Gu and C. J. R. Sheppard. Comparison of three-dimensional imaging properties between two-photon and single-photon fluorescence microscopy. *Journal of Microscopy*, 177(2):128–137, 1995.

[13] Shoji Maruo, Osamu Nakamura, and Satoshi Kawata. Three-dimensional microfabrication with two-photon-absorbed photopolymerization. *Optics Letters*, 22(2):132–134, January 1997.

[14] Gilles Lemercier, Jean-Christophe Mulatier, Cécile Martineau, Rémi Anémian, Chantal Andraud, Irène Wang, Olivier Stéphan, Nadia Amari, and Patrice Baldeck. Two-photon absorption: From optical power limiting to 3D microfabrication. *Comptes Rendus Chimie*, 8(8):1308–1316, August 2005.

[15] Shoji Maruo and Hiroyuki Inoue. Optically driven micropump produced by three-dimensional two-photon microfabrication. *Applied Physics Letters*, 89(14):144101, October 2006.

[16] Jin-Feng Xing, Xian-Zi Dong, Wei-Qiang Chen, Xuan-Ming Duan, Nobuyuki Takeyasu, Takuo Tanaka, and Satoshi Kawata. Improving spatial resolution of two-photon microfabrication by using photoinitiator with high initiating efficiency. *Applied Physics Letters*, 90(13):131106, March 2007.

[17] Xiaoying Wang, Zhenping Wei, Charles Zuwu Baysah, Meiling Zheng, and Jinfeng Xing. Biomaterial-based microstructures fabricated by two-photon polymerization microfabrication technology. *RSC Advances*, 9(59):34472–34480, October 2019.

[18] Dimitri A. Parthenopoulos and Peter M. Rentzepis. Three-Dimensional Optical Storage Memory. *Science*, 245(4920):843–845, August 1989.

[19] James H. Strickler and Watt W. Webb. 3-D optical data storage by two-photon excitation. *Advanced Materials*, 5(6):479–481, 1993.

[20] Shouzhi Pu, Huohong Tang, Bing Chen, Jingkun Xu, and Wenhao Huang. Photochromic diarylethene for two-photon 3D optical storage. *Materials Letters*, 60(29):3553–3557, December 2006.

[21] A. S. Dvornikov, E. P. Walker, and P. M. Rentzepis. Two-Photon Three-Dimensional Optical Storage Memory. *The Journal of Physical Chemistry A*, 113(49):13633–13644, December 2009.

[22] Brandon C. Marin, Su-Wen Hsu, Li Chen, Ashley Lo, Darwin W. Zwissler, Zhaowei Liu, and Andrea R. Tao. Plasmon-Enhanced Two-Photon Absorption in Photoluminescent Semiconductor Nanocrystals. *ACS Photonics*, 3(4):526–531, April 2016.

[23] Janice B. Rabor, Koki Kawamura, Junichi Kurawaki, and Yasuro Niidome. Plasmon-enhanced two-photon excitation fluorescence of rhodamine 6G and an Eu-diketonate complex by a picosecond diode laser. *Analyst*, 144(13):4045–4050, June 2019.

[24] Martin Bauch, Koji Toma, Mana Toma, Qingwen Zhang, and Jakub Dostalek. Plasmon-Enhanced Fluorescence Biosensors: A Review. *Plasmonics*, 9(4):781–799, August 2014.

[25] Peter Zijlstra, Pedro M. R. Paulo, and Michel Orrit. Optical detection of single non-absorbing molecules using the surface plasmon resonance of a gold nanorod. *Nature Nanotechnology*, 7(6):379–382, June 2012.

[26] Haifeng Yuan, Saumyakanti Khatua, Peter Zijlstra, Mustafa Yorulmaz, and Michel Orrit. Thousand-fold Enhancement of Single-Molecule Fluorescence Near a Single Gold Nanorod. *Angewandte Chemie*, 125(4):1255–1259, 2013.

[27] Saumyakanti Khatua, Pedro M. R. Paulo, Haifeng Yuan, Ankur Gupta, Peter Zijlstra, and Michel Orrit. Resonant Plasmonic Enhancement of Single-Molecule Fluorescence by Individual Gold Nanorods. *ACS Nano*, 8(5):4440–4449, May 2014.

[28] Weichun Zhang, Martín Caldarola, Xuxing Lu, Biswajit Pradhan, and Michel Orrit. Single-molecule fluorescence enhancement of a near-infrared dye by gold nanorods using DNA transient binding. *Physical Chemistry Chemical Physics*, 20(31):20468–20475, 2018.

[29] Xuxing Lu, Gang Ye, Deep Punj, Ryan C. Chiechi, and Michel Orrit. Quantum Yield Limits for the Detection of Single-Molecule Fluorescence Enhancement by a Gold Nanorod. *ACS Photonics*, 7(9):2498–2505, September 2020.

[30] Alexandra P. Francisco, David Botequim, Duarte M. F. Prazeres, Vanda V. Serra, Sílvia M. B. Costa, César A. T. Laia, and Pedro M. R. Paulo. Extreme Enhancement of Single-Molecule Fluorescence from Porphyrins Induced by Gold Nanodimer Antennas. *The Journal of Physical Chemistry Letters*, 10(7):1542–1549, April 2019.

[31] Tianyue Zhang, Guowei Lu, Jie Liu, Hongming Shen, Pascal Perriat, Matteo Martini, Olivier Tillement, and Qihuang Gong. Strong two-photon fluorescence enhanced jointly by dipolar and quadrupolar modes of a single plasmonic nanostructure. *Applied Physics Letters*, 101(5):051109, July 2012.

[32] Ding-Feng Zhang, Shuang Li, Qing-Hua Xu, and Yong Cao. Aggregation-Induced Plasmon Coupling-Enhanced One- and Two-Photon Excitation Fluorescence by Silver Nanoparticles. *Langmuir*, 36(17):4721–4727, May 2020.

[33] Russell A. Jensen, I-Chun Huang, Ou Chen, Jennifer T. Choy, Thomas S. Bischof, Marko Lončar, and Moungi G. Bawendi. Optical Trapping and Two-Photon Excitation of Colloidal Quantum Dots Using Bowtie Apertures. *ACS Photonics*, 3(3):423–427, March 2016.

[34] Weichun Zhang, Martín Caldarola, Xuxing Lu, and Michel Orrit. Plasmonic Enhancement of Two-Photon-Excited Luminescence of Single Quantum Dots by Individual Gold Nanorods. *ACS Photonics*, 5(7):2960–2968, July 2018.

[35] Oluwafemi S. Ojambati, Rohit Chikkaraddy, William M. Deacon, Junyang Huang, Demelza Wright, and Jeremy J. Baumberg. Efficient Generation of Two-Photon Excited Phosphorescence from Molecules in Plasmonic Nanocavities. *Nano Letters*, 20(6):4653–4658, June 2020.

[36] J. Mertz, C. Xu, and W. W. Webb. Single-molecule detection by two-photon-excited fluorescence. *Optics Letters*, 20(24):2532–2534, December 1995.

[37] K. K. Caswell, James N. Wilson, Uwe H. F. Bunz, and Catherine J. Murphy. Preferential End-to-End Assembly of Gold Nanorods by Biotin-Streptavidin Connectors. *Journal of the American Chemical Society*, 125(46):13914–13915, November 2003.

[38] M. Ringler, A. Schwemer, M. Wunderlich, A. Nichtl, K. Kürzinger, T. A. Klar, and J. Feldmann. Shaping Emission Spectra of Fluorescent Molecules with Single Plasmonic Nanoresonators. *Physical Review Letters*, 100(20):203002, May 2008.

[39] G. Vecchi, V. Giannini, and J. Gómez Rivas. Shaping the Fluorescent Emission by Lattice Resonances in Plasmonic Crystals of Nanoantennas. *Physical Review Letters*, 102(14):146807, April 2009.

[40] P. B. Johnson and R. W. Christy. Optical Constants of the Noble Metals. *Physical Review B*, 6(12):4370–4379, December 1972.

[41] M. T. Homer Reid and S. G. Johnson. Efficient Computation of Power, Force, and Torque in BEM Scattering Calculations. *ArXiv e-prints*, July 2013.

[42] `http://github.com/homerreid/scuff-EM`.

6

Summary

This thesis provides a general strategy to handle the major obstacle in single-molecule detection, that the optical signals from common molecules are normally too weak compared to the background. Based on fluorescence, we can suppress the background efficiently by spectral filtering as the photons are emitted at longer wavelength than excitation light (Stokes-shifted); based on the plasmonic enhancement, we are able to enhance the brightnesses of the emitters, hence to improve the signal-to-noise ratio in the single-molecule detection. We exploit the single-crystalline gold nanorods (GNRs) as our basic frameworks in the studies because of their strong near-field enhancement and because of their tunable plasmon resonance. In the whole study, we investigate theoretically and experimentally single-molecule detection with the fluorescence enhancement by a single GNR or by a GNR dimer for the ultra-weak emitters, which can either be molecules with extremely low quantum yield ($\sim 10^{-4}$), or molecules under two-photon excitation.

One/two-photon-excited fluorescence enhancement: single GNR vs GNR dimer

We first theoretically investigate single-molecule fluorescence enhancement by a single GNR and by a GNR dimer. As an example, we kept the diameters of all GNRs constant $40\ \mathrm{nm}$, and their plasmon resonances were tuned to the same wavelength of $765\ \mathrm{nm}$. In our study, three dyes with very different absorption and emission bands were examined. Under weak excitation, the fluorescence enhancement can be considered as the product of excitation enhancement and emission enhancement. Simulations showed that the GNR dimer exhibits better performance on enhancing both the excitation and radiative rates of an emitter, hence provides stronger fluorescence enhancement compared to the single GNR. Most interestingly, a GNR dimer offers much stronger enhancement for the nonlinear optical processes, e.g two-photon-excited fluorescence. As is shown in chapter 2, our simulations reveal that, for a GNR dimer with gap of $5\ \mathrm{nm}$, the enhancement factor for two-photon-excited fluorescence can be as high as $\sim 10^8$. The influence of plasmon resonances on the fluorescence lifetime and on the spectral shape is also investigated for all dyes. At last, we show that at

high excitation intensity, the enhancement factor for both one- or two-photon-excited fluorescence will be saturated to a limited value of the radiative enhancement by the plasmonic structures.

Quantum yield limits for the detection of single molecule enhanced by a single gold nanrod

Single-molecule techniques based on fluorescence depend strongly on the emission from the target molecules against the background noise, therefore suffer from the limitations imposed by weak emitting properties of most molecules. By enhancing the fluorescence with plasmonic nanostructures, such as GNRs, we can extend the application of these techniques to a wider range of species. Theoretical analysis indicates that emitter with lower quantum yield will experience stronger fluorescence enhancement because of larger emission enhancement, yet, the emitted photons will be less. In this work, we explore the lower limit of fluorescence quantum yield for single-molecule detection with the fluorescence enhanced by a single GNR. We specifically designed an infrared dye with the extremely low quantum yield of 10^{-4} and a comparatively large Stokes shift of $3,000\ \mathrm{cm}^{-1}$ to demonstrate single-molecule detection by fluorescence enhancement. For molecule with such large Stokes-shifts, both the excitation rate and the overall fluorescence enhancement need to be considered to get best single-to-noise ratio for single molecule detection. Based on the theoretical optimized conditions, we confirm experimentally the detection of single-molecule fluorescence with an enhancement factor of 3 orders of magnitude for the quantum yield 10^{-4}. Theoretical simulations indicate that single-molecule signals should be detectable for molecules with quantum yield as low as 10^{-6}, provided the dwell time of the molecules in the plasmonic hot spot is long enough.

Controlled synthesis of gold nanorod dimers with end-to-end configurations

Plasmonic coupling between metallic nanoparticles can strengthen the near-field enhancement inside the interparticle gaps, as well as the local density of photon states, compared to the individual nanoparticles. As a consequence, metal nanoparticle aggregates can be applied to enhance ultra-weak signals, such as two-photon-excited fluorescence, the signals of which are normally too weak to detect at the single-molecule level. Nanoparticle dimers provide single plasmonic hotspots without reducing the enhancement factors for both excitation and emission rates. Therefore nanoparticle dimer structures can be considered as the best plasmon-coupling system for single-molecule fluorescence enhancement in the sense that i) they provide single sites for fluorescence enhancement; ii) the photoluminescence backgrounds from the nanoparticles can be reduced compared to multimer aggregates.

Among all kinds of nanoparticles, the elongated GNRs may be among the best building blocks for the plasmonic dimer nanostructures, simply because of their narrow, intense, and tunable plasmon resonance with light. Here, we applied two strategies to synthesize the end-to-end GNR dimers with the aid of biotinylated streptavidin as the molecular linkers. Firstly, we illustrate the assembly in bulk of GNRs in the presence of the biotinylated streptavidin. The biotinylated streptavidin can bind specifically to the tips of the GNRs in the presence of

the surfactant cetyltrimethylammonium bromide (CTAB), hence can ensure the end-to-end assembly of the GNRs. The assembly was monitored by recording the extinction spectra of the assembly solution. The constructs were later deposited and keep to dry between glass slides. Secondly, we illustrate the GNR dimer assembly directly on glass sildes. We first immobilized the single nanorods on a clean glass slide, and functionalized them with the biotinylated streptavidin specifically on the tips of the each GNR. The molecular linkers functionalized on the immobilized gold nanrods have the chance of absorbing a second GNR in the solution, hence forming dimer structures. During the assembly, based on the bottom-up flipped strategy, we can separate the inevitable multimer aggregates. Therefore, we can get purified dimer structures on the glass. More details can be seen in chapter 4.

Two-photon-excited single-molecule fluorescence enhancement

Two-photon-excited fluorescence refers to the nonlinear optical process where the emission of a fluorophore is due to the absorption of two photons of identical frequency. Compared to one-photon excitation, two-photon-excited spectroscopy offers reduced scattering, deep sample penetration and intrinsic optical sectioning. Single-molecule detection of two-photon-excited fluorescence, however, is challenging because of the extremely low two-photon absorption cross section of most molecules. Here we applied the end-to-end GNR assemblies to enhance the single-molecule fluorescence under two-photon excitation. Simulations show that for an end-to-end GNR dimer with interparticle separation of $5\ \mathrm{nm}$, the overall fluorescence enhancement can reach 10^7 in the gap between the GNRs. With such high enhancement factors, we successfully detected enhanced two-photon-excited fluorescence from single ATTO 610 molecules.

Samenvatting

Dit proefschrift levert een algemene strategie voor de omgang met het voornaamste obstakel voor optische detectie van een enkel molecuul, namelijk dat het signaal van de meeste moleculen te zwak is in verhouding tot de achtergrond. Wanneer de detectiemethode is gebaseerd op fluorescentie kan de achtergrond efficiënt worden onderdrukt door spectrale filtering omdat de fotonen van de emissie een langere golflengte hebben dan die van de excitatie (ook wel "Stokes-shifted" emissie). Met detectie gebaseerd op plasmonische versterking zijn wij in staat om de helderheid van de fluorescente emissie te vergroten en daardoor de signaal tot ruis verhouding te verbeteren bij enkele molecuul detectie. Hiervoor maken wij gebruik van een enkel kristallijn goud nano staafje (GNS), omdat die een sterke nabij veld versterking heeft en een afstembare plasmonen resonantie. In deze studies onderzoeken wij theoretisch en experimenteel de detectie van fluorescentie versterkt door een enkel GNS of een GNS dimeer. Dit met als doel de detectie van moleculen met ultra zwakke emissie door lage kwantum opbrengst, tot zo laag als 10^{-4}, of van moleculen onder twee-foton excitatie.

Een- en twee-foton geëxciteerde fluorescentie versterking: individueel GNS versus GNS dimeren

Wij beginnen met een theoretische studie van de enkel-molecuul fluorescentie versterking door een individueel GNS en door een GNS-dimeer. Als voorbeeld gebruiken wij altijd staafjes met een diameter van 40 nm en een plasmonen resonantie van 765 nm. In deze studies onderzoeken wij drie verschillende kleurstof moleculen met heel verschillende absorptie en emissie banden. Onder zwakke excitatie kan de fluorescente versterking beschouwd worden als het product van de excitatie en emissie versterking. De simulaties laten zien dat de GNS-dimeer beter presteert, in verhouding tot een enkel GNS, voor zowel de mate van versterking van de excitatie als verkorting van de radiative levensduur. Het is interessant dat de GNS-dimeer ook een veel grotere versterking creëert in de niet-lineaire optische processen zoals bijvoorbeeld twee-foton geëxciteerde fluorescentie. Zoals gepresenteerd in hoofdstuk 2, laten onze simulaties zien dat voor een GNS-dimeer met een tussenruimte van 5 nm de versterkingsfactor voor twee-foton excitatie kan oplopen tot maar liefst 10^8. De invloed van de plasmonen resonantie op de fluorescentie levensduur en de spectrale vorm is vervolgens bestudeerd, voor elke van drie verschillende kleurstofmoleculen. Tot slot laten wij zien dat bij hoge excitatie intensiteit voor zowel een-foton als twee-foton geëxciteerde fluorescentie de versterkingsfactor een gelimiteerd saturatie niveau bereikt in verhouding tot de radiatie versterking die de plasmonische structuren anders kunnen leveren.

Kwantum opbrengst limieten voor de detectie van een enkel molecuul versterkt door een individueel GNS

Enkel-molecuul detectie technieken gebaseerd op fluorescentie zijn sterk afhankelijk van de emissie van het te onderscheiden molecuul ten opzichte van de achtergrond ruis. Dit werpt limitaties op voor de detectie van moleculen die zwakke emissie eigenschappen bezitten. Door versterking van de fluorescentie, gebruik makend van plamonische nano structuren, zoals een GNS, kan de enkel-molecuul techniek uitgebreid worden naar meer soorten moleculen. Theoretische analyse geeft de indicatie dat moleculen met een lagere kwantum opbrengst, relatief grotere fluorescentie versterking ondergaan door de grotere emissie versterking. Echter zal het aantal emissie fotonen minder zijn dan bij een molecuul met een hoge kwantum opbrengst. In dit werk onderzoeken wij wat de lagere limiet is van de fluorescentie kwantum opbrengst waarbij enkel-molecuul detectie nog mogelijk is met plasmonisch versterkte fluorescentie door een enkel GNS. Hiervoor hebben we een special kleurstof molecuul ontworpen met een extreem lage kwantum opbrengst van 10^{-4} en een vergelijkbaar grote Stokes-shift van $3000\ \mathrm{cm}^{-1}$. Dit is om enkel-molecuul detectie te demonstreren bij fluorescentie versterking. Voor een molecuul met zulke grote Stokes-shift moeten zowel de excitatie als de fluorescentie versterking in beschouwing genomen worden om de beste signaal tot ruis verhouding voor enkel-molecuul detectie te vinden. Gebaseerd op de theoretisch optimale condities wordt experimenteel bevestigd dat enkel-molecuul detectie, van een molecuul met een kwantum opbrengst van 10^{-4}, mogelijk is bij een versterkingsfactor van drie orde grotes. Theoretische voorspellingen geven aan dat het signaal van een enkel molecuul met een lage kwantum opbrengst tot wel 10^{-6} detecteerbaar zou kunnen zijn, mits het molecuul lang genoeg in het lokale plasmonische veld verblijft.

Gecontroleerde synthese van GNS dimeren met uiteinde-aan-uiteinde configuraties

In vergelijking met een enkel metalen nanodeeltje kan de plasmonische koppeling tussen metaal nanodeeltjes de nabij veld versterking in de tussenruimte tussen de deeltjes vergroten, evenals de lokale dichtheid van foton toestanden. Door deze eigenschappen kan een aggregatie van nano deeltjes toegepast worden voor de versterking van ultra zwakke signalen, zoals twee-foton geëxciteerde fluorescentie. Deze signalen zijn normaal te zwak om op enkel molecuul niveau te detecteren, zelfs bij versterking met een enkel GNS. GNS-dimeren genereren enkele geconcentreerde plasmonische gebiedjes zonder dat daar de fluorescencie versterkings factor wordt verkleind. Hierdoor kunnen GNS-dimeer structuren beschouwd worden als de beste plasmon gekoppelde systemen, voor enkel-molecuul fluorescentie versterking. Dit is omdat ze ten eerste voorzien in een enkele locatie voor de fluorescentie versterking, en ten tweede omdat de fotoluminescentie achtergrond bijdrage van een GNS-dimeer klein is in vergelijking met die van multimeer aggregaties van goud deeltjes.

Van alle soorten nanodeeltjes ziet het er naar uit dat het GNS als een van de beste bouwstenen gezien kan worden voor het maken van plasmonische dimeer structuren. Simpelweg vanwege de smalle, intense en afstelbare plasmonen resonantie met licht. Wij passen hier twee strategieën toe voor de synthese van uiteinde-aan-uiteinde GNS-dimeren, waarbij gebruik wordt gemaakt van biotinyleerd streptavidin, als moleculaire verbinder. Eerst wordt

een assemblage methode geïllustreerd waarbij goud nano-staafjes en gebiotinyleerde streptavidin in bulk vloeistof samen komen. De gebiotinyleerde streptavidin kan specifiek aan de uiteinden van een GNS binden in de aanwezigheid van de surfactant cetyltrimethylammonium bromide (CTAB) en daardoor er voor zorgen dat er een monster van uiteinde-aan-uiteinde geassembleerde goud nano-staafjes wordt gevormd. De assemblage wordt gemonitord door het extinctie spectrum te meten van de vloeistof waarin de assemblage plaatsvindt. Daarna worden de geassembleerde structuren gedeponeerd op een dekglas en droog bewaard tussen twee glaasjes. Als tweede strategie presenteren wij GNS-dimeer assemblage direct op een dekglas. Op een schoon dekglas werden eerst individuele goud nano-staafjes geïmmobiliseerd en vervolgens, specifiek aan het uiteinde, gefunctionaliseerd met gebiotinyleerde streptavidin. Daarna hebben de linkers aan de uiteinden van de geïmmobiliseerde goud nano-staafjes de kans om een tweede GNS uit de oplossing te binden, om een dimeer structuur te vormen. Door gedurende de assemblage de twee glaasjes, waartussen het proces plaats vindt, ondersteboven te draaien, kunnen de dimeren worden gescheiden van de onontkoombare multimeer assemblages in de oplossing. Zo verkrijgen wij gezuiverde dimeer structuren op het dekglas. Meer details zijn te vinden in hoofdstuk 4.

Twee-foton geëxciteerde enkele molecuul fluorescentie versterking

Twee-foton geëxciteerde fluorescentie verwijst naar het niet-lineaire optische proces waarbij de emissie van een fluorescent molecuul voort komt uit de absorptie van twee fotonen van identieke frequentie. In vergelijking met een-foton excitatie heeft twee-foton geëxciteerde spectroscopie de voordelen van gereduceerde licht verstrooiing, diepere monster penetratie en intrinsieke optische diepte scheiding. Enkele molecuul detectie van twee-foton geëxciteerde fluorescentie is echter uitdagend door de extreem kleine twee-foton absorptie cross sectie van de meeste moleculen. Hier hebben wij de uiteinde-aan-uiteinde geassembleerde GNS structuren toegepast voor het versterken van enkele molecuul fluorescentie bij twee-foton excitatie. Simulaties laten zien dat voor uiteinde-aan-uiteinde GNS-dimeren met een tussenruimte van 5 nm een totale fluorescentie versterking van 10^7 bereikt kan worden in de kleine ruimte tussen de twee goud nano-staafjes. Met behulp van deze versterkingsfactor hebben we succesvol twee-foton geëxciteerde fluorescentie gemeten van een enkel ATTO 610 molecuul.

Curriculum Vitae

I was born on 3st March 1983 in Fujian Province, China. I got my BSc degree in Theoretical Physics at Lanzhou University (Lanzhou, China) in 2006. I started my master project at Peking University (Beijing, China) under the supervision of Prof. Dr. Ruopeng Wang. I obtained the Master degree of Science with the title of 'Study of a Dielectric-Loaded Plasmonic Lens' in 2011. I then joined the research group of Prof. Dr. Weihai Ni as a research assistant at Suzhou Institute of Nano-Tech and Nano-Bionics (SINANO). In September 2017, I started my PhD in the group of Prof. Dr. Michel Orrit at Leiden University. During my PhD, I worked on plasmon-mediated single-molecule fluorescence enhancement under one- and two-photon excitation.

List of Publications

21. **X. Lu**, D. Punj, M. Orrit, *Two-photon excited single-molecule fluorescence enhanced by gold nanorod dimers*, *In preparation*.

20. **X. Lu**, D. Punj, M. Orrit, *Controlled synthesis of gold nanorod dimers with end-to-end configurations*, *In preparation*.

19. **X. Lu**, G. Ye, D. Punj, R. C. Chiechi, M. Orrit, *Quantum yield limits for the detection of single-molecule fluorescence enhancement by a gold nanorod*, ACS Photonics **7**, 2498 (2020).

18. **X. Lu**, W. Ye, W. You, H. Xie, Z. Hang, Y. Lai, W. Ni, *Collective resonance in helical superstructures of gold nanorods*, Physical Review B **101**, 045431,(2020).

17. F. Zhao, X. Wang, Y. Zhang, **X. Lu**, H. Xie, B. Xu, W. Ye, W. Ni, *In situ monitoring of silver adsorption on assembled gold nanorods by surface-enhanced Raman scattering*, Nanotechnology **31**, 295601 (2020)

16. W. Zhang, M. Caldarola, **X. Lu**, M. Orrit, *Plasmonic Enhancement of Two-Photon-Excited Luminescence of Single Quantum Dots by Individual Gold Nanorod*, ACS Photonics **5**, 2960 (2018).

15. W. Zhang, M. Caldarola, **X. Lu**, B. Pradhan, M. Orrit, *Plasmonic enhancement of a near-infrared fluorophore using DNA transient binding*, Physical Chemistry Chemical Physics **20**, 20468 (2017).

14. Z. Yang, Z. Li, **X. Lu**, F. He, X. Zhu, Y. Ma, R. He, F. Gao, W. Ni, Y. Yi, *Controllable biosynthesis and properties of gold nanoplates using yeast extract*, Nano-micro letters **9**, 1 (2017).

13. P. Xu, **X. Lu**, J. Zhao, Y. Li, S. Chen, J. Xue, W. Ou, S. Han, Y. Ding, W. Ni, *Metal Adsorbate-Induced Plasmon Damping in Gold Nanorods: The Difference Between Metals*, Nano **11**, 1650099 (2016).

12. P. Xu, **X. Lu**, S. Han, W. Ou, Y. Li, S. Chen, J. Xue, Y. Ding, W. Ni, *Dispersive Plasmon Damping in Single Gold Nanorods by Platinum Adsorbates*, Small **12**, 5081 (2016).

11. C. Shen, X. Lan, **X. Lu**, T. A. Meyer, W. Ni, Y. Ke, Q. Wang, *Site-specific surface functionalization of gold nanorods using DNA origami clamps*, Journal of the American Chemical Society **138**, 1764 (2016).

10. J. Zhao, P. Xu, Y. Li, J. Wu, J. Xue, Q. Zhu, **X. Lu**, W. Ni, *Direct coating of mesoporous titania on CTAB-capped gold nanorods*, Nanoscale **8**, 5417(2016).

9. Z. Chen, X. Lan, Y. C. Chiu, **X. Lu**, W. Ni, H. Gao, Q. Wang, *Strong chiroptical activities in gold nanorod dimers assembled using DNA origami templates*, ACS Photonics **2**, 392 (2015).

8. X. Lan, **X. Lu**, C. Shen, Y. Ke, W. Ni, Q. Wang, *Au nanorod helical superstructures with designed chirality*, Journal of the American Chemical Society **137**, 457 (2015).

7. C. Shen, X. Lan, **X. Lu**, W. Ni, Q. Wang, *Tuning the structural asymmetries of three-dimensional gold nanorod assemblies*, Chemical Communications **51**, 13627 (2015).

6. J. Wu, **X. Lu**, Q. Zhu, J. Zhao, Q. Shen, L. Zhan, W. Ni, *Angle-resolved plasmonic properties of single gold nanorod dimers*, Nano-micro letters **6**, 372 (2014).

5. G. Dai, **X. Lu**, Z. Chen, C. Meng, W. Ni, Q. Wang, *DNA origami-directed, discrete three-dimensional plasmonic tetrahedron nanoarchitectures with tailored optical chirality*, ACS applied materials & interfaces **6**, 5388 (2014).

4. J. Niu, D. Wang, H. Qin, X. Xiong, P. Tan, Y. g Li, R. Liu, **X. Lu**, J. Wu, T. Zhang, W. Ni, J. Jin, *Novel polymer-free iridescent lamellar hydrogel for two-dimensional confined growth of ultrathin gold membranes*, Nature communications **5**, 1 (2014).

3. **X. Lu**, J. Wu, Q. Zhu, J. Zhao, Q. Wang, L. Zhan, W. Ni, *Circular dichroism from single plasmonic nanostructures with extrinsic chirality*, Nanoscale **6**, 14244 (2014).

2. X. Lan, Z. Chen, **X. Lu**, G. Dai, W. Ni, Q. Wang, *DNA-directed gold nanodimers with tailored ensemble surface-enhanced Raman scattering properties*, ACS applied materials & interfaces **5**, 10423 (2013).

1. X. Lan, Z. Chen, G. Dai, **X. Lu**, W. Ni, Q. Wang, *Bifacial DNA origami-directed discrete, three-dimensional, anisotropic plasmonic nanoarchitectures with tailored optical chirality*, Journal of the American Chemical Society **135**, 11441 (2013).

Acknowledgements

At the end of this thesis, I would like to acknowledge many people without whom the this work would have been impossible.

First and foremost, I would like to express my sincere gratitude to my supervisor Prof. Michel Orrit for his dedicated support and guidance through out the project. His expertise and deep insights in science has made the PhD period an inspiring experience for me. I really appreciate his encouragement and patience in the early stage of my PhD.

I am thankful to Dr. Deep Punj for his contributions in the thesis. I would like to thank him for working together with me in the lab and having day-to-day discussions, and for his contributions in the SEM images, which constitute a considerable part in chapter 4 and 5 of this thesis. I would like to thank Dr. Gang Ye and Dr. Ryan C. Chiechi for providing the low quantum yield dye NDI-2TEG-3T, which contributes to chapter 3 of this thesis.

I owe a big thank to Dr. Weichun Zhang who helped me a lot with the optical setup and equipment in the lab. I thank Dr. Xueyan Miao for guiding me in the chemical lab and for teaching me a lot with sample preparation. I would like to thank Dr. Siddharth Ghosh and Dr. Sergii Pud for working together on the high magnet experiment in Nijmegen. Special thank goes to Dr. Siddharth Ghosh for his kindly encouragement, which helped me overcome the difficulty in oral communication. I also thank Dr. Sergii Pud for providing the glass slides with markers. I thank Dr. Martín Caldarola and Dr. Tomas Jollans for the help in maintaining of the fs laser. I thank Zohre Eskandari for the suggestions on molecular linkers for the assembly experiments.

I greatfully acknowledge Henriette van Leenuwen for careful handling lots of paperwork, Harmen van der Meer for making mechanical components and reaction chambers, Lionel Ndamba for the help in chemical lab. I thank Jacco Ton for Dutch translation of the summary. I would also like to thank many colleagues in MoNOS group including Enrico, Pravin, Patrick, Zoran, Amin, Martin, Subhasis, Biswajit, Wiebke, Christopher, Robert, Nasrin, Eduardo, Rene, Alvaro, Leonardo, Martina, and all the friends in my life.

I wish to express my sincere appreciation to my family for their boundless love and support, especially my father who would be happy if he could witness the moment I become a doctor. Finally, I would like to thank Xiaojing Yan and my little son Yining for their unconditonal love.